FACHBEREICH NATURWISSENSCHAFTEN
BERGISCHE UNIVERSITÄT
WUPPERTAL

Geometry Reconstruction of Fluorescence Detectors Revisited

Daniel Kümpel

Diplomarbeit

August 2007
WU D 07-13

Abstract

Since the 60's, when the use of extensive air shower (EAS) fluorescence light yield was first proposed for the detection of ultra high energy cosmic rays (UHECR's), many past, current and future experiments utilize the effect to get a clue about the origin of cosmic rays. In the fluorescence technique, the geometry of the shower is reconstructed based on the correlation between viewing angle and arrival time of the signals detected by the telescope. The signals are compared to those expected for different shower geometries and the best-fit geometry is determined. The calculation of the expected signals is usually based on a relatively simple function which is motivated by basic geometrical considerations. This function is based on certain assumptions on the processes of light emission and propagation through the atmosphere. The present work investigates the validity of these assumptions and provides corrections that can be used in the geometry reconstruction. The impact on reconstruction parameters is studied. The results are also relevant for hybrid observations where the shower is registered simultaneously by fluorescence and surface detectors.

Contents

List of Figures

List of Tables

Chapter 1

Introduction

Even though you neither feel them nor see them, every second we are bombarded by thousands of ionized cosmic ray particles. Most of them are protons, but also α-particles and heavier nuclei are among them. Fundamental questions arise:

- "Where do they come from?" and in particular
- "What is the acceleration mechanism to such high energies which have already been observed?"

Even today the answers to these questions are not fully understood. The measurement of the particle flux, elemental composition, arrival direction distribution and temporal variations are of central importance to get a clue of an answer. More insight to these questions would make a major break-trough in understanding the high energy Universe and would open an entirely new field of research on its own.
The story of "astroparticle physics" started almost a century ago, when the Austrian physicist Victor Franz Hess discovered cosmic rays, charged particles that hit our atmosphere like a steady rain from space. Astrophysics together with particle physics has fundamentally changed our view of the Universe. Although the term "astroparticle physics" has been widely accepted since only 10-15 years, the first triumph of the relatively new scientific field dates back to the seventies: the detection of solar neutrinos. Together with the detection of neutrinos from a supernovae in 1987, it marks the birth of neutrino astrophysics, acknowledged with the Nobel prize of physics in 2002. The enormous discovery potential of the field stems from the fact that attainable sensitivities are strongly improving in the previous two decades. But not this alone is arguably enough to raise expectations. We are entering territories with a high discovery potential, as predicted by theoretical models. For the first time we are able to tackle the aforementioned questions with the necessary sensitivity. One backbone of astroparticle physics are particle detectors, telescopes and antennas. The size of these instruments are generally large due to the scarcity of the signals that are to be detected and are instrumented in "open" media like water, ocean, ice or rarely populated area. They are operating e.g. at high altitudes and locations with small background from artificial light sources.

The present flagship in the search for ultra-high energy cosmic rays is the Southern Pierre Auger Observatory located in the Argentinean pampa. For the first time it combines two independent detection techniques. Surface detectors on the ground cover a huge area in order to detect and study secondary particles of extensive air showers. Another complementary technique utilizes the fact that shower particles excite nitrogen molecules on their passage through the atmosphere. The de-excitation proceeds partially through the emission of fluorescence light, which can be detected by telescopes at the ground. The synergy of these techniques is able to reduce systematic uncertainties, improves the event reconstruction and provides important cross-check information. Since the celestial distributions of possible sources, background radiation and magnetic fields require full-sky coverage, the Northern Pierre Auger Observatory is planned to be built in Colorado, United States.
The use of fluorescence light was first successfully demonstrated by the Utah group, which was the starting point for founding the Fly's Eye detector and successive air shower fluorescence experiments. All experiments have in common the way of reconstructing the geometry of the air shower. This work revisits the reconstruction procedure under special attention of fluorescence light emission and propagation through the atmosphere. It it shown, that the standard fitting formula has to be adjusted in order to account for a realistic light propagation and emission.

The second Chapter gives an introduction to some important aspects of cosmic ray physics. Chapter 3 focusses on extensive air showers and explains the development and main components. Additionally, the most common detection techniques for air showers are discussed. Chapter 4 gives a brief introduction of the Pierre Auger Observatory, its detection technique and main framework. The standard fluorescence reconstruction procedure is discussed and an insight into the OFFLINE software is given. Chapter 5 summarizes the standard reconstruction of fluorescence signals and discusses investigations for a new parametrization of the pulse centroid uncertainty. In Chapter 6 several aspects of fluorescence light reconstruction are revisited. The propagation speed of extensive air showers are examined as well as the speed of fluorescence light and low energy particles. Delays caused by excitation and de-excitation processes are discussed and their implication on reconstruction parameters are presented. The impact of bended fluorescence light on hybrid reconstruction is shown and the consequences to the synchronization between surface detector and fluorescence telescope are highlighted. Finally, the most important results are summarized in Chapter 7 followed by some concluding remarks for future analyses. An OFFLINE example for hybrid simulation and reconstruction as well as some explanations concerning used parameters and cuts are given in the Appendix.

Chapter 2

Cosmic Rays

At the end of the 19^{th} century some scientists had come to the conclusion that there was little more to do in physics than fill in a few more figures after the decimal point of various fundamental constants. They could not have been more wrong. Small variations in the expectation turned out to be crucial enough to roll up fundamental physics.
At this time it was already known that even perfectly insulated electrostatic devices would discharge themselves. Is was realized that the gradual discharging of bodies could be explained if the air contained ionized particles. But where do those ions come from? The british physicist Charles Wilson carried out an, at this time, baffling experiment. He measured how quickly charge leaked away from a gold leaf electroscope and tried to find out the reasons for the discharge, but neither day/night variations nor different sources of air could cause any differences. He was forced to conclude that, in some way or another, ions were actually formed within the air in a sealed container at a rate that he could measure with equal amounts of positive and negative charge. It became known as "spontaneous" ionization.
This spontaneous ionization had properties very similar to radiation from radioactive substances. In 1901, Wilson wondered whether the cause of the ionization might be radioactive rays from outside the Earth's atmosphere, so he went into a Scottish railway tunnel to see if the ionization attenuates. Unfortunately, he did not realize that the discharge effect is affected not only by rays of particles penetrating the atmosphere but also by radioactivity in the Earth. His apparatus was not sufficient enough to separate these effects. He concluded that the source of ionization must be something in the air itself.

The crucial experiment started 10 years later at six o'clock in the morning of August 7, 1912, when the Austrian physicist Victor Franz Hess started a remarkable balloon ascent. In order to measure the ionization as a function of height he made his last trip of a series of seven balloon ascents. At that time, still, most of the ionization had been traced to radioactive impurities and deposits. Hess wanted to demonstrate with an improved electroscope, that the ionization in a hermetically sealed vessel reduces with increasing height due to the reduction of radioactive substances of the Earth [1], but he discovered a baffling result. Up to a height of about 1000 m the ionization decreased almost as

expected, but then it increased and in roughly 3000 m height the ionization is as strong as it is on the Earth surface. He concluded, that the cause of that boost in ionization might be attributed to the penetration of the Earth's atmosphere from outer space by hitherto unknown radiation of high penetrating capacity [2]. He discovered the *Cosmic Radiation*. 24 years later Hess shared the nobel price in physics "for his discovery of cosmic radiation".

2.1 Energy spectrum

The flux of cosmic ray particles extends from a few hundreds MeV to beyond 10^{20} eV. The spectrum can be approximated by an inverse power law in energy with an differential flux given by

$$\frac{dN}{dE} \propto E^{-\alpha} \ , \tag{2.1}$$

with $\alpha \approx 2.7$ up to $E \sim 3 \times 10^{15}$ eV and above this energy it steepen to $\alpha \approx 3.0$ as can be seen in Fig. 2.1. This region is called the "knee" and was first deduced from observations made by Kulikov and Khristianson *et al.* in 1956 [3]. The position of the knee is dependent of the particle type and is caused mainly by changes in the flux of light cosmic rays (see also Section 2.4). The all-particle spectrum reveals also additional structures at about 10^{17} eV and $\sim 3 \times 10^{18}$ eV known as the "second knee" and the "ankle". Today there is still no consensus about the existence of the second knee, whereas the ankle is reported evidentiary by several experiments (e.g. [4, 5, 6, 7]) and traditionally explained in terms of transition from galactic to extra galactic cosmic rays. A model for that is proposed e.g. in [8] by Hillas.

At the highest energies the cosmic ray flux decreases from originally $\sim 10^3$ $\mathrm{m^{-2}s^{-1}}$ at few GeV to ~ 1 $\mathrm{km^{-2}}$ per century at 100 EeV. This implies large detector arrays to obtain reasonable statistics. So far only three experiments (HiRes [11], AGASA [12] and Auger [13]) were able to receive enough statistical data to derive information about the spectra at highest energies. Recent results from the Pierre Auger Observatory reject the hypothesis that the cosmic ray spectrum continues in the form of a power-law above an energy of $10^{19.6}$ eV with 6σ significance [14] (cf. Sec. 2.6).

2.2 Chemical composition

Certainly, one scientifically most relevant piece of information are precise data on the chemical composition of the primary cosmic ray flux as a function of energy. In comparison to the composition of stellar material in our solar system the differences are quite small as shown in Fig. 2.2. However, there are still some differences in detail, which are very important. For light elements there is an overabundance of Hydrogen and Helium for solar system abundances. Lithium, Beryllium and Boron are overabundant in cosmic rays. Iron agrees quite well with solar system composition, but there is an excess of elements slightly lighter than Iron. One way to understand the overabundances of cosmic rays is to assume

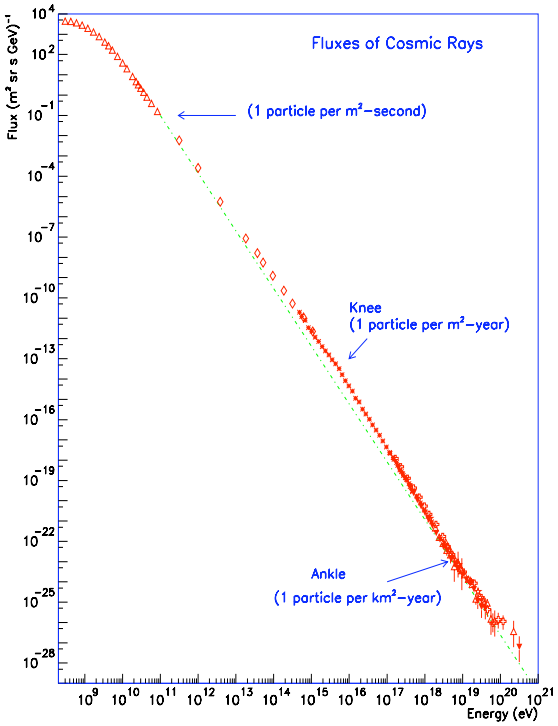

(a) Primary cosmic ray flux (from [9]).

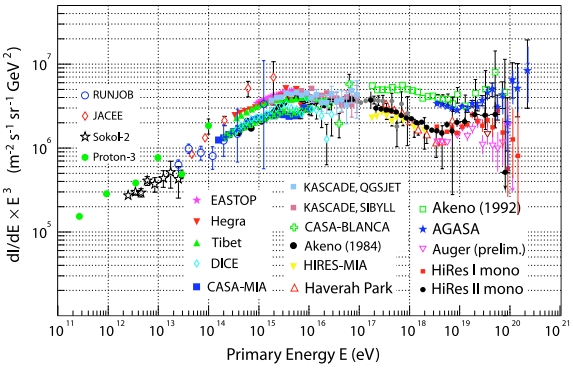

(b) Primary cosmic ray flux scaled with E^3 (from [10]).

Figure 2.1: All-particle energy spectrum.

that cosmic rays have the same composition as solar matter at their origin. Propagating through the interstellar space they can interact with gas and dust particles, which results in heavier nuclei spallating into lighter nuclei.

From the knowledge of the spallation cross sections obtained in accelerator experiments one can learn something about the amount of matter traversed by cosmic rays between production and observation. For the bulk of cosmic rays the average amount[1] of matter traversed is of the order $X = 5$ g/cm^2 to $X = 10$ g/cm^2 (cf. [16]). Furthermore, the density ρ_N of the galactic disc can be approximated to one proton per cm^3. With the proton mass $m_p = 1.67 \cdot 10^{-24}$ g one can calculate the corresponding thickness L of the material to

$$L = \frac{X}{m_p \rho_N} = 3 \times 10^{24} \text{ cm} = 1 \text{ Mpc}.$$

The diameter of the galactic plane is ≈ 30 kpc so one could conclude, that low energy cosmic rays propagate on a very winding way through our galaxy. The resulting lifetime τ is

[1] Note that the amount is energy dependent

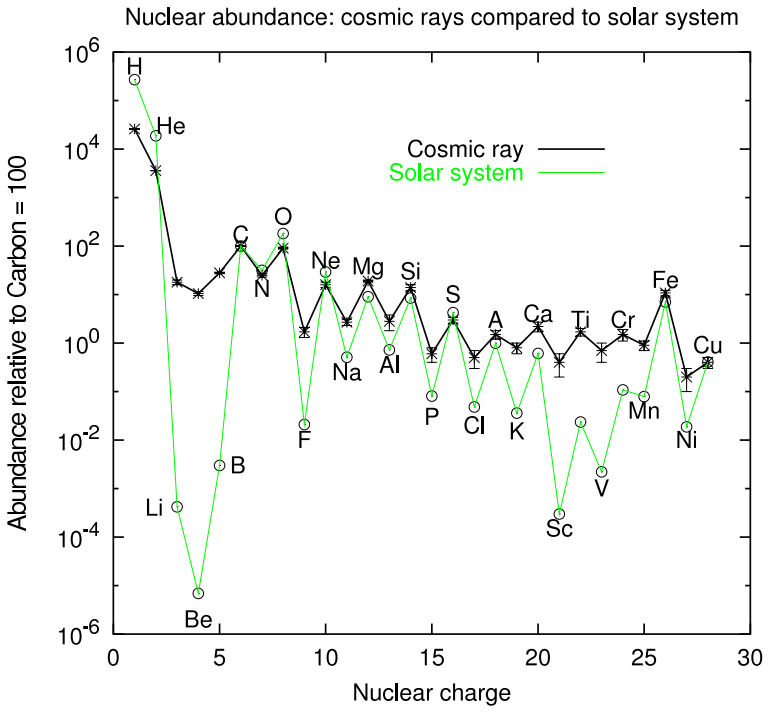

Figure 2.2: Relative abundances of solar and cosmic ray material for low energy cosmic rays (from [15]).

$$\tau = \frac{L}{v} \approx 3 \times 10^6 \text{ years.}$$

Methods of radioactive dating [15] indicate $\tau \approx 2 \times 10^7$ years. This relative large value implies that cosmic ray nuclei spend also significant time diffusing in low density galactic halo regions before escaping into intergalactic space.

Up to energies of about 10^{15} eV measurements on balloons and spacecraft have an important advantage over ground based air shower experiments, because they can detect the primary cosmic particles directly and measure its charge above the atmosphere. A significant point is the first knee. In KASCADE [17] a gradual change in composition is observed through the knee from a lighter to a heavier composition as can be seen in Fig. 2.3. To characterize the cosmic ray mass composition one often uses the mean logarithmic mass $\langle \ln A \rangle$, defined as

$$\langle \ln A \rangle = \sum r_i \ln A_i \ ,$$

where r_i is the relative fraction of nuclei with atomic mass number A_i.

The mass composition of cosmic rays at highest energies is very important to understand the origin of the ankle in the energy spectrum. An almost pure proton composition in this energy range would support the model proposed by Berezinsky [19], where the "dip" is due to an energy loss of extragalactic protons by e^+e^--pair production on the

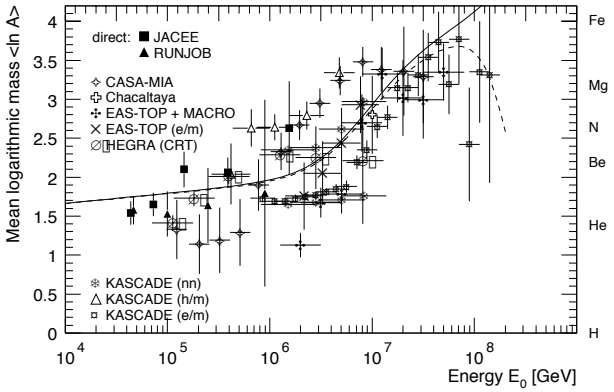

Figure 2.3: Mean logarithmic mass as a function of Energy. Experiments measuring electron, muons and hadrons at ground level. A change in the composition from light to heavy elements can be seen (modified from [18]).

microwave background during propagation. A change of composition from heavy to light nuclei in this energy range could be explained by a transition from galactic to extragalactic cosmic rays.

2.3 Anisotropies

Anisotropies in the arrival direction of cosmic rays are clearly of great interest to locate possible sources. Since we are living inside a galaxy one would expect an anisotropy towards the center if the cosmic ray sources are galactic objects, but there are a number of problems in interpreting the data of anisotropy mainly due to low statistics. The highest statistics so far comes from the Auger experiment. The collaboration searched for point like sources in the direction of Sagittarius A without finding significant excess [20]. Fig. 2.4 (*left*) shows a map of over-densities in circular windows of 5° degree radius with energies in the range of $10^{17.9}$ - $10^{18.5}$ eV. The galactic plane is indicated by a solid line and the galactic center is indicated by a cross. The big circle is the region where AGASA [21] reported an excess and the small circle is the reported excess from SUGAR [22]. The size of the over-densities are consistent with the expected statistical fluctuations (*right*) of an isotropic sky and hence no significant departure from isotropy is observed.

2.4 Cosmic ray acceleration models

A major puzzle ever since the discovery of cosmic rays almost 100 years ago has been their exact origin. Particles with energies exceeding 10^{20} eV have already been observed, which shows that there have to exist very powerful sites of acceleration in the Universe. Since the magnetic fields of the Milky Way are not strong enough to confine particles above the knee ($\sim 10^{16}$ eV) it is plausible that their origin is outside the galaxy, whereas

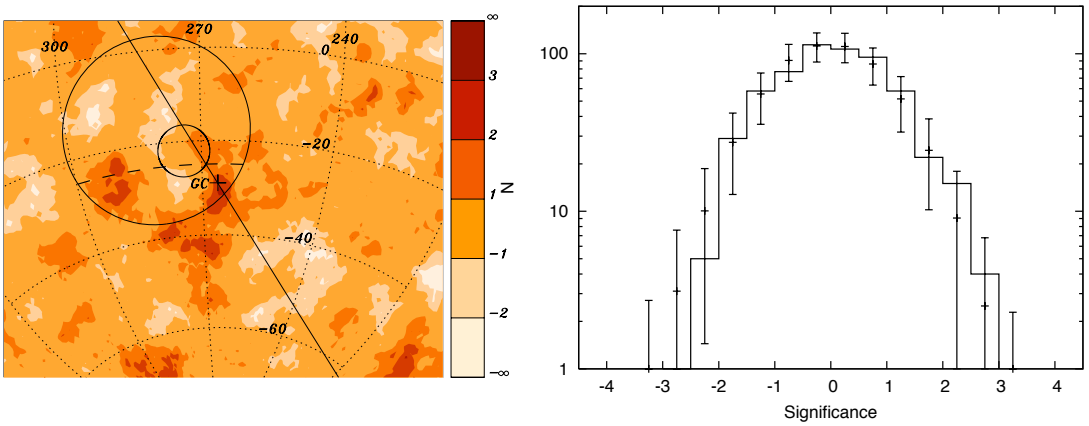

Figure 2.4: *Left:* Significance map of cosmic ray over-densities in the region of the galactic center in the energy range $10^{17.9} - 10^{18.5}$ eV, showing the galactic center (cross), the galactic plane (solid line), the regions of large excess from SUGAR (small circle) and AGASA (big circle), and the field of view limit (dashed line). *Right:* Corresponding histogram of over-densities computed on a grid of 3° spacing, compared to the average isotropic expectation points (with 2σ bounds) [20].

galactic sources are responsible for the lower-energy part.
There are basically two types of mechanisms for *bottom-up*[2] cosmic ray production:

1. The particles are directly accelerated to high energy by an extended **electric field**. This theory goes back to 1933 when Swann made the first plausible suggestion of how cosmic ray energies might be attained [23]. The acceleration is induced by changing magnetic fields near the surface of the sun and stars. It has been known that magnetic fields of up to several kilo-gauss are associated with sunspots, which may appear and disperse over a period of days or weeks on the sun's surface. So so called "one-shot" mechanisms have been worked out in great detail and the electric field is now generally associated with the rapid rotation of small, highly magnetized objects such as pulsars or active galactic nuclei (AGN). Although it is quite fast, this mechanism is not widely favored these days, because it suffers from the circumstances, that the acceleration occurs in astrophysical sites of very high energy density, where the cross section for energy loss processes are high. Another reason is, that the theory can not explain the observed power law spectrum.

2. The particles are accelerated in a **stochastic** way. These models go back to Fermi in 1949 when he proposed an acceleration mechanism, in which particles gain energy gradually by numerous encounters with moving magnetized plasma [24]. However,

[2]In *bottom-up* models the cosmic ray starts with low energy and is accelerated. Usually exotic particles are used in *top-down* models where particles start initially with very high energy and decay to the observed cosmic ray particles.

this mechanism is slow compared to the electric field acceleration, and it is hard to keep the particles confined within the Fermi engine (for more details see Sec. 2.5).

2.5 Fermi mechanism

The basic idea is that cosmic ray particles traverse interstellar space and collide with large objects (like magnetized clouds), which move with random velocity and direction. Depending on the exact relative motion between particle and cloud, the cosmic ray can either lose or gain energy.
Consider a test particle which increases its energy E by an amount $\Delta E = \xi E$ proportional to its energy per "encounter" with an magnetic cloud. Let E_0 be the energy of injection. After n encounters the energy E_n is

$$\begin{aligned} E_n &= E_0(1+\xi)^n \\ n &= \frac{\ln(E_n/E_0)}{\ln(1+\xi)} \; . \end{aligned}$$

Let $P_{\rm esc}$ be the probability for a particle to escape from the region, that is occupied by magnetic clouds, after one encounter. The probability for a particle to reach energy E_n inside the cloud is $(1-P_{\rm esc})^n$. Clearly, the number of particles that are distinguished to remain longer in the cloud (and gain more energy) is proportional to the number of particles that remain in the acceleration region for more than n encounters

$$N(>E_n) = N_0 \sum_{m=n}^{\infty} (1-P_{\rm esc})^m \propto \frac{1}{P_{\rm esc}} \left(\frac{E_n}{E_0}\right)^{-\gamma}$$

with

$$\gamma = \frac{\ln\left(1/(1-P_{\rm esc})\right)}{\ln(1+\xi)} \approx \frac{P_{\rm esc}}{\xi} \; .$$

The result is that stochastic acceleration leads to power law energy spectra.

Second order Fermi acceleration

The basic idea dates back to 1949, when Enrico Fermi proposed an acceleration mechanism for cosmic rays [24]. The acceleration relates to the amount of energy gained during the motion of a charged particle in the presence of randomly moving magnetized clouds ("magnetic mirrors"). Fermi argued, that the probability for a head-on collision is greater than a head-tail collision, so particles would, on average, be accelerated. Assuming a cosmic ray particle entering into a single cloud with energy E_i and incident angle θ_i with the cloud's direction, it undergoes diffuse scattering on the irregularities in the magnetic field. The energy gain of the particle, which emerges at an angle θ_f with energy E_f, can be obtained by applying Lorentz transformations between laboratory frame (unprimed)

and cloud frame (primed):

$$E_i' = \Gamma E_i(1 - \beta \cos\theta_i) \quad (2.2)$$
$$E_f = \Gamma E_f'(1 - \beta \cos\theta_f) \ , \quad (2.3)$$

where Γ and $\beta = V/c$ are the Lorentz factor and the velocity of the magnetic cloud in units of the speed of light, respectively. The fractional energy change is then

$$\xi = \frac{\Delta E}{E} = \frac{E_f - E_i}{E_i} \ . \quad (2.4)$$

By averaging over $\cos\theta_i$ (depending on the relative velocity between the cloud and the particle) it can be shown (e.g. in [16]) that the fractional energy change is proportional[3] to $\frac{4}{3}\beta^2$:

$$\xi \propto \frac{4}{3}\beta^2 \ . \quad (2.5)$$

First order Fermi acceleration

The big disadvantage of the second order Fermi acceleration is the very slow acceleration process. During the late 70's a more efficient acceleration mechanism was proposed, realized for cosmic ray encounters with plane shock fronts [25]. Assume a large shock wave propagating with velocity $-\vec{u}_1$. Relative to the shock front, the downstream shocked gas is receding with velocity $\vec{u}_2$, where $|u_2| < |u_1|$, and thus in the laboratory frame it is moving in the direction of the front with velocity $\vec{V} = \vec{u}_2 - \vec{u}_1$. To find the energy gain per crossing, one can identify the magnetic irregularities on either side of the shock as the clouds of magnetized plasma and proceed similar to Fermi's original idea. For the rate at which cosmic rays cross the shock from downstream to upstream, and upstream to downstream, one finds $\langle \cos\theta_i \rangle = -2/3$ and $\langle \cos\theta_f' \rangle = 2/3$ [16]. The fractional energy change ξ (cf. Eqn. 2.5) can be written as [16]

$$\xi \propto \frac{4}{3}\beta \ . \quad (2.6)$$

The term "first order" stems from the fact that the energy gain per shock crossing is proportional to β, the velocity of the shock divided by the speed of light, and therefore more efficient than Fermi's original mechanism. This is because of the converging flow - it does not matter on which side of the plasma you are, if you are moving with the plasma, the plasma on the other side is approaching you.
Note that in the first order mechanism the spectral index, γ, is independent of the absolute magnitude of the velocity of the plasma. It depends only on the ratio of the upstream and downstream velocities. For strong shocks the acceleration mechanism leads in a natural way to an E^{-2} spectrum [26].

[3] assuming a non-relativistic speed of the magnetic cloud

2.6 GZK-suppression

The discovery of the microwave background radiation by Penzias and Wilson [27] 1965 lead Greisen [28] and independently Zatsepin and Kuzmin [29] 1966 to the point, that this radiation would make the Universe opaque to high energy protons, today known as the *GZK-suppression*[4]. They found that, above a few 10^{19} eV, thermal photons are seen highly blue-shifted by the protons in their rest frames. Here the energy of the microwave background photons γ_{CMB} is sufficient to excite baryon resonances and thus draining the high energy of the proton via pion production as shown in Fig. 2.5 and Fig. 2.6.

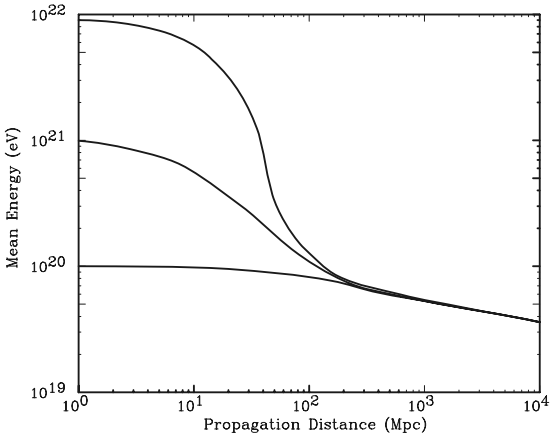

Figure 2.5: Mean energy of protons as a function of propagation distance through the CMB for different source energies of 10^{22} eV, 10^{21} eV, and 10^{20} eV [30].

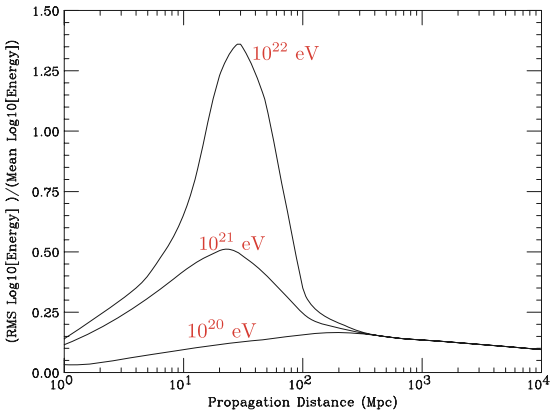

Figure 2.6: Fluctuation of the energy of a proton propagating through the CMB. Different energies are indicated [30].

A secondary effect is the production of ultra high energy gamma rays and neutrinos. Three sources of energy loss for ultra high energy protons are known:

1. **Adiabatic fractional energy loss**
   This is a result of the expansion of the Universe.

2. **Photo-Pion production**
   The cutoff energy is a result of the threshold of pion production in the interaction of cosmic ray protons with cosmic background photons. The cross section is strongly increasing at the $\Delta^+(1232)$ resonance. The GZK-effect can be described as

$$\begin{aligned} p + \gamma_{\mathrm{CMB}} \rightarrow \Delta^+(1232) &\rightarrow n + \pi^+ \\ &\rightarrow p + \pi^0 \ . \end{aligned}$$

In addition also other baryon resonances can occur with increasing energy:

[4] In literature this effect is also known as the GZK-Cutoff, although it is not a real cutoff.

$$p + \gamma_{\mathrm{CMB}} \rightarrow \Delta^{++} + \pi^- \rightarrow p + \pi^+ + \pi^- \ ,$$

where Δ^{++} indicates e.g. $\Delta(1620)$ or $\Delta(1700)$ resonances.

3. **Pair production**
   Another important energy loss is the e^+e^- pair production:

$$p + \gamma_{\mathrm{CMB}} \rightarrow p + e^+ + e^- \ .$$

At energies around and above the GZK-suppression ($E > 10^{19}$ eV) the characteristic time for e^+e^- production is $t \approx 5 \times 10^9$ yr [31]. At this energy photo-pion production is the main contribution to the proton energy loss.

However, in spite of the prediction of the GZK-suppression, a number of experiments claimed to have observed events with $E > 10^{20}$ eV. Even before the cutoff was proposed in 1966, Volcano Ranch [32] observed one event. Later on, SUGAR [33] and Haverah Park [34] observed high energy events as well, but the interpretation is still disputed. Recently, both, the Yakutsk Array [35] and AGASA [36] have claimed to measure events above 10^{20} eV. The Yakutsk Array result seems to be in accordance with the GZK-suppression, but AGASA has claimed the opposite. In 2006 the High Resolution Fly's Eye (HiRes) experiment claimed to observe the GZK-suppression [37]. HiRes observed two features in the ultra-high energy cosmic ray flux spectrum: The ankle at $4 \cdot 10^{18}$ eV and a high energy break in the spectrum at the energy of the GZK-suppression around $6 \cdot 10^{19}$ eV with a significance of about 4σ (cf. Fig. 2.7).
Recent results from the Pierre Auger Observatory reject the hypothesis that the cosmic ray spectrum continues in the form of a power-law above an energy of $10^{19.6}$ eV with 6σ significance [14]. Fig. 2.8 shows the combined energy spectrum in comparison to some astrophysical models both multiplied by E^3. The blue lines assume a mixed composition at the sources, i.e. with nuclear abundances similar to those of low-energy cosmic rays.
However, due to big systematic and statistical uncertainties there is still no definite conclusion about the existence of the GZK-suppression although it tends to the existence of a suppression.

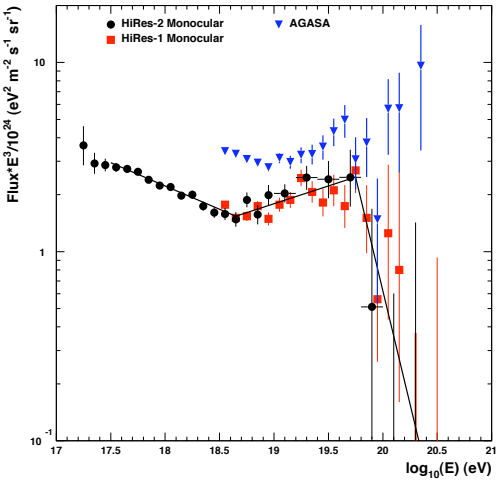

Figure 2.7: The measured spectra from HiRes-I and HiRes-II in monocular mode compared with AGASA data. The solid line is a broken power law spectrum with two break points (from [37]).

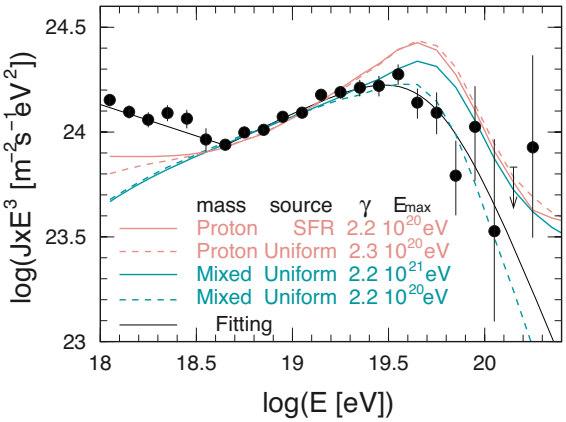

Figure 2.8: The combined energy spectrum measured with Auger multiplied by E^3. The predictions of two astrophysical models (blue and red lines) are indicated together with some input assumptions (from [14]).

Chapter 3

Extensive Air Showers

An Extensive Air Shower (EAS) is a cascade of particles generated by the interaction of an initial high energy primary particle near the top of the atmosphere. The number of generated particles at first multiplies, then reaches a maximum before it attenuates more and more as particles fall below the threshold for further particle production. The measurement of EAS provides the only basis of cosmic ray observation above a primary energy of $\sim 10^{14}$ eV. Cosmic Rays above $\sim 10^{18}$ eV are called *ultra high energy cosmic rays* (UHECR).

The history of EAS dates back to the late 1930s when the French physicist Pierre Auger first introduced the notation of *extensive cosmic-ray shower* [38]. He and his colleagues could show the existence of EAS with coincidence studies with counters and Wilson chambers partly at sea level and partly in two high altitude laboratories, Jungfraujoch (3500 m) and Pic du Midi (2900 m). With an arrangement of two parallel and horizontal counters placed at progressively increasing distances up to 300 m they searched for coincidences and concluded the existence of primary particles with energies around 10^{15} eV. What is happening in these showers is that nuclear cascades are initiated by cosmic rays of very high energy and many of the products reach the ground before losing all their energy.
EAS can be studied at the surface, at various mountain elevations or even beneath the Earth. The experimentally determined quantities are:

- **Lateral distribution function**
  This expresses the particle density as a function of distance from the shower axis. One differentiates between:
  - Lateral distribution of charged particles in the EAS ($e + \mu$)
  - Lateral distribution of Čerenkov light produced by EAS
  - Lateral distribution of muons generated by pion and kaon decays in the EAS (μ)
- **Longitudinal development**
  This can be determined indirectly by studying the lateral distribution or directly by

observing the atmospheric fluorescence and/or Čerenkov light associated with the passage of particles through the atmosphere.

- **Time distribution of particles arriving at ground**
- **Čerenkov light pulse rise time and width**
  This carries information about the longitudinal development of the shower.
- **Hadronic component**
  This component is concentrated very near the axis and is therefore difficult to study at high energies.

3.1 Development of extensive air showers

The first interaction of the primary cosmic ray with the atmosphere typically occurs at a height of 20-30 km, depending on the energy and mass of the primary particle. Assuming a primary cosmic ray nucleon, mostly kaons and muons together with a leading baryon are produced sharing the primary energy. Due to the large primary energy these secondary particles can again interact with other nuclei and produce new particles. The resulting air shower is composed of three main components as shown in Fig. 3.1:

- Hadronic component
- Muonic component
- Electromagnetic component

One important parameter of the longitudinal shower development is the matter traversed by the shower particles. Known as *slant depth* X it is measured in g/cm^2 from the top of the atmosphere along the direction of the incident nucleon and is related in good approximation[1] to the density profile $\rho(h)$ of the atmosphere by

$$X = \frac{X_v}{\cos\theta} \ ,$$

where X_v refers to the vertical atmospheric depth and is given by

$$X_v = \int_h^\infty \rho(h') \ dh' \ .$$

Cascade equations describe the propagation of particles through the atmosphere. They depend on the properties of the particles, their interactions and on the structure of the atmosphere [16]. In matrix notation one has:

[1] for $\theta \lesssim 60$ deg

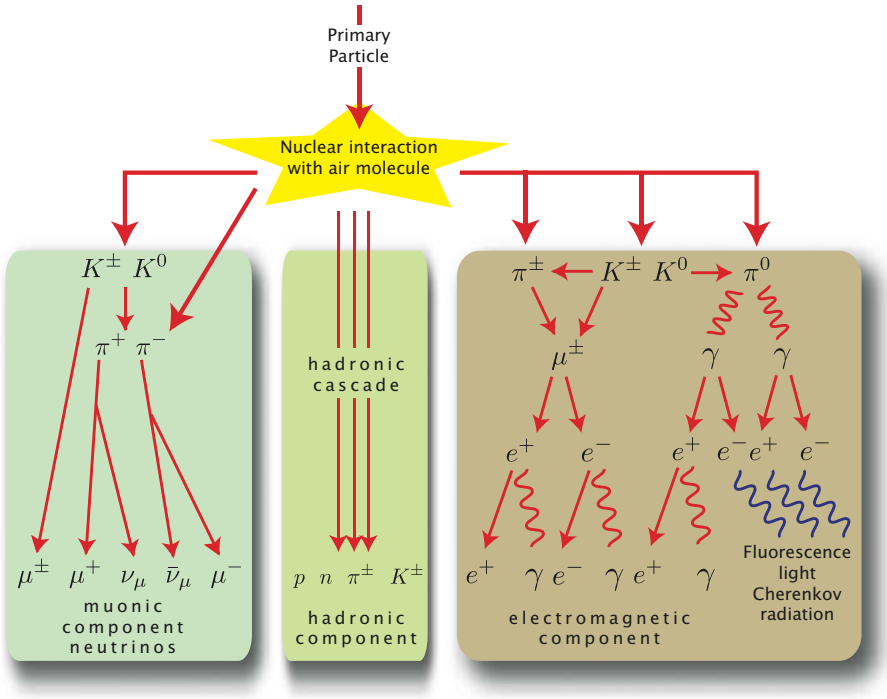

Figure 3.1: Particle content of extensive air showers. Three main components are indicated.

$$\frac{dN_i(E_i, X)}{dX} = \underbrace{-\left(\frac{1}{\lambda_i} + \frac{1}{d_i}\right) N_i(E_i, X)}_{I} + \underbrace{\sum_j \int \frac{F_{ji}(E_i, E_j)}{E_i} \frac{N_j(E_j)}{\lambda_j} \, dE_j}_{II} \; . \tag{3.1}$$

Eqn. 3.1 describes the change of the number of particles of type i and energy E_i in an atmosphere at slant depth X. There are basically two parts:

- **Part I**:
  This term describes the possibility that a particle i disappearing into other types either through interaction with other particles having an interaction length λ_i or through decay with decay length d_i in g/cm^2. It can be understood as a *loss-term*.

- **Part II**:
  This term describes the possibility for creation of a particle of type i through interaction or decay of a particle j. The function $F_{ji}(E_i, E_j)$ is the dimensionless *inclusive cross section* and describes the probability of converting a particle of type j and energy E_j into the desired type i and energy E_i. It can be understood as a *creation-term*.

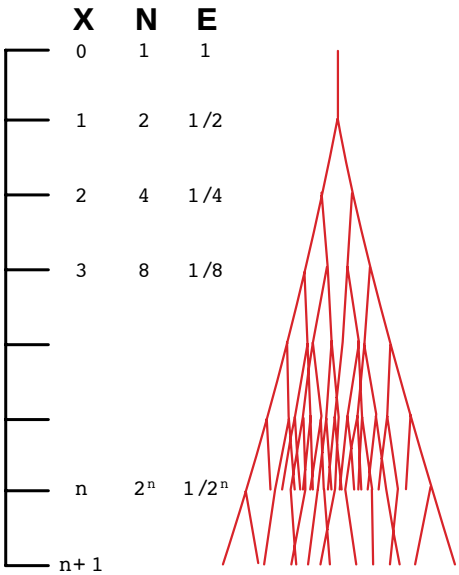

Figure 3.2: Heitler's toy model of cascade development. E symbolizes the energy, N the number of particles and $X = N\lambda$ the depth.

However, since all possible particle types are described with a cascade equation a set of coupled transport equations is needed. A numerical solution is possible and is implemented for instance in CONEX [39].

A simplified way to understand the most important features of cascades has been introduced by Heitler [40]. He describes a cascade of particles of the same type. After an interaction length λ two new particles are created, each carrying half of the primary particle energy $E = E_0/2$ as shown in Fig. 3.2. In each interaction process the number of particles doubles and the energy is shared among them. This sequence continues until the particle energy reaches a critical energy E_c for the splitting process. Below E_c the particles only lose energy, get absorbed or decay. The maximum number of particles is given by

$$N_{\max} = E_0/E_c \ , \tag{3.2}$$

while the depth of maximum is given by

$$X_{\max} = \lambda \frac{\ln(E_0/E_c)}{\ln 2} \ . \tag{3.3}$$

Although the Heitler toy model is extremely simple, it qualitatively correctly describes the shower development up to the maximum of shower development. The basic features of Eqn. 3.2 and 3.3 hold for high energy electromagnetic cascades and also, approximately, for hadronic cascades, namely

$$X_{\max} \propto \ln(E_0) \tag{3.4}$$
$$N_{\max} \propto E_0 \ . \tag{3.5}$$

Still a central issue of air shower physics is to determine the chemical composition of the primary cosmic ray nuclei above 10^{14} eV. The low flux does not allow direct measurements and one has to use measured properties of EAS to determine the composition. To use air showers for this purpose one first needs to know how showers initiated by heavy nuclei differ from those generated by light elements like protons or photons. The distribution of points where the nucleus first interacts inelastically with a target nucleon is crucial for the development of an air shower. The *superposition model* adequates for many purposes. Here one assumes that a nucleus of mass A and total energy E_0 is equivalent to A independent nucleons, each of energy E_0/A and that the distribution of first interactions is the same as if the nucleon had separately entered the atmosphere. Eqn. 3.4 then becomes

$$X_{\max} \propto \ln\left(\frac{E_0}{A \cdot E_c}\right) \ . \tag{3.6}$$

The dependence on A implies that on average showers generated by heavy primaries develop more rapidly than proton showers having the same energy. Unfortunately, there is only a logarithmic dependency on the mass, which makes it difficult to distinguish between masses.
Another distinguishing feature are the fluctuations in their longitudinal development. Heavy nucleons tend to have smaller fluctuations since each nucleus can be described as a beam of many incident nucleons.

3.1.1 Hadronic component

If the primary cosmic ray particle is a nucleon or nucleus, the cascade begins with a hadronic interaction, and the number of hadrons increases through subsequent generations of particle interactions. The depth of first interaction depends on the hadronic interaction length which is ~ 70 g/cm^2 for protons and ~ 15 g/cm^2 for iron nuclei. For a primary proton roughly half of the initial energy is lost in the first interaction for secondary particle production. The position of first interaction strongly influences the subsequent position of the shower maximum $X_{\max}$, which is therefore an important parameter to determine the type of primary particle. Since protons have a much larger interaction length than heavy nuclei, they will have larger fluctuations in the depth of the first interaction and develop deeper in the atmosphere.
Gaisser [41] has parameterized the longitudinal development of hadronic showers as a function of first interaction X_0, depth $X_{\max}$ and size $N_{\max}$ at maximum and the mean free path λ:

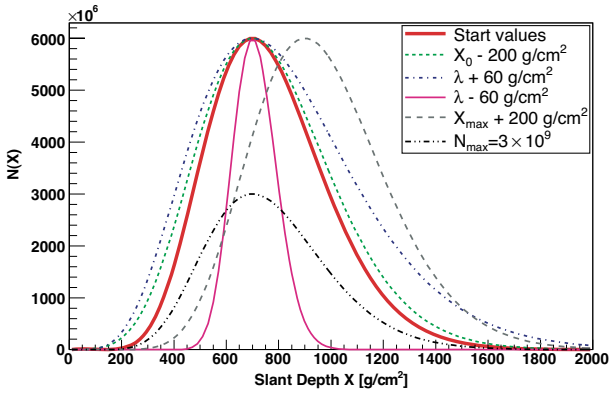

Figure 3.3: Example of a Gaisser-Hillas function with different parameters. The start parameters are $X_0 = 0$, $\lambda = 70$ g/cm^2, $X_{\max} = 700$ g/cm^2 and $N_{\max} = 6 \cdot 10^9$.

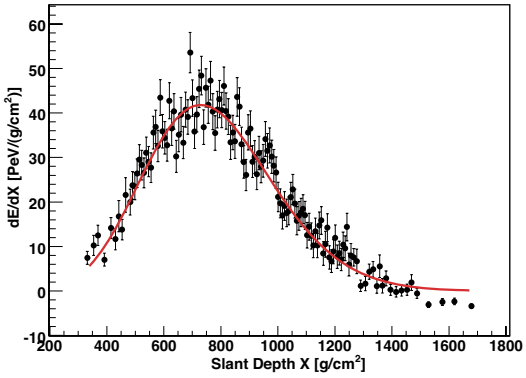

Figure 3.4: Example of a longitudinal profile of the Auger Golden Hybrid event 931431. The red line is the result of a Gaisser-Hillas fit.

$$N(X) = N_{\max} \left(\frac{X - X_0}{X_{\max} - \lambda} \right)^{\frac{X_{\max} - \lambda}{\lambda}} \exp\left(-\frac{X - X_0}{\lambda} \right) \ . \tag{3.7}$$

Eqn. 3.7 is used as a standard fit for the shower longitudinal development and is usually called the *Gaisser-Hillas* formula (cf. Fig. 3.3 and Fig. 3.4).

The basic components in hadron showers are mainly pions and kaons, produced either directly in collisions or as decay products of short living resonances. This shower component is also called *shower core*, because it feeds all other components.

3.1.2 Electromagnetic component

The electromagnetic component of a hadron induced EAS essentially originates from the decay of neutral mesons, mainly pions:

$$\begin{aligned} \pi^0 &\longrightarrow \gamma + \gamma & (\sim 98.8\%) \\ \pi^0 &\longrightarrow \gamma + e^+ + e^- & (\sim 1.2\%) \ . \end{aligned}$$

Electromagnetic cascades can also be initiated directly by high energy photons or electrons. During an interplay between pair production and bremsstrahlung an electromagnetic cascade can develop. In an electromagnetic field of a nucleus N the pair production process can be described as

$$\gamma + N \rightarrow N + e^- + e^+ \ ,$$

whereas bremsstrahlung leads to

$$e^\pm + N \rightarrow N + e^\pm + \gamma \ .$$

The emission of further photons may produce additional $e^\pm$-pairs. This reaction chain proceeds until a threshold energy (critical energy) $E_c = 85.1$ MeV in air is reached. For

$E < E_c$ the ionization energy loss starts to dominate the bremsstrahlung process and the electron is attenuated within one radiation length.

3.1.3 Muonic component

The muonic component of an EAS emerges from the decay of secondary pions and kaons of the hadronic component:

$$\begin{aligned} \pi^{\pm} &\longrightarrow \mu^{\pm} + \nu_{\mu}(\bar{\nu_{\mu}}) \quad (\sim 99.99\%) \\ K^{\pm} &\longrightarrow \mu^{\pm} + \nu_{\mu}(\bar{\nu_{\mu}}) \quad (\sim 63.51\%) \end{aligned}$$

Indeed, the daughter muons are also unstable with typical lifetimes of $\tau_{\mu} \sim 2.2$ μs but taken their experienced time dilatation into account, they mostly reach the ground, unless the energy is smaller than a few GeV. Therefore, the muonic component is also called the hard component of cosmic radiation. On their way to the ground muons are not much deflected by multiple scattering. Their path through the atmosphere is almost rectilinear and makes detection on the ground very helpful for reconstructing the early stage of the shower development. Since the highest energy muons result from high energy pions and kaons, they carry important information about the hadronic interaction at those energies which can be used to test theoretical interaction models. Studying high energy muons near the shower core therefore yields information about the nature of the primary particle.

3.2 Detection techniques

There are several detection techniques for EAS each utilizing special features of air showers ranging from direct sampling of particles in the shower to measurements associated with the emission of fluorescence or Čerenkov light or radio emission. The most common approach is the direct detection of shower particles in an array of sensors spread over a large area (to account for the low cosmic ray flux) to sample particle densities as the shower arrives at the Earth's surface. Another well-established method involves measurements of the longitudinal development of the EAS using fluorescence light produced via interactions of charged particles in the atmosphere. A recently proposed technique uses radar echos from the column of ionized air produced by the shower [42].

3.2.1 Surface arrays

The surface array is comprised of particle detectors, such as Čerenkov radiators or plastic scintillators, distributed with approximately regular spacing. The aim is to measure the energy deposited by particles of the EAS as a function of time. With the energy density measured at the ground and the relative timing of hits in the different detectors one can estimate the energy and direction of the primary cosmic ray.

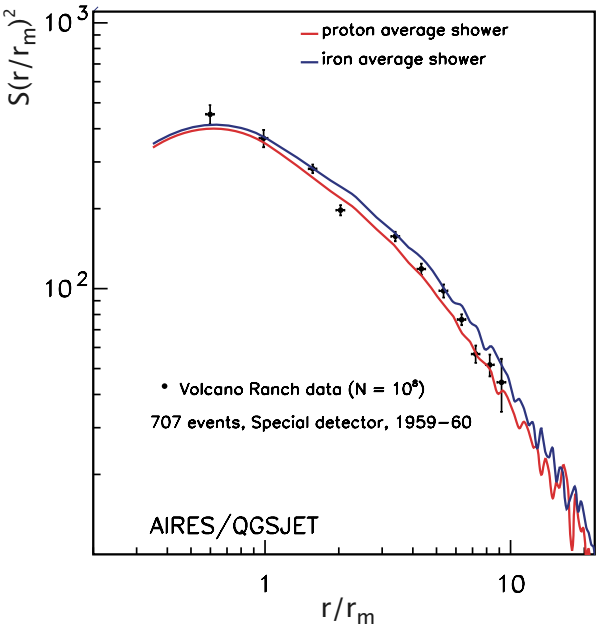

Figure 3.5: Example of an averaged lateral distribution function simulated with AIRES/QGSJET [43] compared to measurements from Volcano Ranch [44] of about 10^{18} eV. r/r_m refers to the distance to the shower axis and S is the lateral distribution of particles at ground (from [45]).

Reconstructing air shower properties involves fitting the lateral distribution function of particle densities at the ground (cf. Fig. 3.5). Clearly, the lateral distribution function has to be determined for each experiment individually. At Haverah Park a good fit to the water Čerenkov lateral distribution was found to be the modified power law function valid for core distances 50 m $< r <$ 700 m, zenith angles $\theta < 45°$ and energies $2 \cdot 10^{17}$ eV$<$ $E < 4 \cdot 10^{18}$ eV [46]

$$\rho(r) = kr^{-(\eta + \frac{r}{4000})} \ , \tag{3.8}$$

where k is the normalization parameter and η is given by

$$\eta = 2.20 - 1.29 \sec\theta + 0.165 \log\left(\frac{E}{10^{17}\ \text{eV}}\right)$$

As already mentioned, the muon content at ground level depends on the composition of the primary cosmic ray. Surface arrays with the ability to distinguish muons from electrons and photons are therefore able to give some hints about the composition of the primary cosmic ray. Another way to gauge the muon content arises from the signal rise time, since the muon content tends to be compressed in time compared to the electromagnetic component.

3.2.2 Fluorescence detectors

Almost 50 years ago Chudakov in the Soviet Union and Suga in Japan realized that nitrogen fluorescence might be used to detect EAS. First measurements of temperature and pressure dependencies of the fluorescence efficiency were made by Greisen and his student Bunner at their Cornell group. They were also the first to build an air shower detector using Fresnel lenses [47], but no air showers were detected in an unambiguous way, because electronic devices were too slow at that time. In 1976 the technique was first successfully demonstrated by the Utah group which was the starting point for founding the Fly's Eye fluorescence detector [48] from 1976.
During the propagation of an EAS through the atmosphere much of the energy is dissipated by exciting and ionizing air molecules (mainly nitrogen) along its path. During the de-excitation process ultraviolet radiation ($\lambda \sim 300 - 400$ nm) is emitted isotropically[2]. This allows detectors to view showers from the side, even at large distances. Although fluorescence light has a very low production efficiency, of the order of 4 photons per meter of electron track, it is possible to detect them over a very large distance. The shower development appears as a rapidly moving spot of light across a night-sky background of starlight, atmospheric air-glow, and man made light pollution. The observed angular motion of the spot depends on both, the orientation of the shower axis and the distance. The measured brightness of the spot indicates the instantaneous number of charged particles present in the shower, but is also affected by Čerenkov light contamination and atmospheric scattering. Since the ratio of energy emitted as fluorescence light to the total energy deposited is less than 1%, low energy showers ($< 10^{17}$ eV) are difficult to detect. Another interference arises from moonlight and observations are only possible on clear moon-less nights, resulting in an average 10% duty cycle.
A fluorescence telescope consists of several light collectors, which image different regions in the sky onto clusters of light sensing and amplification devices. The fluorescence light is collected by photomultiplier tubes (PMTs) positioned approximately on the mirror focal surface. The shower development can then be seen as a long, rather narrow sequence of hit PMTs. With this information the geometry of the shower is determined[3]. Once the geometry in known the longitudinal profile can be determined. This usually involves a three parameter fit to the Gaisser-Hillas function (Eqn. 3.7). The integral of the longitudinal profile is a calorimetric measure of the total electromagnetic shower energy

$$\begin{aligned} E_{\mathrm{em}} &= \alpha_{\mathrm{loss}} \int N(X)\, dX \\ &= \int \frac{dE}{dX}\, dX \ , \end{aligned}$$

where α_{loss} is the average energy loss to the atmosphere which can be approximated as $\alpha_{\mathrm{loss}} \sim 2.2$ MeV g^{-1} cm^2 [49].
The largest cosmic ray event so far was detected by a fluorescence telescope of the Fly's

[2]unlike the very intense Čerenkov light produced by shower particles in air.
[3]A more detailed description of the geometry reconstruction can be found in Sec. 4.5.

Eye experiment with an estimated energy of $3.2 \cdot 10^{20}$ eV and maximum size near a depth of 815 g/cm^2 [50].

3.2.3 Radio detection techniques

A more recent technique to detect air showers utilizes the effect that EAS also emit radio frequency (RF) energy. These radio pulses are produced by several mechanisms, though it is thought that from about 20-100 MHz, the dominant process can be described as coherent synchrotron emission by the electron and positron pairs propagating in the Earth's magnetic field [51]. In the early 1960s RF pulses coincident with EAS were already measured [52] but the promising results from surface arrays and fluorescence eyes abandoned this technique. In the context of next generation digital telescopes more ambitious possibilities have been described (LOFAR [53]). The great potential of a large scale application has been reported by the LOPES project [54]. They also confirmed that the emission is coherent and of geomagnetic origin, as expected by the geosynchrotron mechanism [55].
Another re-explored radio technique may be the detection of radar reflections of the ionization columns produced by EASs [42]. This can be used as an independent technique to detect EASs or as a compliment to existing surface detectors or fluorescence telescopes.

Chapter 4

Pierre Auger Observatory

Currently, the world's largest detecting system for ultra high energy cosmic rays is under construction. Named after the French physicist, the Pierre Auger Observatory was designed to study the upper ($> 10^{18}$ eV) end of the cosmic ray spectrum [56, 57]. The detectors are optimized to measure the energy spectrum, arrival directions and the chemical composition of cosmic rays using two complementary techniques used with success in the past: detecting the nitrogen fluorescence in the atmosphere caused by an extensive air shower and measuring the lateral distribution function of particles that reach the ground. This so-called "hybrid" technique is unique and will enhance the resolution and be valuable in determining systematic errors inherent in both techniques as well as providing more information to determine the particle kind and check hadronic interaction models.
In order to achieve a full sky coverage two instruments, each located at mid-latitudes in the northern and southern hemisphere, are planned or under construction, respectively. The Auger collaboration has started constructing the southern site in Malargüe, located at an elevation of 1400 m in the province of Mendoza, Argentina as shown in Fig. 4.1. To be completed in the second half of 2007 the southern site will cover an area of 3000 km^2 in order to collect a couple of events above 10^{20} eV per year. The northern site is located in southeast Colorado, United States and the construction time is scheduled to be 2009 - 2012 [58]. Once finished, the northern site will cover an area of 10000 km^2 with 4000 water-Čerenkov tanks and additional fluorescence telescopes.

4.1 Surface detector

The surface detector (SD) of the southern array is a ground array covering an area of 3000 km^2 with 1600 water-Čerenkov stations set on a regular triangular grid, with 1.5 km separation between them [57] yielding full efficiency for EAS detection above $5 \cdot 10^{18}$ eV. The communication to the central base station is accomplished through a radio link.
An example of a surface detector is shown in Fig. 4.2. Each station is a cylindrical tank, filled with 12000 liter of purified water, operating as a Čerenkov light detector. The water is contained within a bag that has a high diffuse reflectivity in the wavelength of combined maximum Čerenkov light production, water transmissivity and photocathode sensitivity.

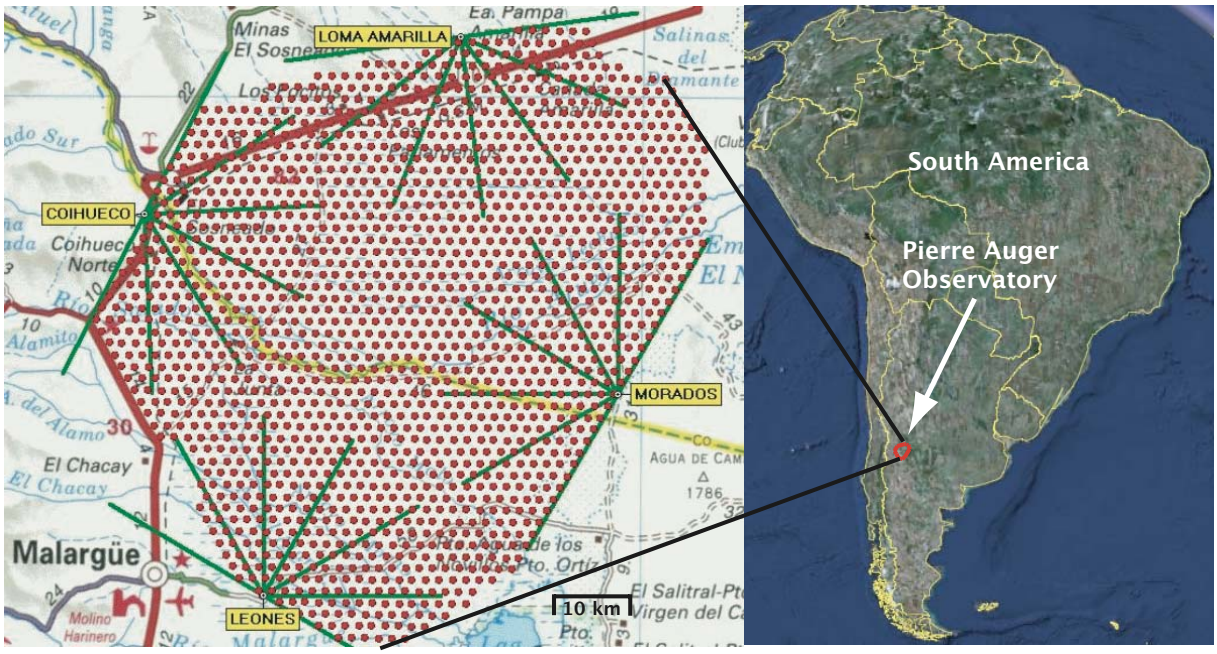

Figure 4.1: A map of the Pierre Auger Observatory with 1600 water tanks (red dots) and four fluorescence telescopes labeled in yellow located next to Malargüe, Argentina.

Three windows are placed on top of the bag where three 9″ PMTs are placed detecting Čerenkov light when particles propagate through the detector. The signals are then passed through filters and read out by a flash analog digital converter (FADC) that samples at a rate of 40 MHz. The digitized data are stored in ring buffer memories and processed by a programmable logic device (FPGA) to implement various trigger conditions [59, 60]. The timing information for each station is received from a GPS system located on each tank with timing resolution < 20 ns [61]. Local electronics as well as the GPS system are powered by two solar panels, combined with buffer batteries.
In order to cope with large amounts of data, the recorded signals are transferred to the Central Data Acquisition System (CDAS) only if a shower trigger has been detected in three adjacent tanks simultaneously. Since the trigger thresholds may change with time, calibration quantities are continuously monitored for each station in the array. The calibration is performed with single cosmic muons by adjusting the trigger rates. This is done with an accuracy of 5% for the PMT gains. For convenience, the number of particles in each tank is defined in units of Vertical Equivalent Muons (VEM) defined as the average charge signal produced by a penetrating down going muon in the vertical direction. The stability and the trigger rates are notably uniform over all detector stations [62].

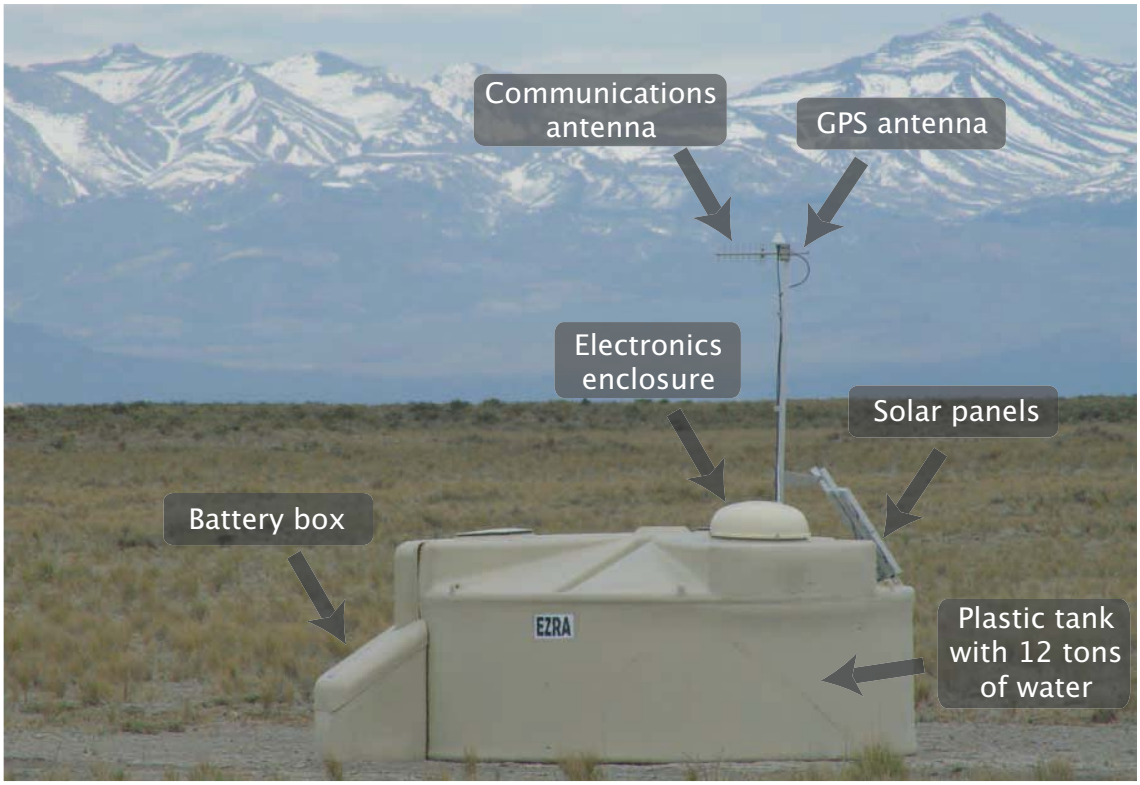

Figure 4.2: View of surface detector "Ezra" within the Argentinean pampa.

4.2 Fluorescence detector

The fluorescence detector (FD) of the southern array is conceived to detect fluorescence light, emitted by de-excitation processes of nitrogen molecules. The fluorescence yield is very low[1], but large imaging telescopes are able to detect this light during clear new to half moon nights, resulting in a duty cycle of $\approx 10 - 15\%$.
The FD is composed of 4 different eyes (named Los Leones, Los Morados, Loma Amarilla and Coihueco) as shown in Fig. 4.1 located at the perimeter of the SD, which enables detection of EAS simultaneously by SD and FD ("hybrid detection"). Each eye consists of 6 independent Schmidt telescopes (bays) each made of a 440 pixel camera, which achieves a covering area of $1.5° \times 1.5°$. They are arranged in a 22×20 matrix to give a field of view of 30° in azimuth and 28.6° in elevation, adding to a 180° view inwards the array of one eye (cf. Fig. 4.1). The fluorescence light is collected by a 12 m^2 mirror with a radius of 3.4 m and reflected to the camera, located at the focal surface of the mirror. The telescopes use a Schmidt optics design to avoid coma aberration, with a diaphragm, at the center of curvature of the mirror. The radius of the diaphragm is 1.1 m including a corrector lens with an inner radius of 0.85 m and outer radius of 1.10 m. The effect of the lens is to increase the light collection area by a factor of two while maintaining an

[1] Approximately 4 photons per meter of electron track [63]

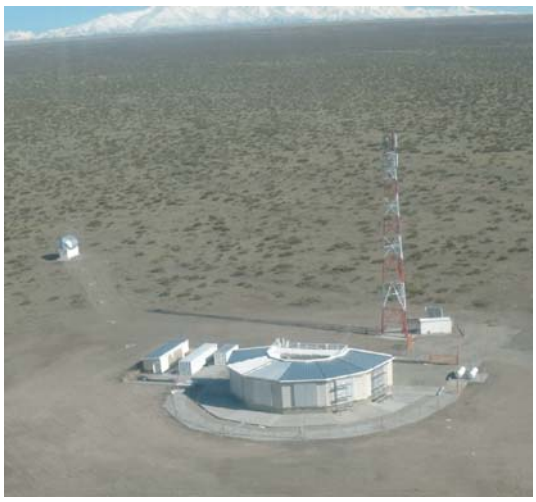

(a) Photo of fluorescence telescope Loma Amarilla taken in Nov. 2006 by Greg Snow.

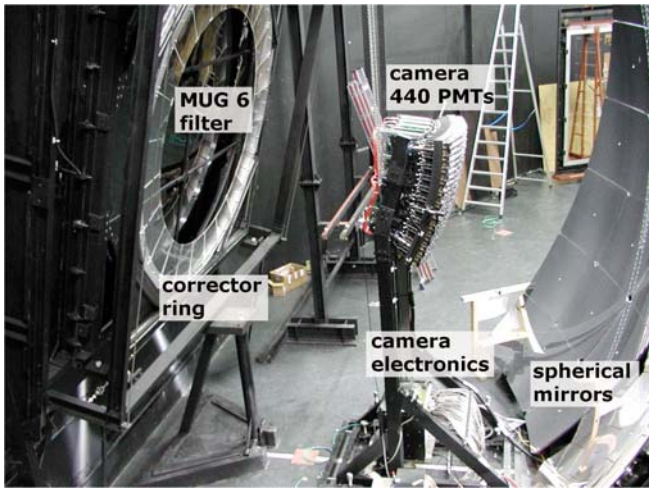

(b) Design of the fluorescence telescope [62].

Figure 4.3: Fluorescence detector of the Pierre Auger Observatory.

optical spot size of 0.5° [64]. To avoid interfering background light each diaphragm has a UV transparent filter that restricts the incoming light to the wavelength range between 300 and 420 nm, which is where the main fluorescence emission lines can be found. To reduce signal losses when fluorescence light crosses PMT boundaries, small light reflectors ("mercedes stars") are placed between the PMTs [65].

The PMT signals are continuously digitized at 10 MHz sampling rate with a dynamic range of 15 bit in total. In order to filter traces out of a random background, a FPGA based multi-level trigger system is used.
To measure air shower energies correctly the fluorescence detectors have to be calibrated and monitored. The **absolute calibration** provides the conversion between the digitized signal (in ADC units) and the photon flux incident on the telescope aperture. This calibration of each telescope is performed three or four times a year. During the calibration a large homogeneous diffuse light source was constructed for use at the front of the telescope diaphragm. This drum shaped source has a diameter of 2.5 m and the emitted light is known from laboratory measurements [66]. The ratio of the drum intensity to the observed signal for each PMT gives the required calibration. The main goal of the **relative calibration** is to monitor short term and long term changes between successive absolute calibration measurements and to check the overall stability of the FD. The atmospheric conditions must be monitored closely since attenuation of the light from the EAS to the telescope due to molecular (Rayleigh) and aerosol (Mie) scattering has to be corrected. Several methods are currently used to determine the effects in the air at any given time during data taking. The relevant parameters are determined by a Horizontal Attenuation Monitor (HAM), Aerosol Phase Function monitors (APF) and a Laser Illuminated Detection And Ranging system (LIDAR) located at each eye (cf. [67, 68]). There are

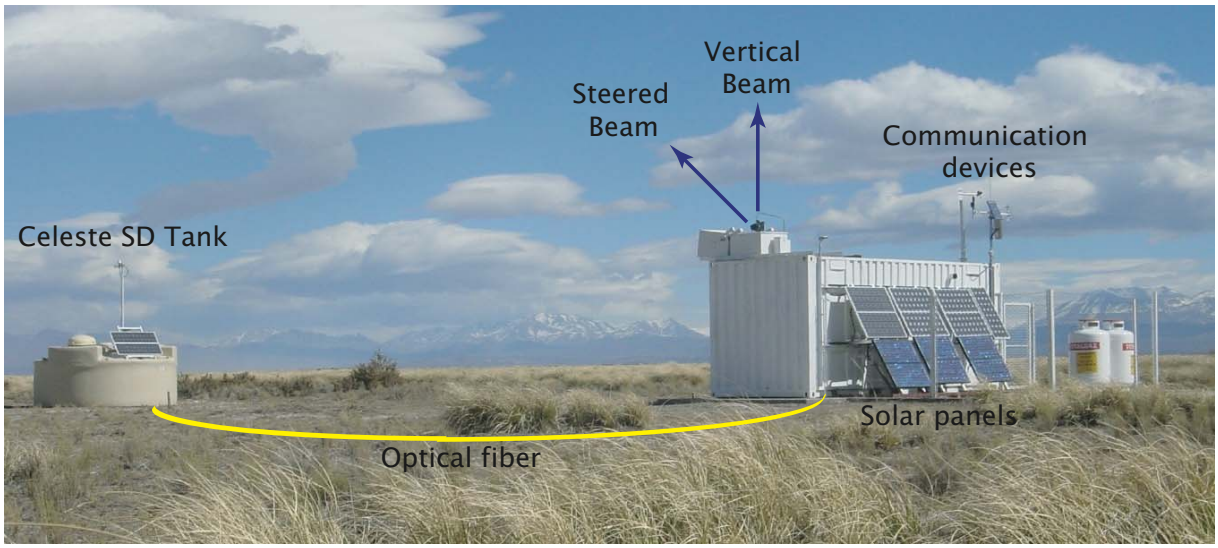

Figure 4.4: The central laser facility [71].

also cloud and star monitors to detect clouds and track stars and any changes in their intensity caused by changing atmospheric conditions.

4.3 Central laser facility

Another complementary measurement of the aerosol vertical optical depth vs. height and the uniformity of the atmosphere across the aperture of the array is provided by the central laser facility (CLF) [69]. It is a steerable automatic system which produces regular pulses of linearly polarized UV light at 355 nm. It is located in the middle of the array, 26 km away from Los Leones (cf. Fig. 4.4). In addition, the CLF provides a laser generated "test beam" for the observatory. This system creates an artificial hybrid cosmic ray event by feeding a signal into a nearby tank (Celeste) through a fiber optics cable. The scattered laser light is intense enough to be registered by all eyes thereby providing a real-time confirmation that the FD eyes are functioning and are able to "see" the array center. The time recorded at each detector is used to measure and monitor the relative timing between SD tanks and FD eyes. The stability of that time offset has been measured by previous measurements to be ~ 100 ns [70].
The possibility to determine the shower axis in mono-mode and single-tank hybrid mode offers the ability to test the accuracy of hybrid reconstruction: For vertical laser shots the location of the CLF could be determined with a resolution of 550 m in mono-mode and after including the timing information of the single water tank, the resolution improved to 20 m without a systematic shift [62].

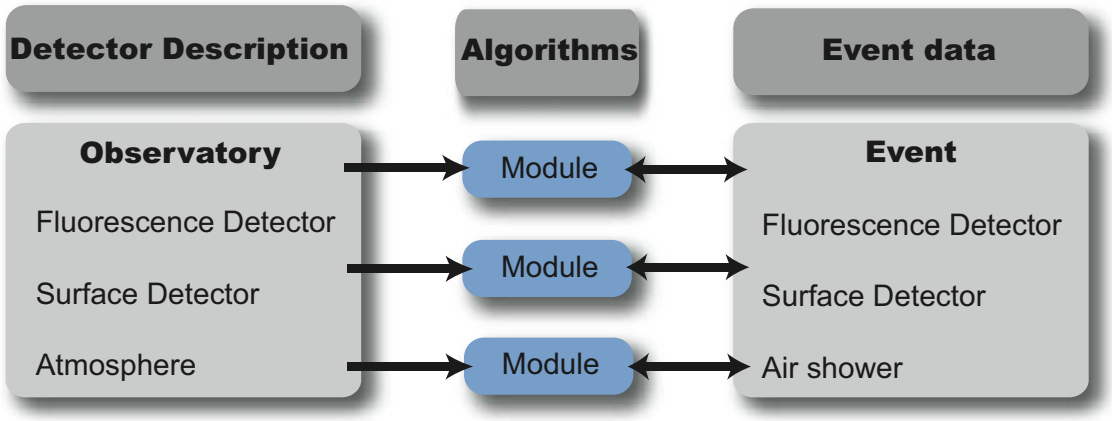

Figure 4.5: General structure of the OFFLINE framework. Simulation and reconstruction are accomplished in different modules and each module is able to read information from the detector description and/or event data, process information, and write the results back into the event (cf. [72]).

4.4 OFFLINE framework

Within the Pierre Auger collaboration, a general purpose software framework has been designed in order to provide an infrastructure to support a variety of distinct computational tasks necessary to analyze data gathered by the observatory [72]. The requirements of this project place strong demands on the software framework underlying data analysis. Therefore, it is implemented in C++ taking advantage of object-oriented design and common open source tools.

The general body comprises three principal parts as shown in Fig. 4.5:

1. **Processing modules**:
   Most tasks of interest can be reasonably factorized into sequences of self contained processing steps. These steps are realized in *modules*, which can be inserted into the framework via a registration macro. The advantage is to exchange code, compare algorithms and build up a wide variety of applications by combining modules in various sequences. In order to steer different modules a *XML*-based run controller was constructed for specifying sequencing instructions. This user friendly environment allows to choose which modules to use and to implement new modified modules.
   XML files are also used to store parameters and configuration instructions used by modules or by the framework itself. A central directory points modules to their configuration files which is created from a *bootstrap* file whose name is passed on the command line at run time.

2. **Event structure**:
   The event data structure acts as the principal backbone for communication between

modules. It contains all raw, calibrated, reconstructed and Monte Carlo data changing for every event. Therefore, the event structure is build up dynamically, and is instrumented with a protocol allowing modules to interrogate the event at any point to discover its current constituents.

3. **Detector description**:
   In contrast to the event structure the detector description is a read-only information. It provides a unified interface from which module authors can retrieve static (stored in *XML* files) or relatively slowly varying information (stored in *MySQL* databases) about detector configuration and performance at a particular time. The requested data is passed to a registry of *managers*, each capable of extracting a particular sort of information from a particular data source. The detector description machinery is illustrated in Fig. 4.6.

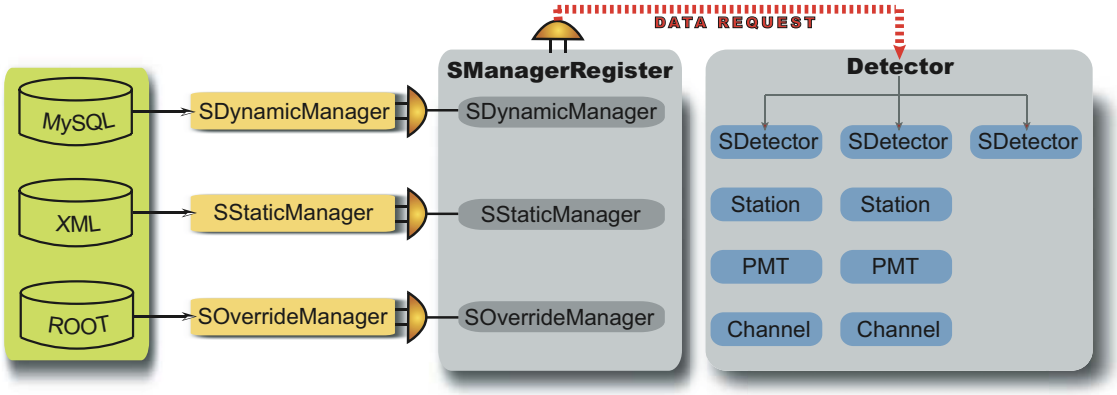

Figure 4.6: Detector description machinery of the OFFLINE framework. An example of SD implementation is illustrated (cf. [72]).

An example of the application of the OFFLINE software in typical simulation and reconstruction tasks can be found in App. A. Here the specific case of hybrid simulation and reconstruction is considered.

4.5 Fluorescence geometry reconstruction

The geometry reconstruction of the shower axis, utilizing fluorescence light of EAS, was first successfully applied at the Fly's Eye experiment [48]. The basic principle did not change much over the years. The emitted fluorescence light along the shower axis appears as a sequential light track propagating across the night sky background starlight, man made civilization light and atmospheric air glow as shown in Fig. 4.7. The "hit pattern" of PMTs determines a plane in space in which the trajectory of an EAS lies. The orientation of the shower axis within that "shower detector plane" (SDP) can be determined by the timing sequence of the light pulse arrival times. Once the geometry is fixed, Rayleigh

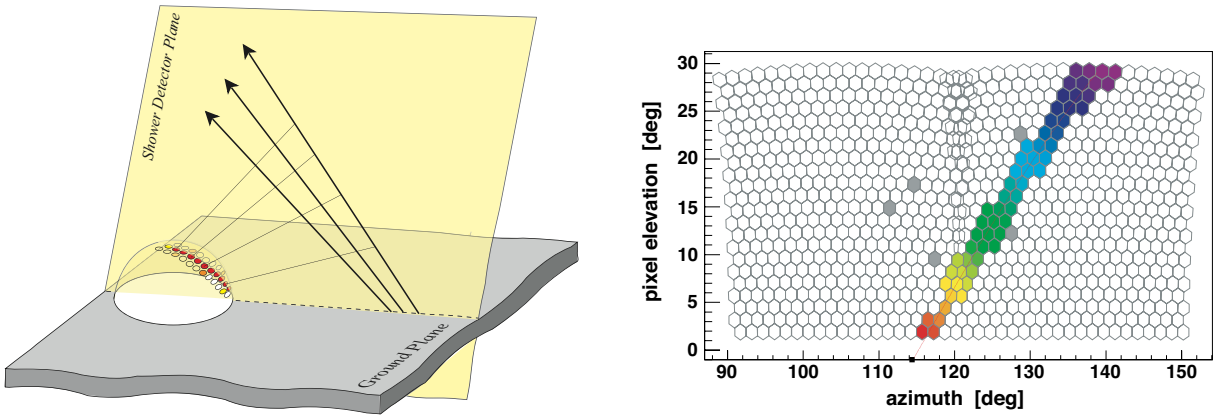

(a) Illustration of the SDP. The geometry is reduced to a planar problem. Different showers still fit to one SDP.

(b) Light track of event 3308259 as seen by two adjacent fluorescence cameras (Los Morados). Different colors indicate the arrival time at the telescope. The filled black square at the bottom of the telescope denotes the position of the station used within the reconstruction (cf. Sec. 4.6).

Figure 4.7: Determination of the SDP.

and Čerenkov light contributions can be subtracted from the apparent brightness of the shower and the energy deposit of the electromagnetic cascade as a function of shower depth is determined.

4.5.1 Shower detector plane

The shower detector plane is defined as the plane, containing the shower axis and the center of the eye. The reconstruction procedure mainly uses the trace of triggered pixels where high signal PMTs are expected to be more reliable than noisy ones. First a two step pre-selection of pixels is done [73]:

1. It is required that the pixel is not isolated in space and time by requiring that valid pixels should not be more than four camera rows or columns away from any other. The barycenter of reconstructed pulses should not be more than 6 μs away from other pixels.

2. It is required that pixel times are correlated with shower candidates

The orientation of the SDP is specified by a unit normal vector $\vec{n}$ referred to as the "SDP vector". Since every plane has two normal vectors, one opposite to each other, a convention is used to remove this ambiguity. The common definition is that the cross product of the SDP vector with the local vertical of the detector points in the direction of the core [74]. For this convention only, the core is defined as the intersection of the shower axis and the detector's horizontal plane. The direction of the shower is not taken

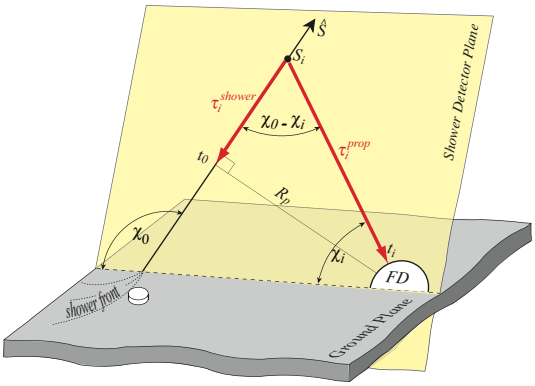

(a) Illustration of the shower / detector geometry.

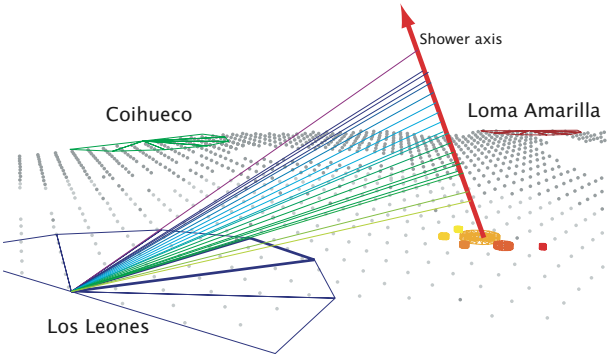

(b) Light track of event 3308445. The timing information is used to determine the fit parameters. This event was also seen by SD-tanks → hybrid event.

Figure 4.8: Illustration of the shower / detector geometry. The fit parameters χ_0, R_p and t_0 are determined by the angular motion of the track.

into account, i.e. a vertical up-going laser shot and a vertical down-going shower at the same core location will have the same SDP. Within a χ^2 minimization the plane that best describes the triggered pixels is determined. The normal vector $\vec{n}$ is obtained using the pointing direction $\vec{r_i}$ of the i^{th} triggered phototube:

$$\chi^2 = \sum_i |\vec{n} \cdot \vec{r_i}|^2 \, w_i \ , \tag{4.1}$$

where w_i is basically[2] the sum of the signal found in pixel i. The accuracy of the SDP reconstruction is described in [76]. It is found, that the SDP vector for a 30 deg track length shower has a 0.08 deg centroidal uncertainty and a 0.5 deg angular uncertainty[3] in accordance to simulations.

4.5.2 Reconstruction of the axis within the SDP

Once the SDP is fixed the geometry of the shower is reduced to a two dimensional problem. In addition to the hit pattern of the PMTs, the timing information is used to fix the direction of the EAS within the SDP. This is achieved by finding the closest distance R_p of the shower axis to the telescope, together with the shower inclination with respect to the SDP (cf. Fig. 4.8). The time t_0 at which the shower passes the closest point to the telescope is used as a reference time.

Within a χ^2 minimization process, the best fit parameters χ_0, R_p and t_0 are determined. The χ^2 function for the fluorescence reconstruction is defined as

[2]There are also some corrections from studies on laser shots [75].

[3]The uncertainty of the SDP vector is given in the shower track coordinate system. The centroidal uncertainty is a translation of the estimated track's centroid perpendicular to the actual track. The angular uncertainty is a rotation of the estimated track about the actual track's centroid. More details about the coordinate system and angle definitions can be found in [76].

$$\chi^2_{fl} = \sum_i \frac{(t_i - t_i^{\mathrm{exp}})^2}{(t_i^{\mathrm{err}})^2} \ , \tag{4.2}$$

where t_i is the measured arrival time, t_i^{exp} the expected arrival time at the telescope, and t_i^{err} the centroid error for the i^{th} pixel viewing towards S_i (cf. Fig. 4.8). This work covers investigations related to both, t_i^{exp} and t_i^{err}. More details about the centroid error t_i^{err} can be found in Sec. 5.1. The expected arrival time t_i^{exp} can be expressed by geometrical considerations. Let τ_i^{shower} be the propagation time from point S_i (light emission point) to the point at reference time t_0 on the shower axis. τ_i^{shower} is then usually expressed as

$$\tau_i^{\mathrm{shower}} = \frac{R_p}{c \cdot \tan(\chi_0 - \chi_i)} \ , \tag{4.3}$$

where c denotes the speed of light and χ_i the viewing angle towards S_i. The propagation time τ_i^{prop} from S_i to the telescope is assumed to be

$$\tau_i^{\mathrm{prop}} = \frac{R_p}{c \cdot \sin(\chi_0 - \chi_i)} \ . \tag{4.4}$$

With (4.3) and (4.4) the expected arrival time becomes

$$\begin{aligned} t_i^{\mathrm{exp}} &= t_0 - \tau_i^{\mathrm{shower}} + \tau_i^{\mathrm{prop}} \\ &= t_0 + \frac{R_p}{c} \left(\frac{1}{\sin(\chi_0 - \chi_i)} - \frac{1}{\tan(\chi_0 - \chi_i)} \right) \\ &= t_0 + \frac{R_p}{c} \tan\left(\frac{\chi_0 - \chi_i}{2} \right) \ . \end{aligned} \tag{4.5}$$

The resulting time vs. angle correlation is shown in Fig. 4.9.

Eqn. 4.5 is the "classical" formula [26] used in past and current fluorescence air shower experiments [11, 77, 78]. However, the validity of this formula is discussed in this thesis and corrections are provided. More details can be found in Chapter 6.

Since the SDP can be reconstructed with high accuracy, the uncertainty mainly arises from the determination of the shower geometry within the SDP (FD-mono). The uncertainty of the fit parameters depends on the particular geometry as well as on the observed track length, e.g. for short track length there may be only insignificant curvature in the tangent function resulting in an ambiguity in the set of fit parameters χ_0, R_p and t_0. This translates directly into an uncertainty of the primary energy E_{prim} since to a good approximation the primary energy is proportional to

$$E_{\mathrm{prim}} \propto L_{\mathrm{fluor}} \propto L_{\mathrm{FD}} \cdot R^2_{X_{\mathrm{max}}} \cdot e^{R_{X_{\mathrm{max}}}/\lambda_{\mathrm{att}}} \ , \tag{4.6}$$

where L_{fluor} denotes the amount of light per unit length produced at shower maximum, L_{FD} the actually received light at the telescope, $R_{X_{\mathrm{max}}}$ the distance to shower maximum from the telescope and λ_{att} the attenuation length of fluorescence light. The quantity

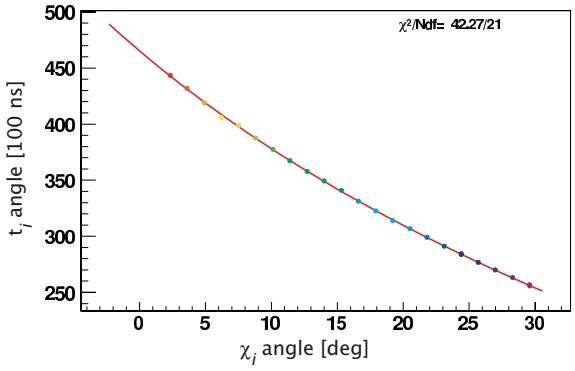

(a) Time vs. angle correlation of event 3375249. The dots represent the measured (χ_i,t_i)-pairs. The different colors indicate the arrival time from purple (early) to red (late). The solid red line represents the timing fit (Eqn. 4.5).

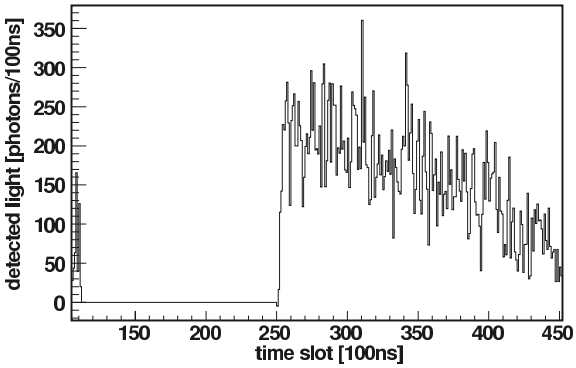

(b) Sum of photon traces for event 3375249.

Figure 4.9: Time-angle correlation together with the sum of photon traces for event 3375249.

$R_{X_{\max}}$ is affected by changes in the parameters χ_0, R_p and t_0. The resulting asymmetric uncertainties are important drawbacks within mono fluorescence reconstruction.

The situation can be improved if the same event is seen by more than one telescope (stereo observations) as shown in Fig. 4.10. The shower axis can then be defined by the intersection between the two reconstructed SDPs. With all 4 FD in operation, the Pierre Auger Observatory will achieve full efficiency for stereo observations at energies above $\sim 2 \cdot 10^{19}$ eV.

4.6 Hybrid geometry reconstruction

One of the key features of the Pierre Auger Observatory is the ability to detect high energy cosmic rays simultaneously by fluorescence telescopes and ground array. This hybrid detection can avoid the aforementioned ambiguities (mono-mode) and provides important crosschecks and measurement redundancy. Much of the hybrid capability stems from the accurate geometrical reconstruction, better than either the ground array detectors or a single telescope. Since 2004 the hybrid data set is growing continuously as shown in Fig. 4.11 The synergy between both techniques can be seen in several examples:

- **Energy spectrum**:
  Due to the 100% duty cycle of the surface detectors together with a huge collecting area the energy parameter $S(1000)$ can easily be calculated for the events. In order to convert $S(1000)$ into cosmic ray primary energy FD data is used, since it uses a near-calorimetric technique for determining energy. This has the advantage of

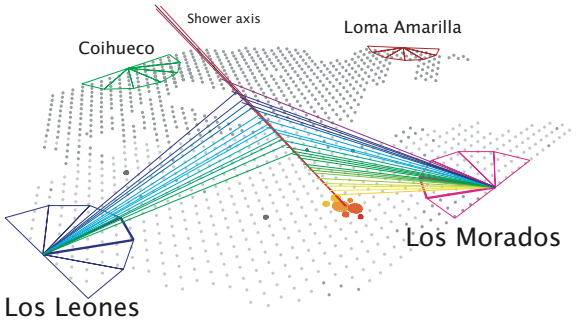

(a) Stereo event 3031623 seen by Los Leones and Los Morados.

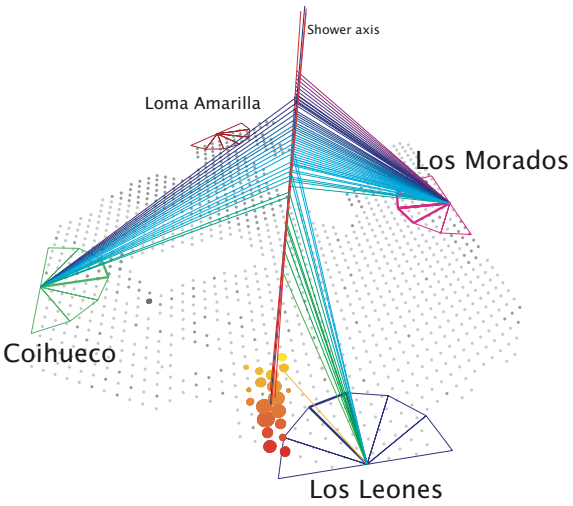

(b) Triple event 3336808 seen by Los Leones, Los Morados and Coihueco.

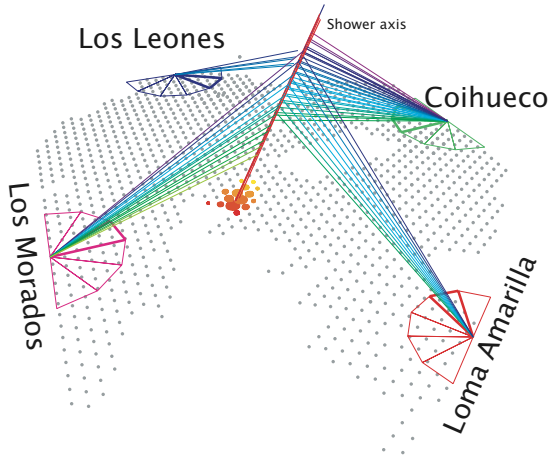

(c) First quadruple event occurred on May 21st 2007 at 09:47:21 UTC with an energy of about 10^{19} eV.

Figure 4.10: Example of some multiple eye events seen by the Pierre Auger Observatory in 2007.

being almost independent of the high energy hadronic interaction models used in simulations.

- **Mass composition**:
  The depth of shower maximum $X_{\max}$ is so far the most important parameter for mass composition studies. Hybrid data can therefore be used to calibrate and cross-check the search for new promising mass sensitive parameters measured by the SD alone [80].

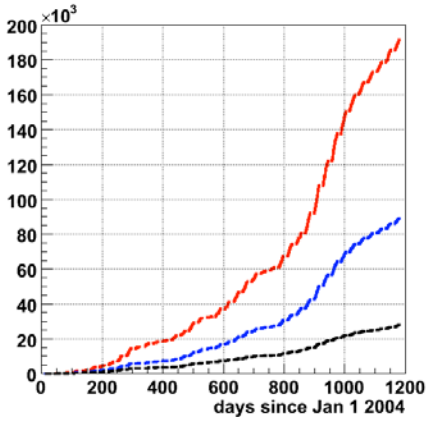

Figure 4.11: Growth of the hybrid data set since 2004. The top line indicates the number of successful reconstructed geometries, the middle line events with $X_{\max}$ in the field of view and the bottom line those events with reconstructed energies $> 10^{18}$ eV (from [79]).

- **Anisotropy studies**:
  Also in anisotropy studies hybrid data can be used to provide a sub-sample of high-precision shower arrival directions which, again, can be used to cross-check SD arrival directions and estimate SD angular resolution.

In order to achieve an improved geometry reconstruction, the SD information of the "hottest" tank is regarded as shown in Fig. 4.12.

The expected timing information from a hit ground station $t_{\mathrm{SD}}^{\mathrm{exp}}$ can be related to the reference time t_0, at which the shower passes the closest point to the telescope, by

$$t_{\mathrm{SD}}^{\mathrm{exp}} = t_0 - \frac{\vec{R}_{\mathrm{SD}} \cdot \hat{S}}{c} \,, \tag{4.7}$$

where $\vec{R}_{\mathrm{SD}}$ is the vector pointing from the telescope to the hottest SD tank and $\hat{S}$ the unit vector of the shower axis pointing towards the origin (cf. Fig. 4.12 (a)). In this expression it is assumed that the shower front is planar. In real situations the shower front curvature must be taken into account.
This additional information can be used as a supplemental data point for the timing fit as shown in Fig. 4.12 (b). The improvement is, that the data point is usually "far away" in viewing angle from triggered FD pixels offering a kind of lever arm for the timing fit. The curvature can be expressed more accurately resulting in a better resolution. The χ^2-function (cf. Eqn. 4.2), which has to be minimized, is then a combination of FD and SD information

$$\chi^2 = \underbrace{\sum_i \frac{(t_i - t_i^{\mathrm{exp}})^2}{(t_i^{\mathrm{err}})^2}}_{\mathrm{FD-Part}} + \underbrace{\frac{(t_{\mathrm{SD}} - t_{\mathrm{SD}}^{\mathrm{exp}})^2}{(t_{\mathrm{SD}}^{\mathrm{err}})^2}}_{\mathrm{SD-Part}} \,, \tag{4.8}$$

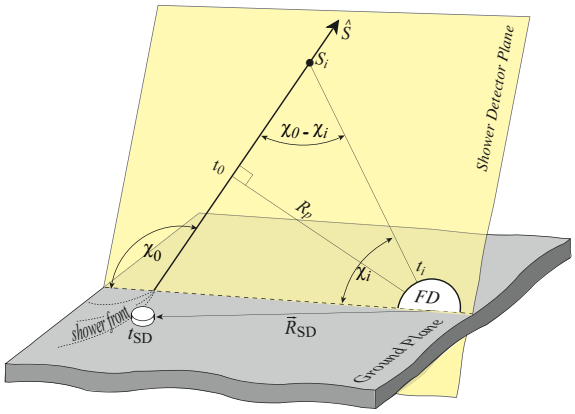

(a) Illustration of the reconstruction of hybrid events.

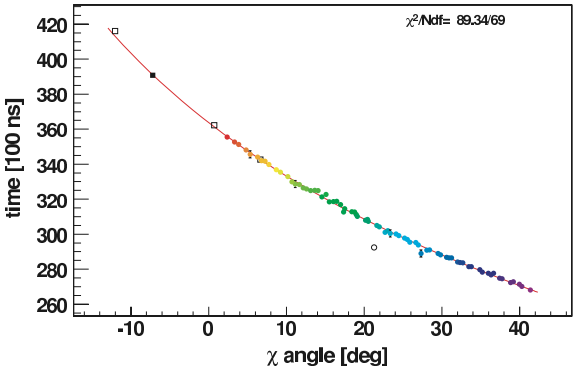

(b) Timing fit of event 3031104. Additional to the FD data the hottest tank (black filled square) is used for the reconstruction. The open squares are also triggered SD tanks, but not included in the reconstruction. Pixels which were used for the SDP determination but dropped during the time fit are symbolized by open circles.

Figure 4.12: Example for golden hybrid events.

where t_{SD} denotes the measured, $t_{\mathrm{SD}}^{\mathrm{exp}}$ the expected timing information of the ground station and $t_{\mathrm{SD}}^{\mathrm{err}}$ the expected uncertainty between t_{SD} and $t_{\mathrm{SD}}^{\mathrm{exp}}$. The directional resolution can hereby be improved to be better than 0.5 deg making sensitive anisotropy searches possible as well as cross-checks of SD direction assignments [79].
Showers that are triggered by the FD and at least three SD stations are called "golden hybrid" events. The geometry of those events can be independently reconstructed by either only the SD or FD information, or by combining this information using a hybrid technique as shown in Fig. 4.13.

Obviously, an accurate synchronization between SD and FD is essential for hybrid analyses. The location of the shower core using the hybrid technique is sensitive to the SD-FD time synchronization. If the FD time is delayed, in relation to the SD time, the reconstructed core will be systematically pushed away from the FD location and vice versa. More studies on the SD/FD offset can be found in Section 6.6.

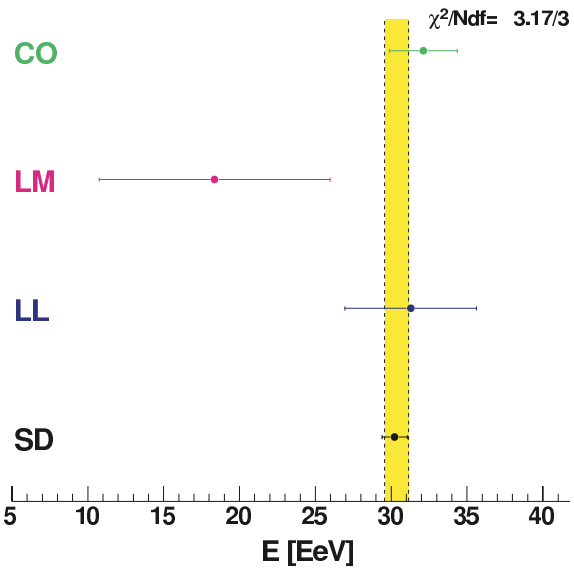

(a) The shower energies reconstructed by three eyes and the surface array of event 3351072. The yellow band represents a weighted average of the sub-detectors. Its width combines the statistical uncertainty σ_E.

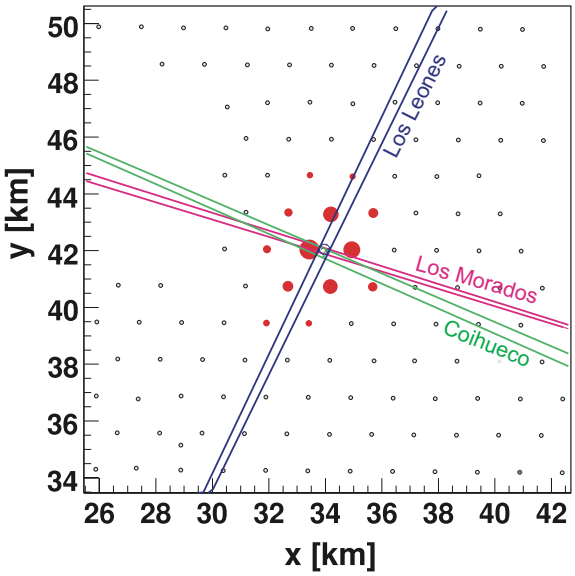

(b) Two dimensional plot of the surface array of event 3351072. Stations used for SD reconstruction are shown in red colors. Two lines from each FD with a successful FD reconstruction show the $\pm 1\sigma$ projections of the SDPs on the array plane.

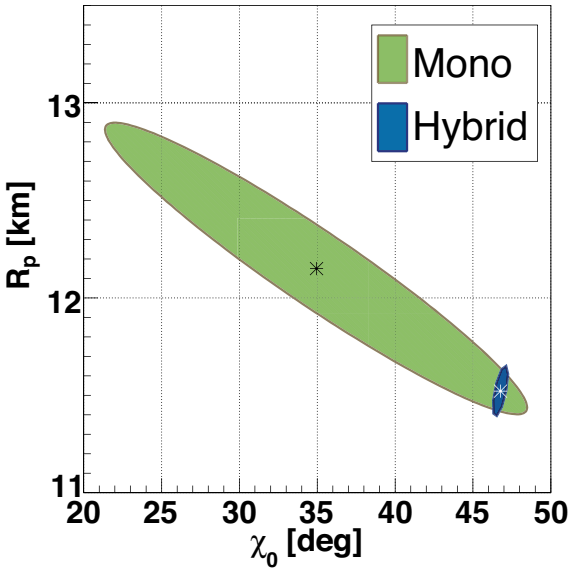

(c) Solution for the axis for mono and hybrid reconstruction (1σ accuracy). The large uncertainty of the monocular reconstruction is broken using the timing information from the surface detector. The stars indicate the solution that minimize the χ^2 for the axis reconstruction (cf. [81]).

Figure 4.13: Advantages of the hybrid technique.

Chapter 5

Parameterization of the Pulse Centroid Uncertainty

The determination of the exact fluorescence pulse centroid and its error is an essential step towards an accurate geometry reconstruction. Uncertainties propagate directly into the reconstructed primary energy and affect the reconstruction procedure. The current determination of the centroid error is not optimal and some attempts are made to revise certain drawbacks. As an introduction the standard reconstruction of fluorescence signals is revisited and the determination of the pulse centroid and its uncertainty is discussed following some attempts for a new parametrization.

5.1 Standard reconstruction of fluorescence signals

Based on the experience of the Utah Flys's Eye experiment [48], the reconstruction procedure is divided into several reconstruction steps accomplished in different modules with intuitive names:

- **FdCalibrator**:
  Each pixel has a different individual noise level, that has to be determined and corrected. The first step is to identify the baseline, corresponding to the mean noise level of one pixel. Usually, a period of 200 time bins of the stored ADC-trace[1] where no signal is present is used to determine that baseline and noise fluctuations. After subtracting the baseline from the trace, the ADC-counts are converted into number of photons by multiplying the calibration constant k_i for each pixel i. The ADC-trace $F_i(t)$ is converted into the photon-trace $N_{\gamma_i}(t)$

$$N_{\gamma_i}(t) = k_i \cdot F_i(t) \ . \tag{5.1}$$

- **FdPulseFinder**:
  The ADC-counts are triggered by the data taking software in 100 ns bins. The

[1] ADC-counts as a function of time, binned by 100 ns.

aim of the FdPulseFinder module is to determine the pulse centroid (related to the detection of fluorescence light) from the ADC-counts. The basic procedure is a signal over noise (S/N) maximization algorithm. The first step is the boundary determination of the suspected pulse. Starting from the time of First Level Trigger, the start and stop time bin are shifted as long as a maximal S/N ratio is achieved

$$\mathrm{S/N} = \frac{\mathrm{charge}}{\sqrt{\Delta t} \cdot \mathrm{noise}} \rightarrow \max \ , \tag{5.2}$$

where "charge" is the total integrated signal within the assumed pulse length, Δt is the time difference between start and stop time bin in units of 100 ns bins and

$$\mathrm{noise} = \sqrt{\frac{\sum_j \left(N_\gamma(j) - \overline{N_\gamma}\right)^2}{\Delta t}} \ , \tag{5.3}$$

where $\overline{N_\gamma} = \mathrm{charge}/\Delta t$ is the mean of the number of photons per pulse. After the minimization the pulse duration[2] is usually rather small and therefore extended until the start and stop signal is below the noise level. In order to reject accidental noise pixels, a S/N threshold greater than 5 is set.
The pulse centroid is determined by the trace algorithm "centroid". This is basically a loop over the pulse duration bins j setting the centroid time t_i for pixel i to be

$$t_i = \frac{\mathrm{moment}}{\mathrm{charge}} = \frac{\sum_j N_{\gamma i}(j) \cdot (j + 0.5)}{\sum_j N_{\gamma i}(j)} \ . \tag{5.4}$$

The FD timing uncertainty t_i^{err} (centroid pulse time uncertainty) follows a suggestion of Stefano Argirò and Andrea de Capoa [82] and is currently [83] calculated with an algorithm illustrated in Table 5.1 and Fig. 5.1:

If	duration	$\leq$	200	$\rightarrow t_i^{\mathrm{err}} = 200$
If	duration	$>$	200 and < 500	$\rightarrow t_i^{\mathrm{err}} = 100$
If	duration	$\geq$	500	$\rightarrow t_i^{\mathrm{err}} = 50$
If	$\frac{\mathrm{charge}}{\frac{\mathrm{duration}}{\mathrm{timebinsize}} \cdot \mathrm{noise}}$	$>$	7	$\rightarrow t_i^{\mathrm{err}} = t_i^{\mathrm{err}} \cdot 0.5$
If	$\frac{\mathrm{charge}}{\frac{\mathrm{duration}}{\mathrm{timebinsize}} \cdot \mathrm{noise}}$	$>$	2 and < 3	$\rightarrow t_i^{\mathrm{err}} = t_i^{\mathrm{err}} \cdot 2$
If	$\frac{\mathrm{charge}}{\frac{\mathrm{duration}}{\mathrm{timebinsize}} \cdot \mathrm{noise}}$	$<$	2	$\rightarrow t_i^{\mathrm{err}} = t_i^{\mathrm{err}} \cdot 4$

Table 5.1: Current algorithm to determine the pulse centroid uncertainty. A few if-conditions are set to estimate the uncertainty. The term "duration = $\Delta t \cdot$ timebinsize" denotes the length of the pulse, timebinsize = 100 ns , "charge" the total integrated signal and noise the RMS of the pixel.

[2] duration = $\Delta t \cdot$ timebinsize denotes the length of the pulse. The timebinsize is set to 100 ns.

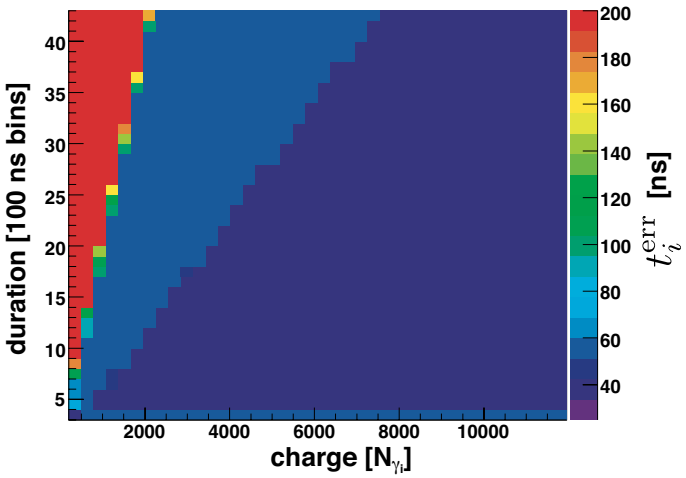

Figure 5.1: Illustration of the centroid uncertainty parametrization as a function of charge and duration as it is currently used. Different colors indicate the uncertainty of the centroid. The noise was set to 25 according to the average noise distribution.

- **FdSDPFinder**:
  This module determines the SDP of the shower. A pattern recognition algorithm is used to determine all pixels triggered by the EAS and to suppress noise pixels. The extant pixels together with their pointing directions are used to determine the SDP by minimizing Eqn. 4.1.

- **FdAxisFinder**:
  The pointing direction of pixel i is translated into an angle χ_i. The geometry within the SDP is accomplished by minimizing Eqn. 4.2. More details about this reconstruction step can be found in Section 4.5.2.

- **FdApertureLightFinder**:
  The aim of this module is to find the total light received at the aperture of the fluorescence telescope. Again, a S/N maximization algorithm is used for finding the optimal width ξ of the shower image on the camera (cf. discussion in [84]). Once having the optimal ξ, one can derive the number of photons at the telescope aperture as a function of time.

- **FdProfileFinder**:
  The two previous modules calculate the geometry of the shower and the light measured at an angle χ_i of the detector. The FdProfileFinder uses this information to determine the light emitted at the shower position. Clearly, a precise knowledge of atmospheric conditions as well as measured Rayleigh and Mie attenuation lengths are essential ingredients for that calculation. Having a parametrization of the atmosphere for the time of the measurement one can translate this profile into the more meaningful longitudinal profile which is a function of traversed atmospheric depth

$N(X)$. Finally, this profile can then be transformed into the energy deposit profile (energy deposited as a function of traversed matter dE/dX) using the measured fluorescence yield in air.

- **FdEnergyFinder**:
  In order to find the total energy of the EAS one has to extrapolate from the measured sequence of the shower towards undetected parts. This is usually done by fitting a Gaisser-Hillas parametrization to the profile as already explained in Sec. 3.1.1.

- **FdCherenkovFinder and FdCherenkovSubtracter**:
  Within the shower development high energy charged particles are generated traveling faster than the speed of light in the surrounding medium resulting in emission of Čerenkov light along their path. Due to scattering processes this may lead to a light contribution at even large observation angles and has to be taken into account. The standard reconstruction algorithm for determining the profile starts by assuming that no Čerenkov contamination exists. This profile is fitted with a Gaisser-Hillas function and the emission of Čerenkov light is estimated and propagated towards the detector and then subtracted from the measured light flux. The new light flux is used for a second profile fit. This procedure of profile reconstruction and light subtraction is then iterated ten times.

The last named iteration procedure and the profile reconstruction using $N(X)$ has some disadvantages [85] and other attempts are made to avoid these drawbacks e.g. by using a non-iterative procedure using matrix algebra [85], which is currently adopted in the OFFLINE software. Within this thesis the resultant FdProfileReconstructorKG module was used to take advantage of these improvements. One important improvement is also, that statistical uncertainties of the reconstructed total energy and shower maximum are evaluated by a thorough propagation of the uncertainties of the measured light flux, the shower geometry and invisible energy correction.

5.2 Motivation for a new pulse centroid uncertainty

As can be seen in Table 5.1 the pulse centroid uncertainty is determined by a couple of if-conditions using mainly charge, duration and noise of the pulse. The situation is sketched in Fig. 5.2. For long durations a small uncertainty is assumed, which is not a directly obvious choice. One would expect fluorescence light coming from far away showers to produce long and rather flat pulses. Since the determination of the centroid is more difficult for those pulse shapes the uncertainty should be larger and not smaller. After this crude setting of the pulse uncertainty utilizing its duration, it is weighted according to the charge of the pulse. Here it is assumed that pulses with a high charge produce smaller uncertainties.
The estimation of the pulse centroid uncertainty should satisfy the following requirements:

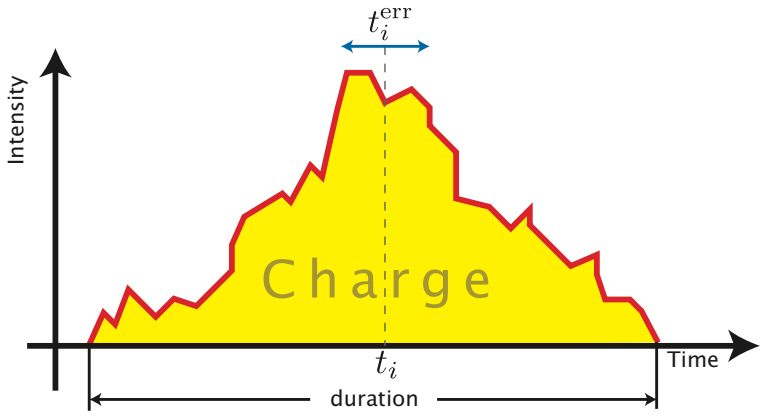

Figure 5.2: Illustration of the pulse centroid. The yellow area under the pulse represents the charge.

- A way to test the uncertainty estimations is given by the χ^2 distribution of the timing fit (cf. Eqn. 4.8). The χ^2 distribution per degree of freedom[3] is expected to center around unity.
- χ^2 per degree of freedom should be independent of other parameters like energy, distance to shower maximum, R_p and so forth, so that finding any such correlation indicates residual shortcomings.
- The uncertainty estimation should be parameterized in a continuos way.

A first attempt to test the algorithm is made using simulated data. The shower sample consists of 1800 proton showers from the CORSIKA-Lyon database [86] with energies of 10^{18}, 10^{19} and 10^{20} eV and zenith angles of 0, 45 and 60 deg. In each energy-theta bin are therefore 200 simulated showers as shown in Table 5.2.

$\theta \downarrow E \rightarrow$	10^{18} eV	10^{19} eV	10^{20} eV
0 deg	200	200	200
45 deg	200	200	200
60 deg	200	200	200

Table 5.2: Simulated data as used in this analysis.

The showers have been simulated with *OFFLINE v2.0-drevil* in a slice of 30 deg in the field of view of bay 4 of the Los Leones telescope. The core distances are uniformly distributed with an energy dependent maximal distance to the telescope[4]. The quality

[3]The number of degrees of freedom is N_{df}=nPixels-3, cf. App. B.1.
[4]The maximal core distances were set to 17 km for 10^{18} eV shower, 35 km for 10^{19} eV shower and 48 km for 10^{20} eV shower.

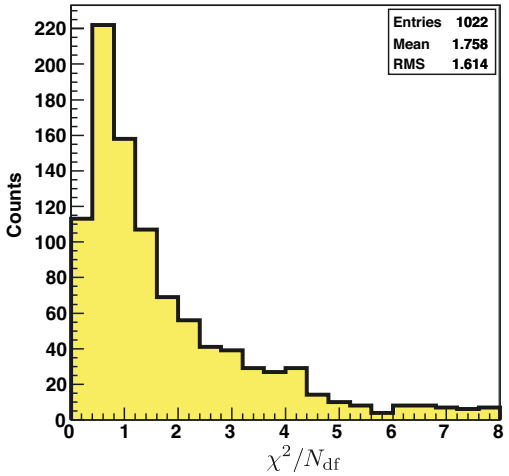

Figure 5.3: χ^2 distribution of the described simulated data. With a mean of 1.76 the uncertainties are underestimated.

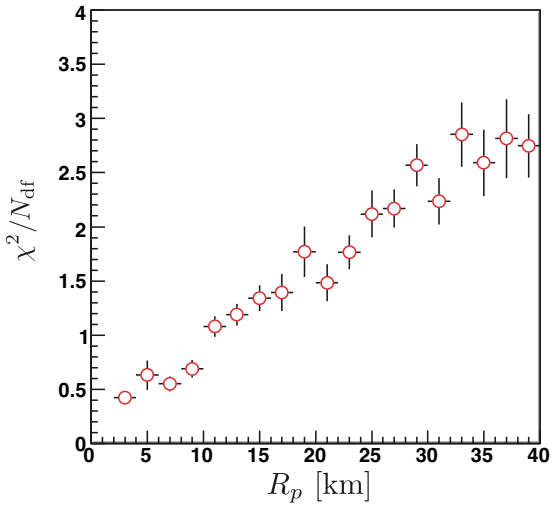

Figure 5.4: χ^2 as a function of R_p. The pulse centroid uncertainty is underestimated for showers with large R_p i.e. far away showers and overestimated for close ones.

cuts as shown in Table B.1 (App. B.2) were used.
Fig. 5.3 illustrates the timing χ^2 per degrees of freedom using the old estimation of the centroid given in Table 5.1 and Fig. 5.4 χ^2/N_{df} as a function of R_p. One can see that the pulse centroid uncertainties are underestimated with a mean of 1.76. This effect is larger for distant showers where the pulse shape is more flat with a long duration. This already known effect [85] can be reduced in OFFLINE by enlarging the errors by a factor $\sqrt{\chi^2/N_{\mathrm{df}}}$ as suggested by the particle data group [87].

5.3 Finding a new parametrization

5.3.1 First approach

At this stage of the reconstruction where the pulse centroid and its uncertainty is calculated, the geometry of the shower is not yet determined. Apart from the measured pulse time t_i, only charge, duration and noise of the pulse is available. The first attempt aims to parameterize the uncertainty as a function of charge and duration [88] as shown in Eqn. 5.5.

$$t_i^{\mathrm{err}} = f(\mathrm{charge}) \cdot g(\mathrm{duration}) \cdot w_i \ , \tag{5.5}$$

where f and g are fitting functions described later in this paragraph and w_i is a weighting factor. To find an appropriate fitting function, $f(\mathrm{charge})$ differences between the measured pulse centroid t_i and expected pulse centroid t_i^{exp} (cf. Eqn. 4.5) are plotted vs. the charge

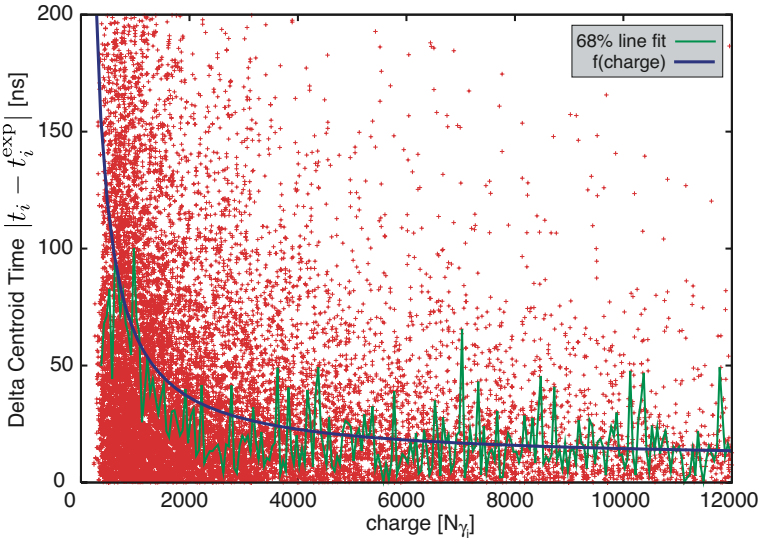

Figure 5.5: Timing difference as a function of charge. The red dots represent the timing difference for just one pixel in an event, the green line indicates the result of the 1σ deviation and the blue line is the fit to the green line.

of the pulse. This is shown in Fig. 5.5. In order not to bias the results with badly reconstructed events this plot only uses events which passed all quality cuts. As one can see, the expected timing uncertainty is large for pulses with small charge. Now, the optimal t_i^{err} as a function of charge is searched. One is interested in a 1σ deviation of the data. For this purpose, the charge axis is divided between 350 and 12000 $[N_{\gamma_i}]$ into bins with a binsize of 50 $[N_{\gamma_i}]$, which is indicated by the green line in Fig. 5.5. Below that line 68% of the data can be found. The green line is now fitted with a fitting function f:

$$f(\text{charge}) = \frac{f_1}{\text{charge} - f_2} + f_3 \ , \tag{5.6}$$

where $f_1 = 55000$, $f_2 = -10$ and $f_3 = 9$ are fitting parameters. The blue line in Fig. 5.5 indicates the result of the fit.

The same procedure is performed to find the fitting function g. The corresponding timing uncertainty as a function of duration is shown in Fig. 5.6. The duration is given in 100 ns bins. The 1σ fit (green line) indicates, that long durations produce rather large uncertainties. Here, a linear relationship between timing uncertainty and duration is assumed:

$$g(\text{duration}) = g_1 \cdot \text{duration} + g_2 \tag{5.7}$$

with $g_1 = 6.85$ and $g_2 = 23.97$. The resulting fit function is also shown in Fig. 5.6. For durations < 400 ns a constant uncertainty of 20 ns is assumed. Combining Eqn. 5.6 and Eqn. 5.7 the final uncertainty is given by

$$t_i^{\text{err}} = \left(\frac{f_1}{\text{charge} - f_2} + f_3 \right) \cdot (g_1 \cdot \text{duration} + g_2) \cdot w_i. \tag{5.8}$$

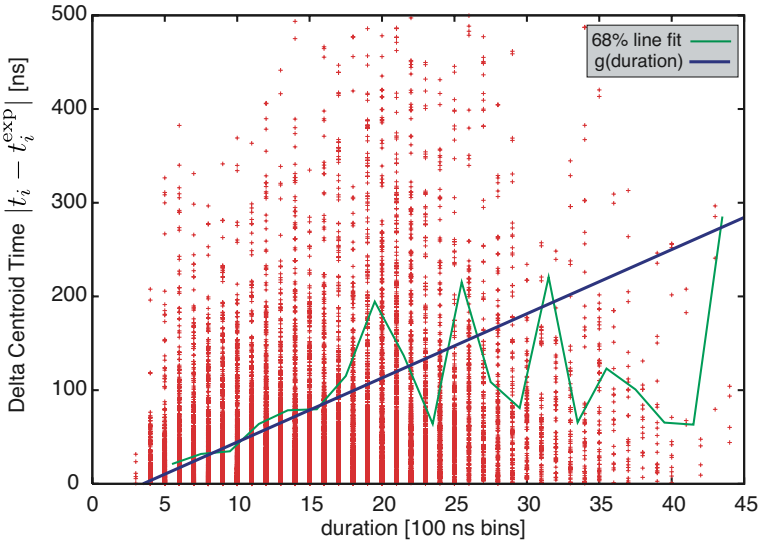

Figure 5.6: Timing difference as a function of duration. The red dots represent the timing difference for just one pixel in an event, the green line indicates the result of the 1σ deviation and the blue line is the fit to the green line.

In the following the weighting factor w_i is set to $w_i = 1/37$ to give $\chi^2/N_{\mathrm{df}} \approx 1$. Fig. 5.7 indicates the uncertainty parametrization. The application to data can be found in Sec. 5.4.

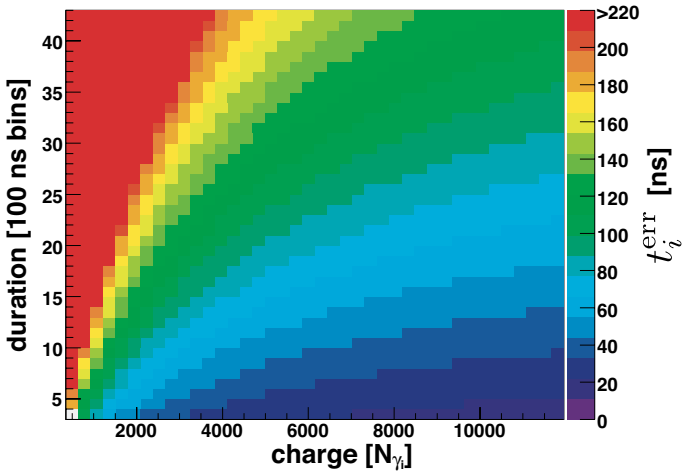

Figure 5.7: Illustration of the centroid uncertainty parametrization as a function of charge and duration for the first approach. Different colors indicate the uncertainty of the centroid.

5.3.2 Second approach

The previous attempt assumed a proportionality of

$$t_i^{\mathrm{err}} \propto \frac{\mathrm{duration}}{\mathrm{charge}}$$

and 6 degrees of freedom for determining the pulse centroid uncertainty. Another parameterization possibility arises using the more physical proportionality

$$t_i^{\mathrm{err}} \propto \frac{\mathrm{duration}}{\sqrt{\mathrm{charge}}} \ ,$$

resulting in a parametrization according to

$$t_i^{\mathrm{err}} = \frac{\mathrm{duration}}{\sqrt{\mathrm{charge}}} \cdot q_i \tag{5.9}$$

with just one degree of freedom q_i. To center the reduced χ^2 around one this factor is set in a first effort to $q_i = 222$ as illustrated in Fig. 5.8.

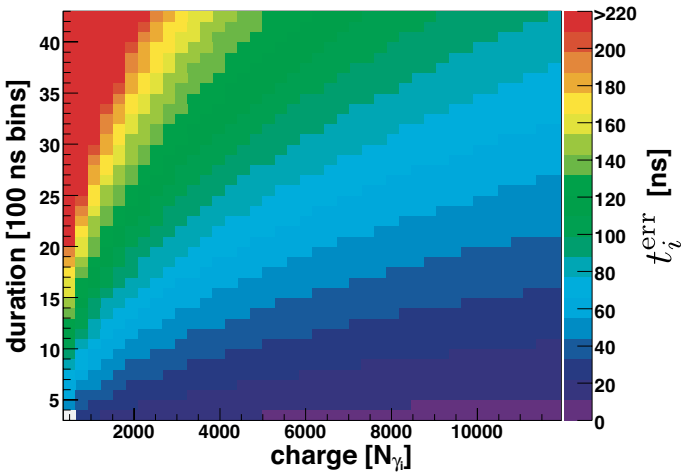

Figure 5.8: Illustration of the centroid uncertainty parametrization as a function of charge and duration for the second approach. Different colors indicate the uncertainty of the centroid.

5.4 Application to data

In the following, the aforementioned parametrizations are tested on 1800 simulated events discussed above. All these events were reconstructed three times once using the "RAW" algorithm, the first approach "ATT1" and the second approach "ATT2" to determine the pulse centroid uncertainty. The corresponding reduced χ^2 distribution are shown in

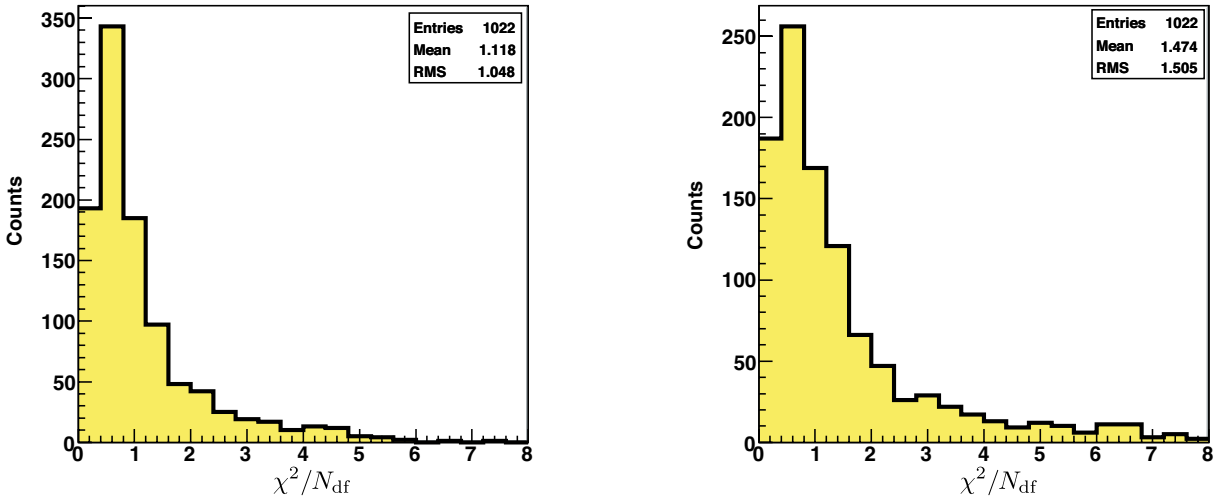

(a) χ^2 distribution for ATT1.

(b) χ^2 distribution for ATT2.

Figure 5.9: Histogram χ^2 distribution for simulated data for ATT1 and ATT2.

Fig. 5.9. Since the mean of the distribution can be "steered" by free parameters, the independence to other shower parameters is more important. The correlation to R_p (cf. 5.4) is shown in Fig. 5.10. One can see that the first approach produces a much weaker dependence on R_p than the other one. Also for very low R_p the reduced χ^2 tends to center around 1. In order to identify the showers with large reduced χ^2 the φ_{axis} dependency is shown in Fig. 5.11. In Fig. 5.11 (d) one can see that the uncertainties for near vertical shower are quite well estimated without any shift for different algorithms. Fig. 5.11

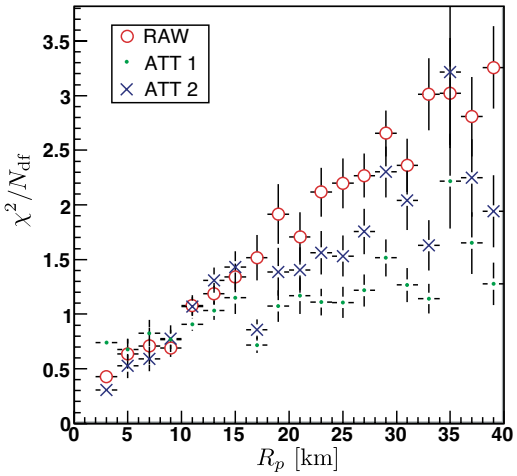

Figure 5.10: Reduced χ^2 as a function of R_p for different centroid uncertainties. The red cycles indicate the old parametrization, the green dots and blue crosses ATT1 and ATT2, respectively.

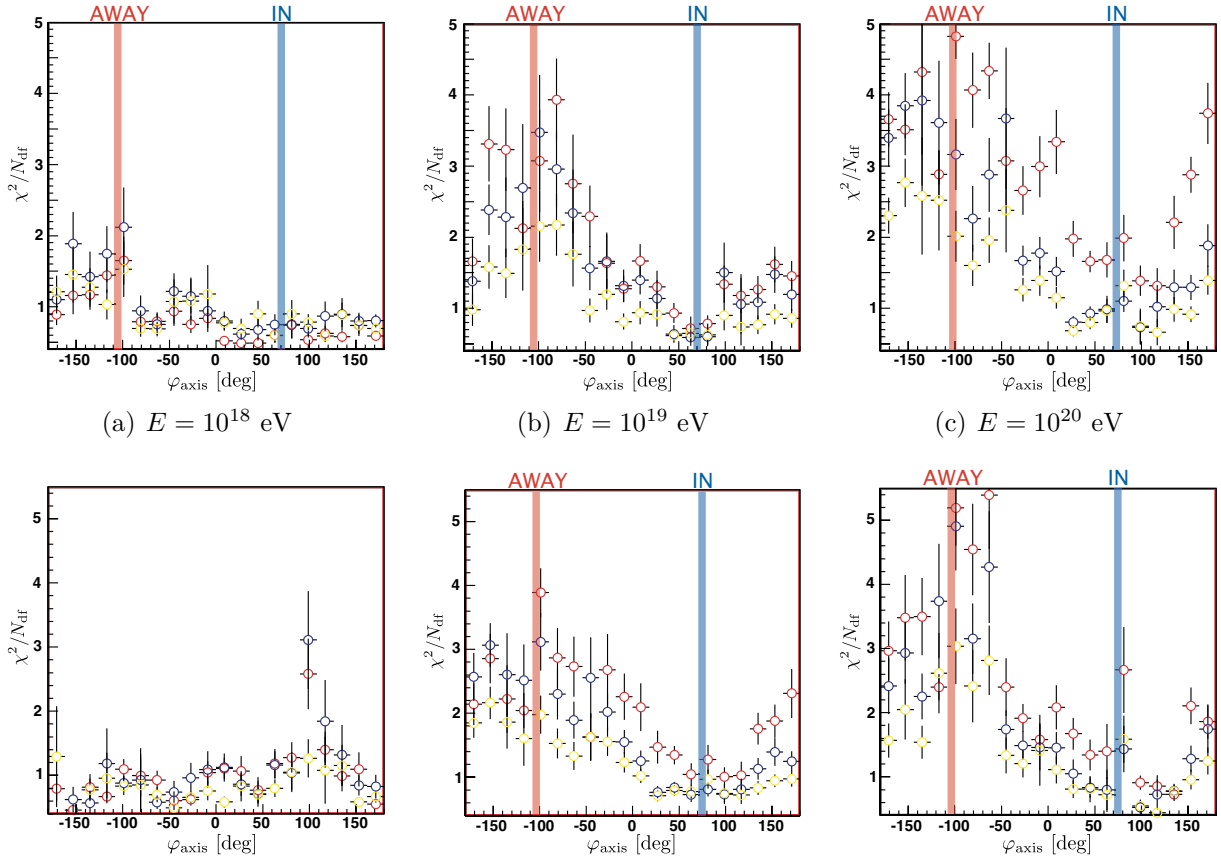

(a) $E = 10^{18}$ eV (b) $E = 10^{19}$ eV (c) $E = 10^{20}$ eV

(d) $\vartheta_{axis} = 0$ deg (e) $\vartheta_{axis} = 45$ deg (f) $\vartheta_{axis} = 60$ deg

Figure 5.11: Reduced χ^2 as a function of φ_{axis}. Different colors indicate different centroid uncertainty algorithm. The red cycles indicate the old parametrization, the green cycles and blue cycles ATT1 and ATT2, respectively. The regions for coming in and going away shower are indicated as well.

(b) and (c) indicate that the reduced χ^2 increases for high energy going away[5] showers. This is supported by (e) and (f) where one has stronger differences for inclined shower geometries.

One can conclude that the pulse centroid uncertainty is mostly underestimated for high energy distant going away showers [89]. The proposed uncertainty algorithms are affected as well but not as strong as the current one. It seems that this effect also has some impact on the energy reconstruction as shown in Fig. 5.13. The fractional energy error as a function of R_p is plotted once for coming in and once for going away showers. Coming in showers have a much more constant offset independent of R_p and all uncertainty algorithms produce the same result. In general, the reconstructed energy is systematically lower for small R_p. This could have several reasons [90]:

[5]The ratio between coming in and going away shower is roughly 3:2 in this data set

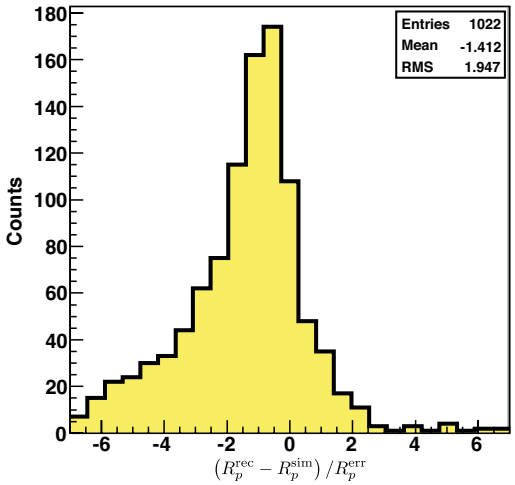

(a) Histogram of the fractional error in R_p.

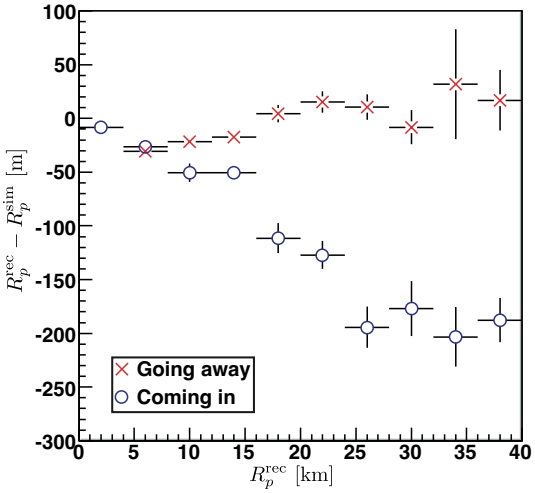

(b) Differences between R_p^{rec} and R_p^{sim} as a function of R_p^{rec}.

Figure 5.12: Comparison of reconstructed "rec" and simulated "sim" R_p. The simulated R_p seems to be shifted towards the telescope.

- The reconstructed geometry could be systematically off for nearby showers, but differences in R_p for MC and real shower do not verify this (cf. Fig. 5.12).
- There could be a problem with light collection or shower profile reconstruction since nearby showers produce a fatter track in the camera than far away showers. Maybe

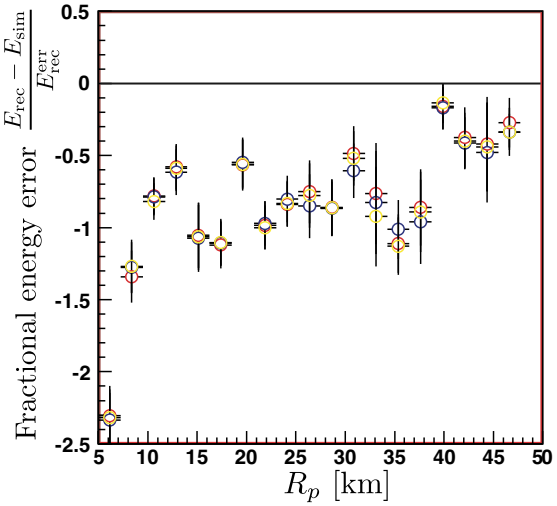

(a) Coming in events

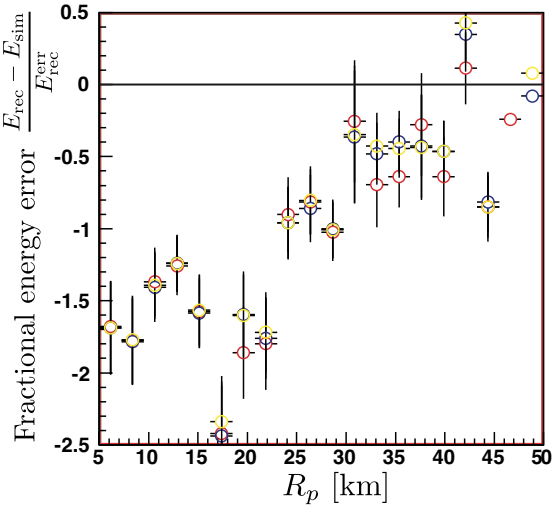

(b) Going away events

Figure 5.13: Fractional error as a function of R_p for coming in (a) and going away (b) events.

one needs to set different ζ values[6] according to different ranges.

- There could be a timing problem that grows with the distance to the shower. This could be related to asymmetries in the pulse shape. If the reconstructed pulse centroid was shifted from the true one by a fraction of the pulse width one would expect this effect [91].

To see the impact on real data, approximately 10000 golden hybrid events with standard quality cuts were used. The energy dependence is shown in Fig. 5.14. One can see that all algorithms indicate an increasing χ^2/N_{df} towards larger energies, which is relatively strong for the raw and ATT2 algorithm.
The impact on R_p is separated into going away and coming in showers and is shown in Fig. 5.15. The previous simulation result seems to be confirmed and going away showers are more affected than coming in events.

5.5 Conclusion

In the previous sections some approaches were made to parameterize the centroid pulse time uncertainty in a more physical and stable way than it is done right now. It could be shown that it is possible to use MC data in conjunction with real data to parameterize the estimated pulse centroid uncertainty as a function of the integrated charge and duration of the pulse. More refined studies are needed to further improve the estimate of the correct centroid uncertainty and other effects may also affect the estimation e.g. the camera shadow of the telescope [92].

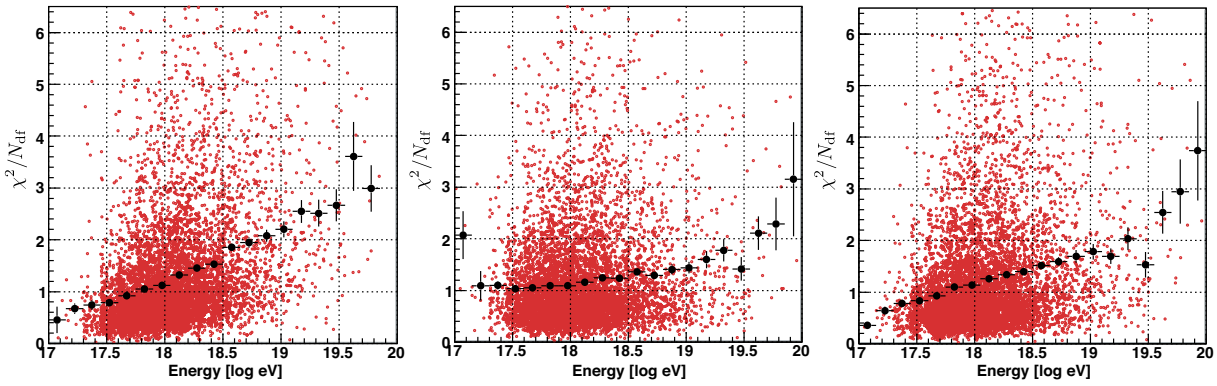

(a) Raw algorithm (b) ATT1 algorithm (c) ATT2 algorithm

Figure 5.14: Energy dependence of χ^2/N_{df} for golden hybrid events. Red dots indicate the scatter plot and black dots the corresponding profile plot.

[6]The ζ angle corresponds to the angular distance around a given point of the track at the camera. It is used to obtain the signal from nearby pixel.

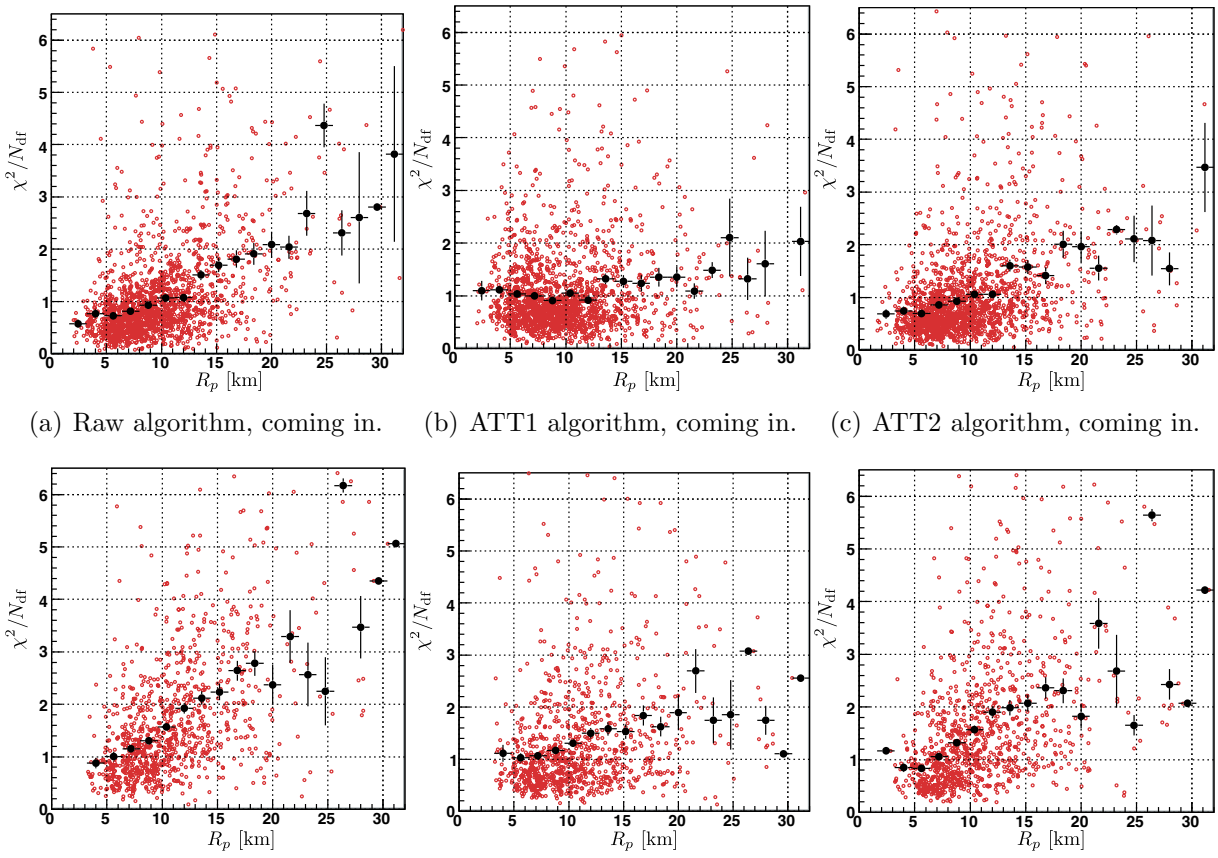

(a) Raw algorithm, coming in. (b) ATT1 algorithm, coming in. (c) ATT2 algorithm, coming in.

(d) Raw algorithm, going away. (e) ATT1 algorithm, going away. (f) ATT2 algorithm, going away.

Figure 5.15: Impact on golden hybrid events as a function of R_p separated in coming in and going away showers. Red dots indicate the scatter plot and black dots the corresponding profile plot.

Chapter 6

Fluorescence Reconstruction Revisited

Since the 60's, when the use of extensive air shower (EAS) fluorescence light was proposed for the detection of ultra high energy cosmic rays (UHECR's), many past, current and future experiments [48, 93, 77, 78] utilize the effect to get a clue about the origin of cosmic rays. In the fluorescence technique, the geometry of the shower is reconstructed based on the correlation between viewing angle and arrival time of the signals detected by the telescope. The signals are compared to those expected for different shower geometries and the best-fit geometry is determined. The calculation of the expected signals is based on a relatively simple function which is motivated by basic geometrical considerations. This function is based on certain assumptions on the processes of light emission and propagation through the atmosphere.

6.1 Motivation

The determination of the shower geometry from fluorescence observations has already been discussed in Section 4.5 and 4.6. First used at the Utah Fly's Eye detector [48] the expected arrival time t_i of fluorescence light can be expressed as (cf. Eqn. 4.5)

$$t_i = t_0 + \frac{R_p}{c} \tan\left(\frac{\chi_0 - \chi_i}{2}\right) \ . \tag{6.1}$$

The expected arrival time as a function of χ_i for different geometries is shown in Fig. 6.1. The amount of curvature is geometry dependent and sensitive to the fit parameters R_p, t_0 and χ_0 whose uncertainties propagate also into the primary energy.

However, in Eqn. 6.1 it is assumed that everything

1. propagates with the speed of light in vacuum,
2. takes place instantaneously and
3. propagates on straight lines.

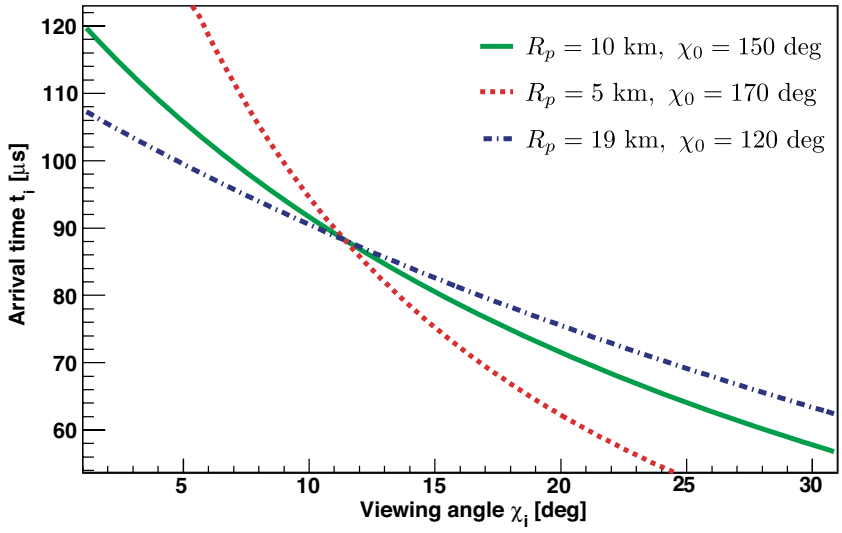

Figure 6.1: Example of different timing fits for some geometries according to Eqn. 6.1. The reference time t_0 is always set to zero. The amount of curvature is geometry dependent.

The validity of these assumptions are discussed in the following Sections. If required, corrections are provided.

6.2 Propagation speed of extensive air showers

In Eqn. 4.3 it is assumed, that the extensive air shower (EAS) propagates with the speed of light in vacuum c. A reduced shower speed would cause a discrepancy in arrival time at the telescopes.
To estimate the propagation speed of an EAS one has to apply relativistic kinematics. The kinetic energy E_{kin} of a particle with mass m_0 and propagation speed c is given by

$$E_{\text{kin}} = m_0c^2(\gamma - 1) = m_0c^2 \left(\frac{1}{\sqrt{1 - \frac{v^2}{c^2}}} - 1 \right) \quad . \tag{6.2}$$

Resolving Eqn. 6.2 to the propagation speed v yields

$$v = c\sqrt{1 - \frac{m_0^2c^4}{(E_{\text{kin}} + m_0c^2)^2}} \quad . \tag{6.3}$$

Fig. 6.2 illustrates the propagation speed as a function of kinetic energy E_{kin} for different particles. As expected, particles with large rest masses propagate slower in comparison to light particles with the same kinetic energy. Table 6.1 illustrates an energy threshold for different kinds of particles if we define a criterion for high energy particles to have a time offset $\Delta t = s/v - s/c < 1$ ns after traveling a distance s of 10 km (which

would be of negligible impact on the arrival time with the timing resolution of current giant air shower experiments) [94].

Electron:	E_{e^-}	$= 66$ MeV
Proton:	E_p	$= 121$ GeV
Iron:	E_{Fe}	$= 6.7$ TeV

Table 6.1: Energy threshold for different particles to be characterized as "propagating with vacuum speed of light".

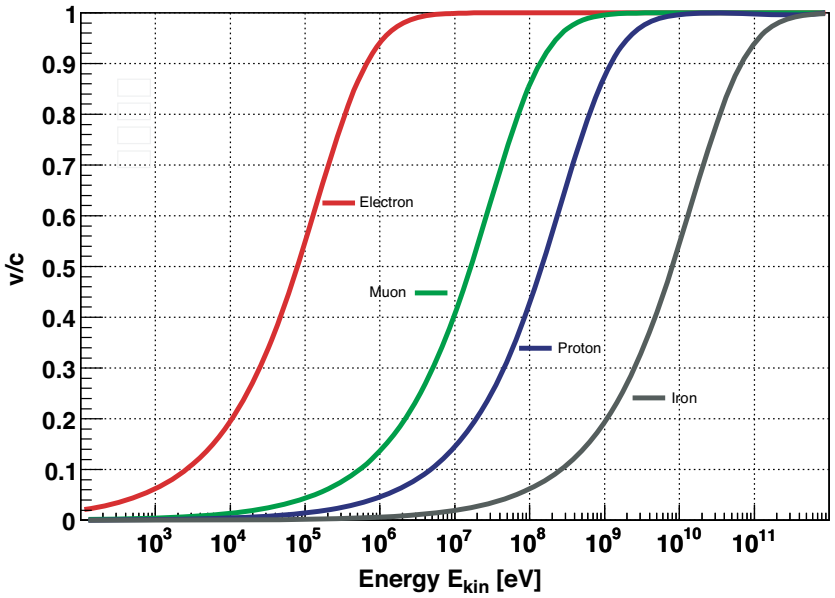

Figure 6.2: Propagation speed of different particles as a function of kinetic energy.

Assuming a primary proton with an energy $E_{prim} = 10$ EeV one may consider the speed of the leading particle as the propagation speed of the shower front. Assuming further, that after one interaction length the energy of the primary particle is roughly halved, the energy of the leading particle at shower maximum (i.e. after ~ 10 interaction lengths) is still $E_{lead} \approx E_{prim} \cdot 2^{-10} \approx 10$ PeV. Thus, in comparison to $E_p = 121$ GeV the shower front can be approximated to propagate with the speed of light c. This also holds when assuming a primary iron nuclei ($A = 56$).

6.3 Time delay due to low energy electrons

In Section 6.2 the propagation speed of an EAS was calculated assuming that the shower front propagates with the speed of the leading particle. However, the energy release and the resulting emission of fluorescence light mainly arises from secondary (lower energy)

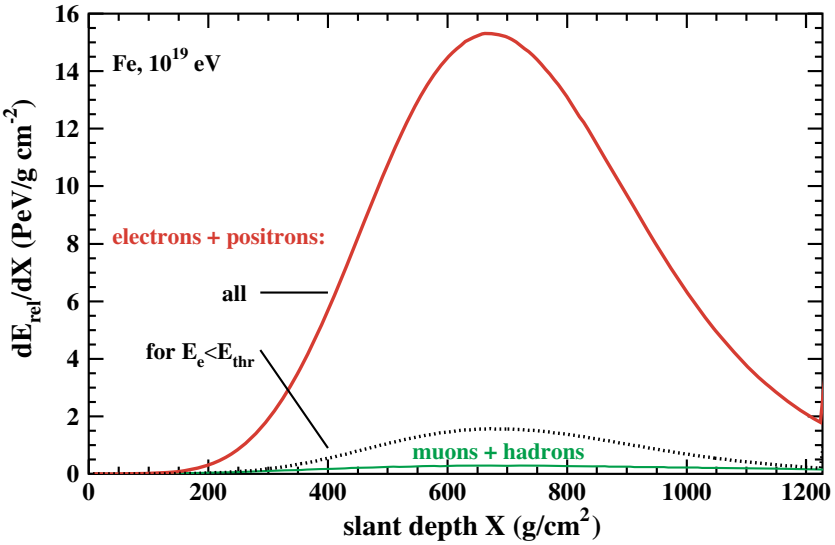

Figure 6.3: Energy release of different particles within the longitudinal shower development for a primary 10^{19} eV iron particle simulated with CORSIKA. The energy threshold of $E_{\text{thr}} = 0.1$ MeV is indicated (cf. [95]).

particles [95] which may release larger quantities of fluorescence light behind the shower front. In Fig. 6.3 different contributions to the energy release are shown, as derived from CORSIKA simulations. As expected, the main contribution stems from positrons and electrons, the most numerous charged particles in EAS. There are also some contributions of electromagnetic particles below the simulation energy threshold of $E_{\text{thr}} = 0.1$ MeV with a fraction of about 10%. Around the shower maximum, the energy release contribution of muons and hadrons are less than 2-3%. Thus, electrons and positrons can be regarded as the main target for further energy release studies.
Low energy electrons are mainly produced by high energy electrons via Møller scattering while low energy electrons can also gain energy from low-energy photons by Compton scattering. An important quantity are the energies of electrons and positrons contributing to the energy release in EAS. In Fig. 6.4 the contribution to the energy release per matter traversed in shower direction as a function of kinetic particle energy is shown. At those energies secondary particles of extensive air showers lose their energy mostly by ionization and excitation of air molecules. The main contribution arises from electrons and positrons with energies between 100 keV and 1 GeV with a tail towards small energies (cf. Fig. 6.4). Almost all of the air fluorescence in the wavelength range between 300 nm and 400 nm originates from transitions of molecular nitrogen N_2 or molecular nitrogen ions N_2^+ which make ∼78% of the air composition. A more detailed study concerning excitation and de-excitation processes can be found in Section 6.4. A broad maximum is visible at particle energies around 10-50 MeV and ∼ 22% of the energy loss is caused by electrons with kinetic energies < 1 MeV. The ionization energy loss is described by the Bethe-Bloch stopping power formula [96]

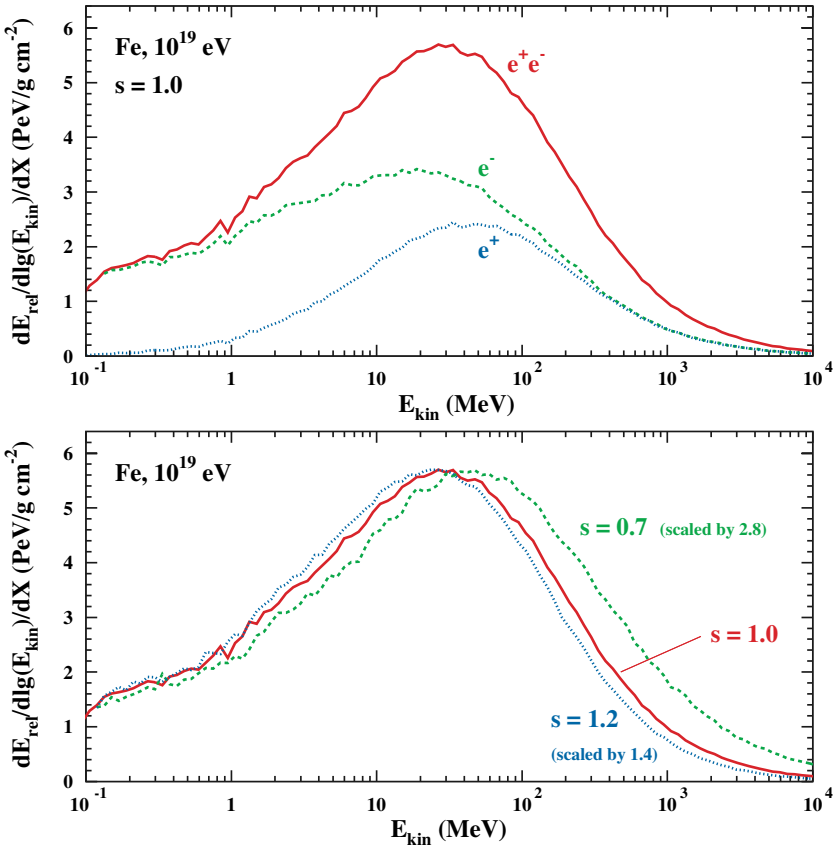

Figure 6.4: (Upper panel): Contribution of electrons and positrons to the energy release for a primary iron with 10^{19} eV at shower maximum. **(Lower panel)**: Combined contribution of electrons and positrons to the energy release for a primary iron with 10^{19} eV for different shower ages s normalized to the same height of maximum (cf. [95]).

$$\frac{dE_i}{d\lambda} = \frac{\gamma^2 z^2}{\gamma^2 - 1}\kappa_1 \left(\ln(\gamma^2 - 1) - \beta^2 + \kappa_2\right) \ , \tag{6.4}$$

where $\beta = v/c$ is the velocity of the particle in the laboratory frame in units of the velocity of light, $\gamma = 1/\sqrt{1-\beta^2}$ is the Lorentz factor, $d\lambda$ the thickness of traversed matter and z the charge of the ionizing particle in units of e. The two constants $\kappa_1 = 0.153287$ MeV g^{-1} cm^2 and $\kappa_2 = 9.386417$ refer to dry air [96]. Above a critical energy $E_c \approx 580$ MeV$/Z$ (Z is the atomic number of the medium) energy loss induced by bremsstrahlung starts to dominate. Since more than 90% of the energy deposited in the atmosphere arises from $e^{\pm}$ with energies below E_c, only ionization energy loss is comprised in further studies.

As can be seen in Fig. 6.2 electrons with energies < 10 MeV have a significantly lower propagation speed than the shower front. As a result the energy release into air (excitation region) occurs behind the shower front as illustrated in Fig. 6.5. In order to estimate the offset, one can assume low energy electrons with different energies starting simultaneously

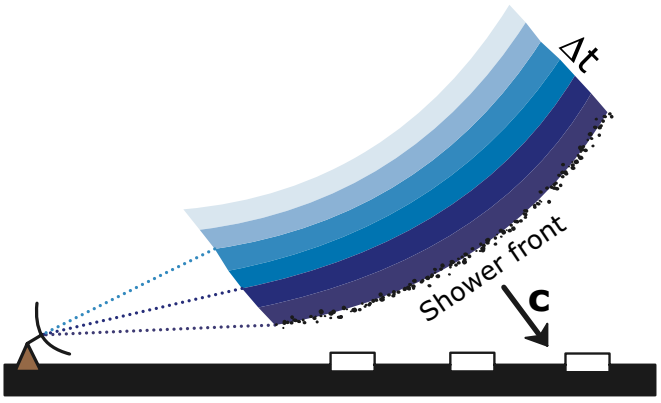

Figure 6.5: Illustration of the delay of fluorescence light due to low energy electrons and positrons. As a result of the reduced propagation speed electrons and positrons excite nitrogen molecules slightly behind the shower front resulting in an offset Δt in time.

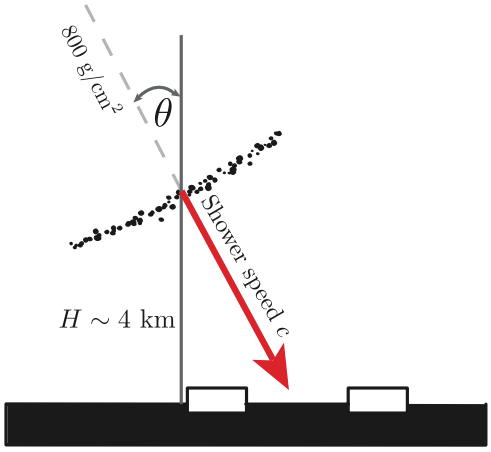

Figure 6.6: Illustration of the shower geometry during the simulation. Starting at a height of $H \sim 4$ km the shower propagates at an angle of $\theta = 38$ deg to the Earth surface.

with the shower front (speed c) into the same direction. Due to the reduced speed, the electron is limping behind the shower front and an offset Δt in time occurs. According to Eqn. 6.4 the electron is losing energy until the energy is too low for further ionization. This is shown in Fig. 6.7. The time offset is plotted as a function of the integrated relative energy loss for different starting energies. During the simulation is was assumed that the shower starts at a slant depth of $X_{\text{start}} = 800$ g/cm^2, the averaged X_{max} for EAS, and with an inclination angle θ of 38 deg as illustrated in Fig. 6.6. At that point electrons of different energies are injected simultaneously with the shower front and the time offset is calculated until the electrons have released all their energy in the atmosphere. Electrons with large kinetic energies lose almost all their energy close to the shower front. With decreasing energy the time delay is increasing up to an energy of $\sim$ 1 MeV. For even smaller energies Δt is decreasing again due to the rise in the Bethe-Bloch formula at low energies. Such low energy particles move, on the one hand, relatively slow. On the other hand, they release their energy quickly so that the time offset remains small. Most fluorescence light is excited with a delay of $\sim$ 2 ns with respect to the shower front. In first approximation this effect is negligible in hybrid reconstruction.
This simple estimate neglects 3D-effects by multiple scattering and particle cascading (δ-electrons). In case of δ-electron production one can imagine the time delays of electrons of different energies to sum up, resulting in a delay of several ns. More refined CORSIKA studies are planned to study such effects.

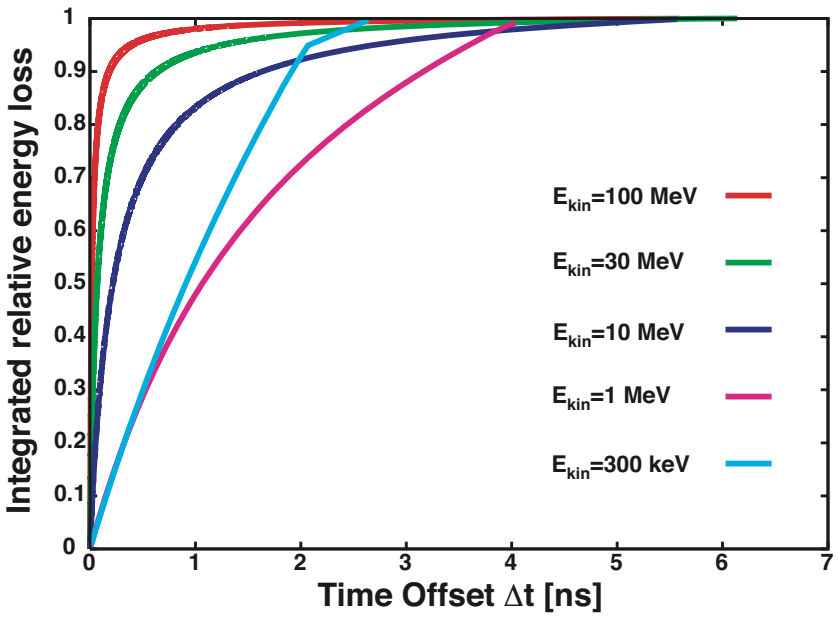

Figure 6.7: Time delay Δt of low energy electrons behind the shower front. Most of the energy is released close to the shower front. The lowest ascent is visible for a 1 MeV electron where the Bethe-Bloch formula has its minimum.

6.4 Modeling nitrogen fluorescence in air

In this Section the assumption of instantaneous fluorescence light production is checked. To determine the expected arrival time of fluorescence light at the telescope, a good knowledge of excitation and de-excitation processes is essential. The situation is sketched in Fig. 6.8. The nitrogen fluorescence spectrum mainly consists of transitions from the second positive system (2P) of molecular nitrogen N_2 and the first negative system (1N) of ionized nitrogen molecules N_2^+:

$$2P(\nu', \nu'') \quad : \quad C^3\Pi_u(\nu') \rightarrow B^3\Pi_g(\nu'') \tag{6.5}$$

$$1N(\nu', \nu'') \quad : \quad B^2\Sigma_u^+(\nu') \rightarrow X^2\Sigma_g^+(\nu'') \ . \tag{6.6}$$

Here the notation "second positive" and "first negative" refers to the place of emission of the appropriate band system in gas discharge tubes. About 88% of the total emission is found in the range of 300-400 nm [97]. There are various processes by which the two systems can get excited. However, characteristic time constants for excitation are around 10^{-6} ns [98] and are negligible for this study.

6.4.1 De-excitation

After a typical decay time $\tau_{\nu',\nu''}$ the excited initial electronic-vibrational state ν' will relax into any lower energetic state ν''. Let $N^*_{\nu'}$ be the number of excited molecules in the state

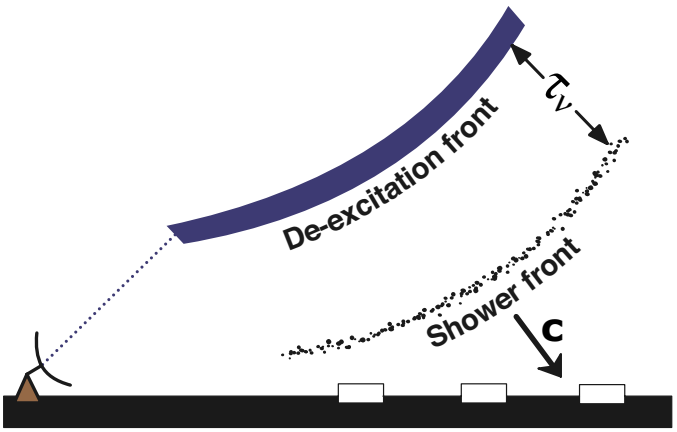

Figure 6.8: Illustration of the time delay due to excitation and de-excitation processes. Assuming that the excitation process takes place inside the shower front, fluorescence light emission is delayed by τ_ν.

ν'. Then there is[1]

$$\frac{dN^*_{\nu'}}{dt} = -\frac{1}{\tau_{\nu',\nu''}} N^*_{\nu'}(t) \ . \tag{6.7}$$

The reciprocal decay time $\tau^{-1}_{\nu',\nu''}$ corresponds to the Einstein coefficient $A_{\nu',\nu''}$ of the transition $\nu' \rightarrow \nu''$. If there is more than one final state ν'', the total rate becomes

$$\begin{aligned} \frac{dN^*_{\nu'}}{dt} &= -\sum_{\nu''} \frac{1}{\tau_{\nu',\nu''}} N^*_{\nu'}(t) \\ &= -\sum_{\nu''} A_{\nu',\nu''} N^*_{\nu'}(t) = -\frac{1}{\tau_{\nu'}} N^*_{\nu'}(t) \ . \end{aligned} \tag{6.8}$$

Therefore, the mean lifetime $\tau_{\nu'}$ of the excited state ν' results to be the inverse sum over all transition probabilities $A_{\nu',\nu''}$ and the effective observable lifetime of any transition $\nu' \rightarrow \nu''$ turns out to be equal to $\tau_{\nu'}$.

6.4.2 Quenching

In reality not all transitions are necessarily radiative transitions. It is also possible that they transfer energy into rotations, vibrations or translations of other molecules without emitting optical photons. This is the quenching effect and as a consequence one has to introduce an additional radiationless deactivation term into Eqn. 6.8:

$$\frac{1}{\tau_{\nu'}(p,T)} = \frac{1}{\tau_{0_{\nu'}}} + \frac{1}{\tau_{c_{\nu'}}(p,T)} \ , \tag{6.9}$$

[1] if cascading from higher energetic states is neglected or is considered to have much smaller time constants than the mean lifetime of this state

where $1/\tau_{0_{\nu'}}$ is the sum over all constant transition probabilities and $1/\tau_{c_{\nu'}}(p,T)$ is the total collisional deactivation rate which depends on the pressure p and temperature T of the gas. Following [98] the final expression for the total quenching rate becomes

$$\frac{1}{\tau_c} = \frac{p}{kT}\sqrt{\frac{T}{293\ \mathrm{K}}}\sum_i f_i Q_i \quad \propto \frac{p}{\sqrt{T}}\ , \tag{6.10}$$

where k is the Boltzmann constant, f_i denotes the fraction of molecules or atoms of the corresponding gas constituent i, Q_i is the corresponding quenching rate constant referring to a temperature of 293 K. The final reciprocal lifetime can then be expressed as

$$\frac{1}{\tau_{\nu'}(p,T)} = \frac{1}{\tau_{0_{\nu'}}}\left(1 + \underbrace{\frac{\tau_{0_{\nu'}}}{kT}\sqrt{\frac{T}{293\ \mathrm{K}}}\left[f_{N_2}\cdot Q^{\nu'}_{\mathrm{N}_2} + f_{\mathrm{O}_2}\cdot Q^{\nu'}_{\mathrm{O}_2} + f_{\mathrm{Ar}}\cdot Q^{\nu'}_{\mathrm{Ar}}\right]}_{1/p'_{\nu'}}\cdot p\right)\ , \tag{6.11}$$

where $p'_{\nu'}$ is the reference pressure at which the radiative transition rate $1/\tau_{0_{\nu'}}$ is equal to the collisional deactivation rate $1/\tau_{c_{\nu'}}$. One can then simplify Eqn. 6.11 to

$$\frac{1}{\tau_{\nu'}(p,T)} = \frac{1}{\tau_{0_{\nu'}}}\left(1 + \frac{p}{p'_{\nu'}(T)}\right)\ . \tag{6.12}$$

6.4.3 Estimation of de-excitation times as a function of height

In this study dry air with the following composition is assumed:

f_{N_2}	f_{O_2}	f_{Ar}
0.781	0.209	0.01

Fig. 6.9 shows the nitrogen fluorescence spectrum. The main contributions arise from the second positive and the first negative system $2P(0,\nu'')$, $1P(1,\nu'')$ and $1N(0,\nu'')$. The aim is to find an appropriate lifetime $\tau_{\nu'}$ as a function of pressure and temperature of these three sub-spectra. Weaker contributions are neglected. From Eqn. 6.12 one has

$$\frac{1}{\tau_{\nu'}(p,T)} = \frac{1}{\tau_{0_{\nu'}}}\left(1 + p\cdot\sqrt{\frac{293\ \mathrm{K}}{T}}\frac{1}{p'_{\nu'}(293\ \mathrm{K})}\right). \tag{6.13}$$

Fig. 6.10 shows temperature profiles of the atmosphere above Malargüe [99] together with the profile used in this analysis. The connection between pressure p and height h is calculated via the barometric formula

$$p = p_0 e^{-h/H}$$

using a scale height $H = 8005$ m and a reference pressure $p_0 = 1013$ hPa. The variation of the relative intensities of the main transitions for different pressures is smaller than

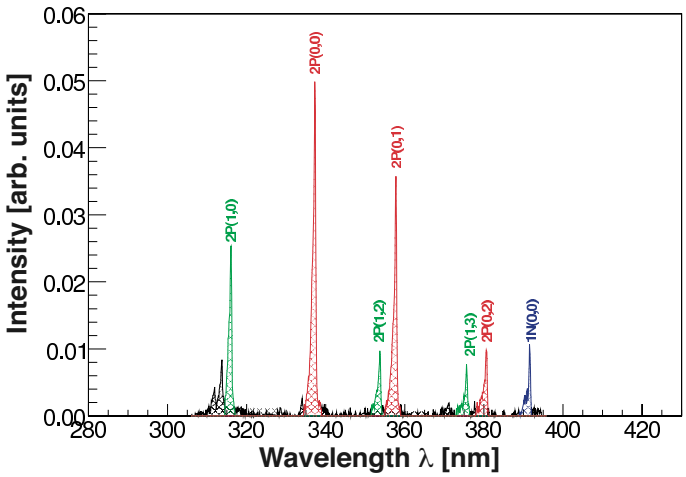

Figure 6.9: Most intensive transitions in the nitrogen spectrum emerge from three electronic vibrational states marked by different colors (from [98]).

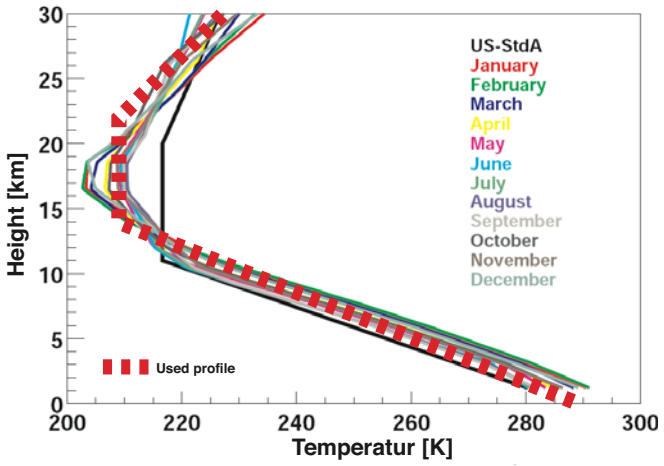

Figure 6.10: Temperature profile of the Malargüe monthly models [99] together with the profile used in this analysis (dashed line).

	$2P(0,\nu'')$	$2P(1,\nu'')$	$1N(0,\nu'')$
Fraction [%]	61	31	8
$\tau_{0_{\nu'}}$ [ns]	38.93	32.88	65.22
$p'_{\nu'}$ [hPa]	15.30	15.45	1.20

Table 6.2: Parameters used in this analysis (cf. [98]). The values for $p'_{\nu'}$ refer to a temperature of 293 K.

5% up to a height of 24 km ($\sim$ 50 hPa) for dry air (cf. Fig. 6.11) and it is neglected henceforth. From Fig. 6.11 one can also estimate the intensities of the main transitions

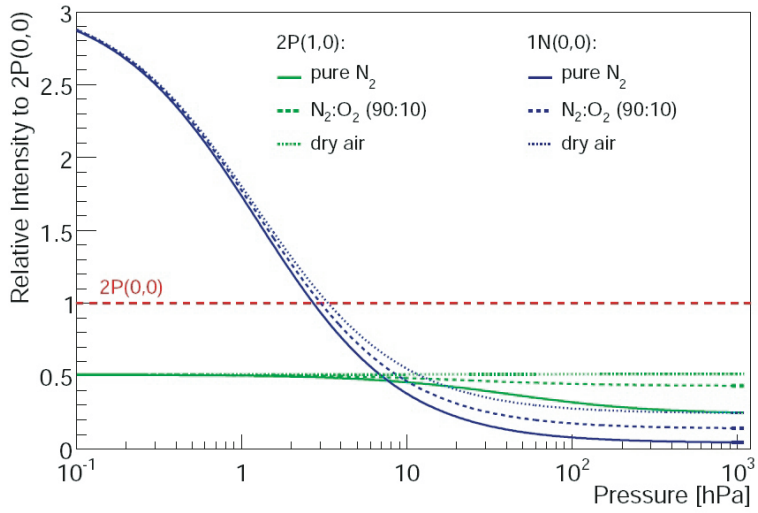

Figure 6.11: Pressure dependence of the relative intensities with respect to $2P(0,0)$ [98]. 20 km corresponds to $\sim$ 80 hPa.

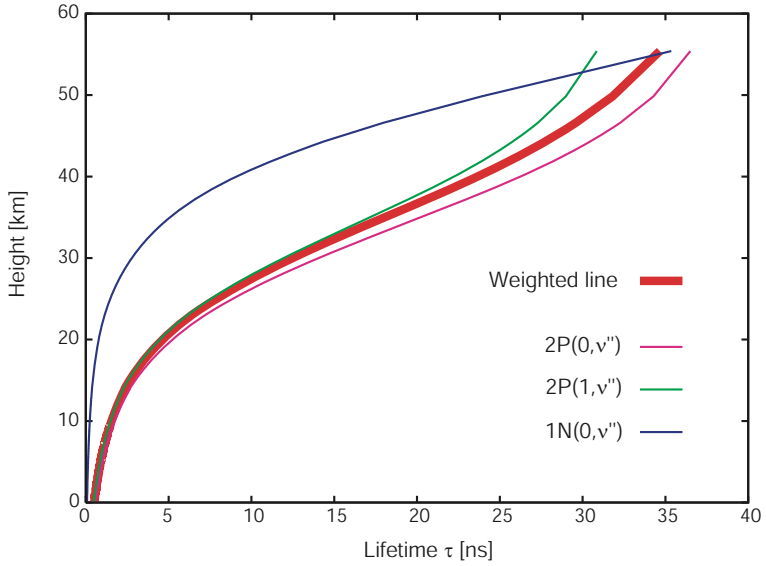

Figure 6.12: Lifetime of individual transitions as a function of height a.s.l. for dry air. The thick line indicates the weighted lifetime according to the different intensity fractions given in Table 6.2. The width of that line roughly denotes a temperature uncertainty of $\pm$40 K.

as listed in Table 6.2.

Fig. 6.12 illustrates the expected lifetime as a function of height above sea level calculated with the parameters of Table 6.2. The three main transitions are shown as well as the averaged lifetime weighted according to the different intensities. The width of weighted line roughly denotes a temperature uncertainty of $\pm$40 K. One can see that the

quenching term dominates at low altitudes and that the lifetime is below 5 ns up to a height of 20 km. This seems to be small, though within the minimization process altitudes above 20 km are not unusual. For $h \to \infty$ we have $\tau_{\nu'} \to \tau_{0_{\nu'}}$. It should be noted that the delay times get smaller with growing shower age. Anecdotally, this means the fluorescence light front appears to move with velocities larger than the vacuum speed of light.
The expected lifetime τ in ns as a function of height a.s.l. in m (weighted line in Fig. 6.12) can be parameterized in good approximation to be

$$\tau(h) = \frac{\tau_{0_{\nu'}}}{\alpha \cdot e^{-h/H} + 1} \ , \tag{6.14}$$

with $\tau_{0_{\nu'}} = 37.5$ ns, $H = 8005$ m and $\alpha = 95$. The expected arrival time (Eqn. 6.1) changes then to

$$t_i = t_0 + \frac{R_p}{c} \tan\left(\frac{\chi_0 - \chi_i}{2}\right) + \tau(h) \ . \tag{6.15}$$

6.4.4 Impact on Auger golden hybrid events

To study the impact on real data approximately 10000 *IoAuger* Golden Hybrid events were extracted using the quality cuts as shown in Table B.1 (App. B.2). Some explanations to these cuts are given in App. B.1. The showers have been reconstructed with *OFFLINE v2.0-drevil*. The impact on the fit parameters R_p, χ_0 and t_0 vs. the distance to shower maximum $R_{X_{\max}}$ is shown in Fig. 6.13. "Delta" refers to the difference between old and new reconstruction, where the new reconstruction takes the delayed light emission into account according to the thick line of Fig. 6.12. With increasing distance, the fit parameters are more affected because fluorescence light of larger altitudes is detectable. For low minimum viewing angles (MVA), i.e. coming in showers, larger differences occur (cf. Fig. 6.14).

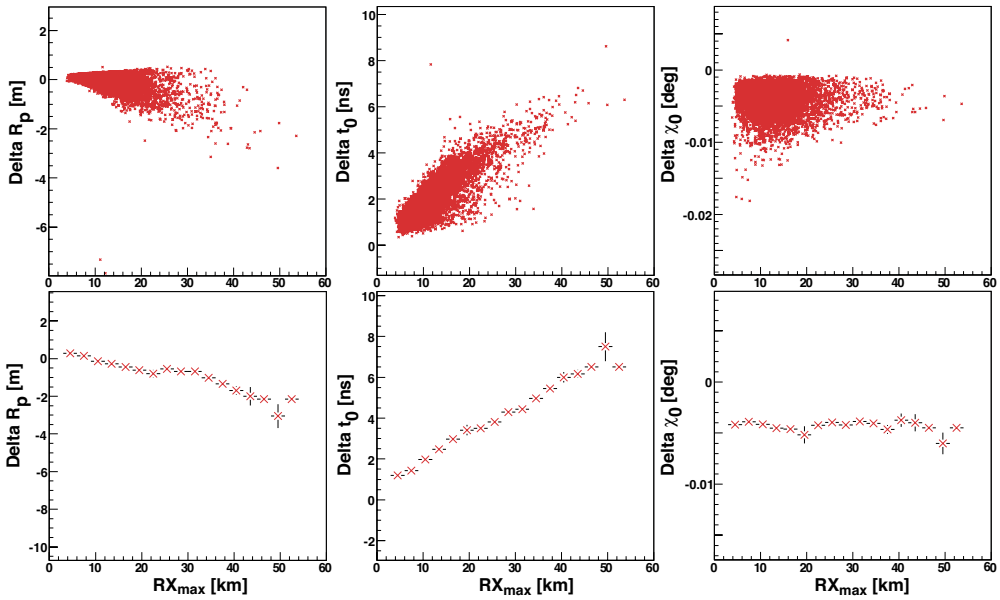

Figure 6.13: Differences in the fit parameters as a function of $R_{X_{\max}}$. "Delta" refers to the old value minus the new value (here: accounting for the de-excitation times). **(Upper panel)**: Profile plot. **(Lower panel)**: Corresponding scatter plot.

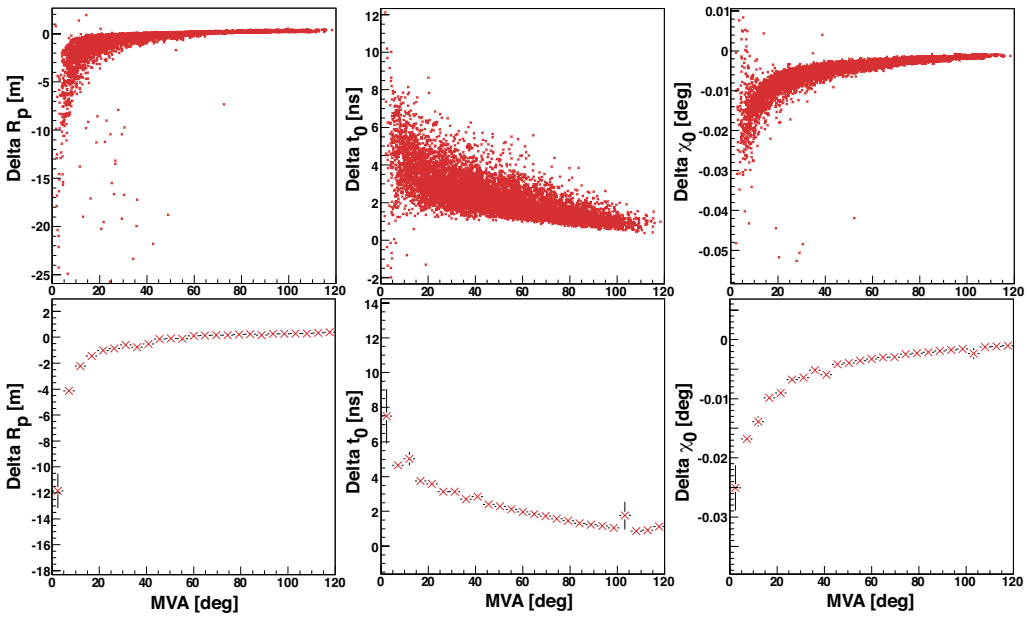

Figure 6.14: Differences in the fit parameters as a function of minimum viewing angle (MVA). "Delta" refers to the old value minus the new value (here: accounting for the de-excitation times). **(Upper panel)**: Profile plot. **(Lower panel)**: Corresponding scatter plot.

6.5 Reduced speed of fluorescence light

Going back to Eqn. 4.4 it is assumed, that fluorescence light propagates with the speed of light in vacuum c. A reduced propagation speed would cause a delay in arrival time at the telescope [100].

6.5.1 Basics about the index of refraction

The ratio of the speed of an electromagnetic wave in vacuum c to that in matter v is known as the absolute index of refraction n and is given by

$$n \equiv \frac{c}{v} \ . \tag{6.16}$$

Assuming that the atmosphere consists of m different layers each with a different index of refraction n_i, as shown in Fig. 6.15, the transit time from S to P is then

$$t = \frac{S_1}{v_1} + \frac{S_2}{v_2} + \ldots + \frac{S_m}{v_m} = \sum_{i=1}^{m} \frac{S_i}{v_i} = \frac{1}{c} \sum_{i=1}^{m} n_i S_i \ , \tag{6.17}$$

where S_i and v_i refer to the path length and the speed of light in layer i, respectively. The sum in Eqn. 6.17 is known as the *optical path length* (OPL) traversed by the ray, in contrast to the spatial path length $\sum_{i=1}^{m} S_i$. Clearly in case of an continuos inhomogenous medium, like the atmosphere, the summation leads to an integral:

$$\mathrm{OPL} = \int_S^P n(s)\ ds \tag{6.18}$$

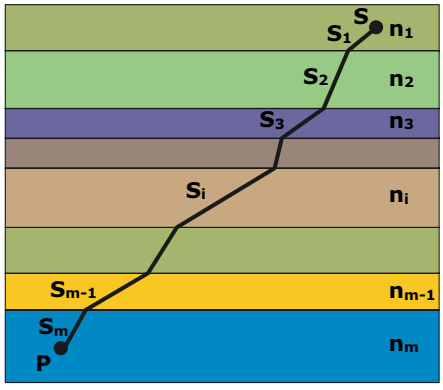

Figure 6.15: Illustration of a changing index of refraction. A light ray propagating through media with different index of refraction n_i from point S to P. The total propagation time is the sum over the individual times.

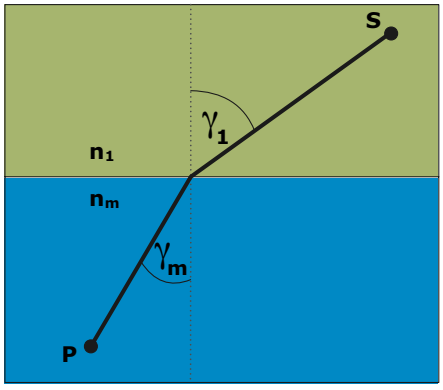

Figure 6.16: Fermat's principle applied to refraction. The angular difference is $\gamma_1 - \gamma_m > 0$ for a transition between two media with index of refraction n_1 and n_m, where $n_1 < n_m$, respectively.

With $t = \mathrm{OPL}/c$ one can state Fermat's principle:

"*Light, in going from points S to P, traverses the route having the smallest optical path length.*"

Fig. 6.16 illustrates Snell's law. It states that the ratio of the sines of the angles γ_1 and γ_m is equal to the inverse ratio of the indices of refraction:

$$n_1 \sin \gamma_1 = n_m \sin \gamma_m \ . \tag{6.19}$$

Basically, the index of refraction is a function of the traversed medium and wavelength λ. In case of the atmosphere the dependence of the refractive index on pressure and temperature is often approximated as a dependence on density[2] and, thus, on altitude. Fig. 6.17 demonstrates the impact of different wavelength on the index of refraction. The calculation has been done in [101]. The change of $n(\lambda)$ is $< 3\%$ for the wavelength range covered by the FD (cf. Fig. 6.17). As in CORSIKA, the wavelength dependence is ignored in the following and a value for a fixed wavelength is adopted.

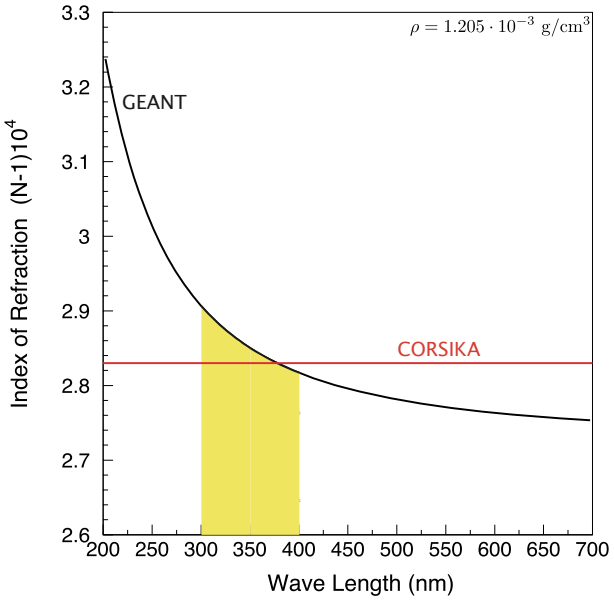

Figure 6.17: Index of refraction as a function of wavelength for fixed atmospheric conditions at sea level. The yellow area represents the 300-400 nm wavelength band of fluorescence light (cf. [101]).

6.5.2 Implementing a realistic atmosphere in hybrid reconstruction

This Section explains how Eqn. 4.4 is calculated taking into account an index of refraction $n > 1$ and illustrates the implementation into the hybrid reconstruction chain.

[2]The effect of varying humidity or other ingredients of air is neglected.

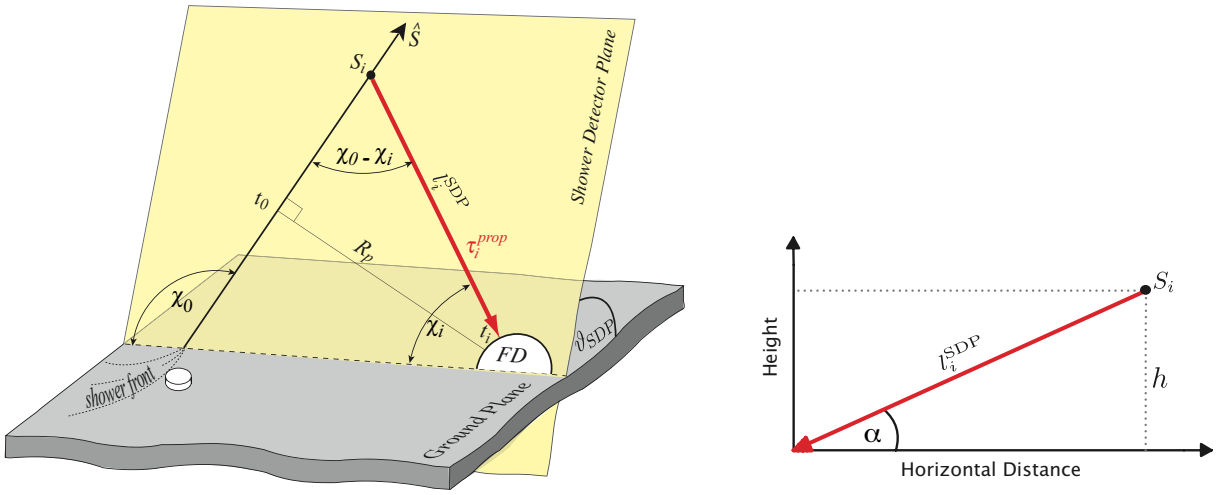

(a) Illustration of the propagation time τ_i^{prop} and distance l_i^{SDP} between point S_i and the telescope.

(b) Parameters used within the calculation.

Figure 6.18: Illustration of the geometry for the reduced speed of light.

During the reconstruction one needs to know the index of refraction of the atmosphere along a particular path. To locate the point where the fluorescence light is emitted the height and the angle α, as shown in Fig. 6.18, is needed.

One obtains

$$\alpha = \arcsin\left(\frac{h}{l_i^{\text{SDP}}}\right) \ , \tag{6.20}$$

with $l_i^{\text{SDP}} = R_p / \sin(\chi_0 - \chi_i)$ and $h = l_i^{\text{SDP}} \cdot \sin\vartheta_{\text{SDP}} \cdot \sin\chi_i$ (see Fig. 6.18 for definition of ϑ_{SDP}). The light now propagates through the atmosphere with the speed being determined by the local index of refraction. To parameterize the index of refraction as a function of height one can follow the approach of CORSIKA [96, 102] simulations. In general, the index of refraction depends on the altitude h due to its dependence on the atmospheric density. A reasonable approximation is given in [103] by assuming a scaling law with the atmospheric density $\rho(h)$:

$$\frac{n(h) - 1}{n_0 - 1} = \frac{\rho(h)}{\rho_0} \ . \tag{6.21}$$

The values $\rho(h)$ and $n(h)$ refer to the atmospheric density and the index of refraction at altitude h and n_0 and ρ_0 are the corresponding values at sea level. Eqn. 6.21 can be approximated [104] by the local density $\rho(h)$:

$$n(h) = 1 + 0.000283\frac{\rho(h)}{\rho_0} \tag{6.22}$$

The density variation of the atmosphere is modeled by 4 layers with an exponential dependence on the altitude (cf. Fig. 6.19)

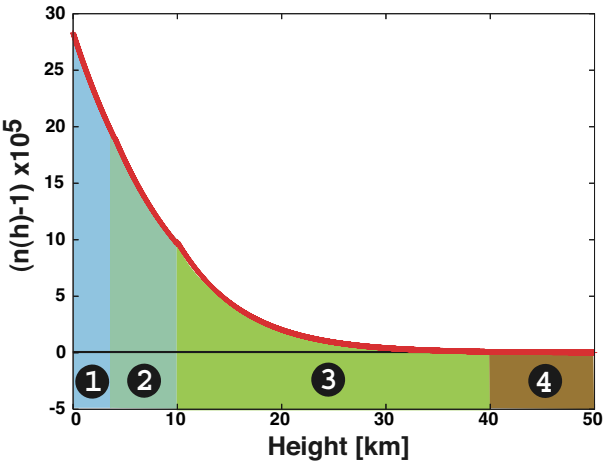

Figure 6.19: Index of refraction as a function of height a.s.l.. Four different layers are indicated. Parameters from the U.S. standard atmosphere are used.

$$\rho(h) = \frac{b_j}{c_j} e^{-h/c_j} \ , \tag{6.23}$$

where h is the height a.s.l. and b_j as well as c_j atmospheric parameters for the U.S. standard atmosphere as shown in Table 6.3 (the linear term for altitudes > 100 km is neglected).

Layer j	**Altitude** h **[km]**	b_j [g/cm^2]	c_j [cm]
1	0 . . . 4	1222.6562	994186.38
2	4 . . . 10	1144.9069	878153.55
3	10 . . . 40	1305.5948	636143.04
4	40 . . . 100	540.1778	772170.16

Table 6.3: Parameters for the U.S. standard atmosphere.

Knowing the local density, the index of refraction $n(h)$ can be calculated as

$$n(h) = 1 + \frac{0.000283}{\rho_0} \frac{b_j}{c_j} e^{-h/c_j} \ , \tag{6.24}$$

with $\rho_0 = b_1/c_1$. For completeness it is assumed that the index of refraction is $n(h) = n(h_{\text{Tel}})$ for $h < h_{\text{Tel}}$ and $n(h) = 1$ for $h > 100$ km. h_{Tel} characterizes the individual height of the telescope above sea level. For each layer the propagation time from emission to detection at the receiving telescope can then be calculated via integration:

$$\begin{aligned}\tau_j &= \frac{1}{c\sin\alpha}\int_{h_{\rm Tel}}^{h} n(h')\,dh' \\ &= \frac{1}{c\sin\alpha}\left[h - h_{\rm Tel} - \frac{0.000283\cdot b_j}{\rho(0)}\left(e^{-h/c_j} - e^{-h_{Tel}/c_j}\right)\right] \ . \end{aligned} \tag{6.25}$$

For light paths traversing several layers j, the final propagation time $\tau_i^{\rm prop}$ is the sum over the individual layers

$$\tau_i^{\rm prop} = \sum_j \tau_j \ . \tag{6.26}$$

The calculation of $\tau_i^{\rm prop}$ is performed using a function in *HybridGeometryFinder.cc* where the old calculation is replaced. Due to different velocities of the shower front (vacuum speed c) and fluorescence light (effective speed of light c_i') the expected arrival time (Eqn. 6.15) changes to

$$t_i^{\rm exp} = t_0 + \underbrace{\frac{R_p}{c_i'}\left(\frac{1}{\sin(\chi_0-\chi_i)}\right)}_{\tau_i^{\rm prop}} - \frac{R_p}{c}\left(\frac{1}{\tan(\chi_0-\chi_i)}\right) + \tau_\nu(h) \ . \tag{6.27}$$

6.5.3 Estimation of the effect

To estimate the impact of a realistic atmosphere description the difference of the light arrival times between the cases of vacuum and realistic speed of light from different parts of the atmosphere, as shown in Fig. 6.20, is calculated. The time difference is larger for light propagating near the surface of the Earth as one would expect and differences of more than 20-25 ns can occur. Furthermore, coming in showers are expected to have a more constant offset contrary to going away showers.

As already mentioned in Section 6.5.1, light propagates along a particular path to the telescope which is not necessarily the shortest distance but, in general, a curved path. The impact on the arrival time difference between direct and curved path is shown in Fig. 6.21. The difference in arrival times between these cases is ≤ 0.03 ns. Thus, for calculating the arrival time, the approximation of the light path as straight line seems to be valid.

6.5.4 Application to simulated data

The shower sample consists of 1800 proton induced showers from the CORSIKA-Lyon database [86] with energies of 10^{18}, 10^{19} and 10^{20} eV and zenith angles of 0, 45 and 60 deg as already discussed in Section 5.4. These data were reconstructed with the old and new speed of light model. In addition to the quality cuts of Table B.1 only events of Eye 1

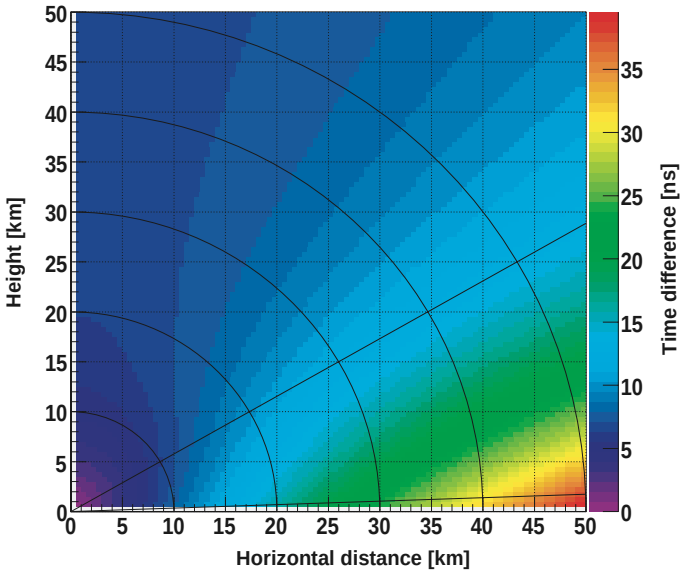

Figure 6.20: Arrival time difference $|t_{\text{real}} - t_{\text{vacuum}}|$ where just the effect of a reduced speed of light is included. The telescope is located at position [0,0] at 1416 m a.s.l. (corresponding to the altitude of the eye Los Leones). The straight lines indicate the field of view between 1 and 31 deg.

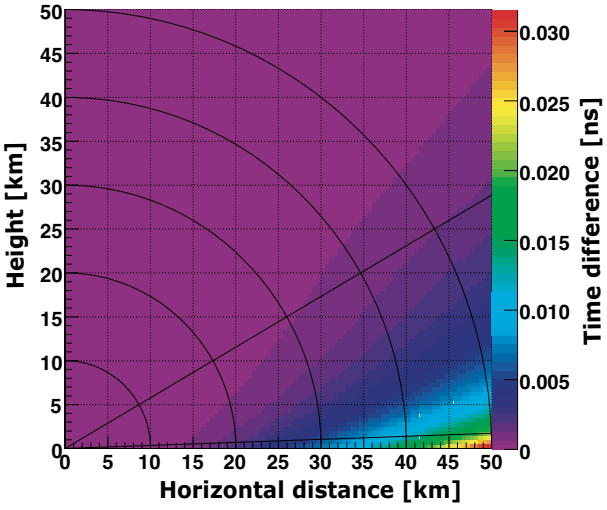

(a) Arrival time difference between direct and fastest path for a realistic atmosphere. The different colors indicate the difference $\tau_{\text{real}} - \tau_{\text{direct}}$ in ns.

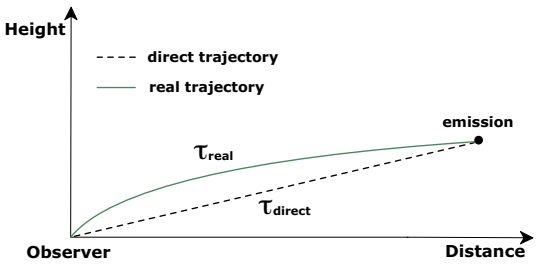

(b) Illustration of the arrival time difference. The green line is the real path of light whereas the black line is the direct connection between emission and observer.

Figure 6.21: Illustration of the arrival time difference between direct and fastest path for a realistic atmosphere.

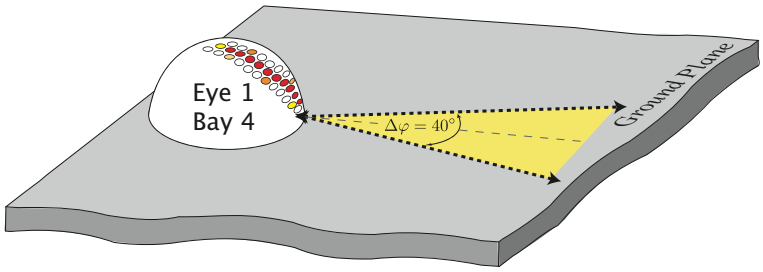

Figure 6.22: Going away and coming in showers are defined via φ_{axis} and have an opening angle of $\Delta\varphi = 40$ deg.

(Los Leones) were selected.
The effect on R_p, χ_0 and t_0 is shown in Fig. 6.23. Note that in the simulation chain the propagation speed of the fluorescence light is (until now) c and hence the reconstruction with (vacuum) c is consistent in contrast to real data. Going away and coming in showers are defined in Fig. 6.22. One can see that the effect is strong for coming in showers and large zenith angle and is negligible for going away showers. There is a complex effect on the fit parameters. The shape of the curves are a result of a three parameter fit within the χ^2-minimization.

To understand the complex dependencies with just one parameter one can plot the fit parameters as a function of the minimum viewing angle MVA as shown in Fig. 6.24. One can see that there is a strong dependence for low MVA (shower pointing towards the telescope). More information about the MVA can be found in App. B.1.

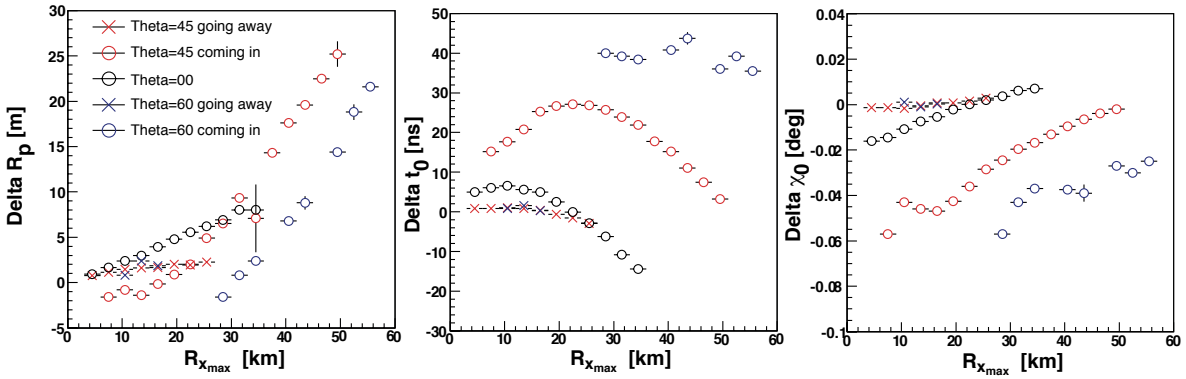

Figure 6.23: *Simulated Data*: Effect on R_p, χ_0 and t_0. Note that "vac" indicates the speed of light in vacuum and "real" the reduced speed of light. "Delta" refers to $x_{\text{vac}} - x_{\text{real}}$. Circles denote coming in and crosses going away showers. Different inclination angles ϑ are color coded (black $\rightarrow \vartheta = 0$ deg, red $\rightarrow \vartheta = 45$ deg and blue $\rightarrow \vartheta = 60$ deg).

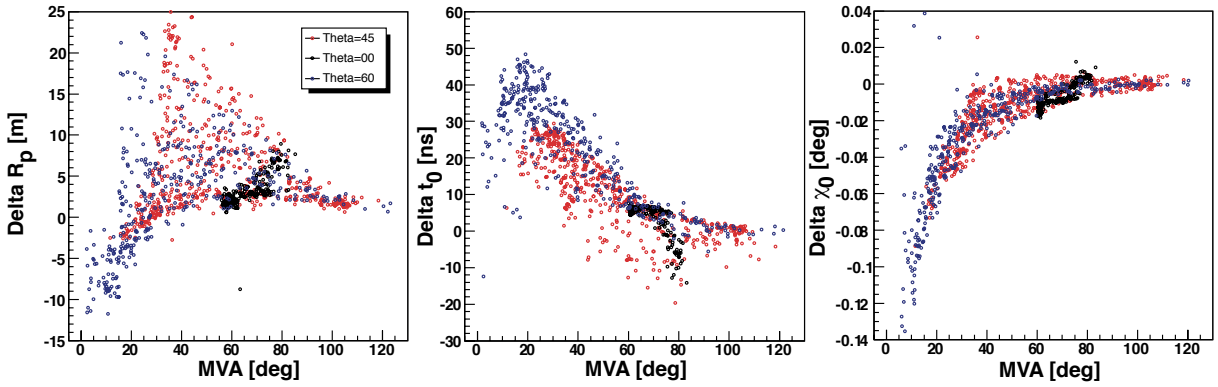

Figure 6.24: *Simulated Data*: Fit parameters as a function of minimum viewing angle. Note that "vac" indicates the speed of light in vacuum and "real" the reduced speed of light. "Delta" refers to $x_{\text{vac}} - x_{\text{real}}$. Different inclination angles ϑ are color coded (black $\rightarrow \vartheta = 0$ deg, red $\rightarrow \vartheta = 45$ deg and blue $\rightarrow \vartheta = 60$ deg).

6.5.5 Application to real data

To see the impact on real data the golden hybrid data set of Section 6.4.4 is used applying the same quality cuts as for simulated data. In Fig. 6.25 one can see similar results for the fit parameters. Again, low MVA are strongly affected by a realistic atmosphere.
Two individual golden hybrid events with large differences are selected and shown in Table 6.4. For instance, differences of 0.2 - 0.3 deg in the space angle and $\sim 10\%$ in energy can occur! Differences between t_i^{exp}(vac) and t_i^{exp}(real) are usually around zero. This is not surprising because the job of minimization procedure is to minimize the difference between t_i^{exp} and t_i by finding the appropriate values of R_p, χ_0 and t_0, so the effect on different speed of light models bias these fit parameters.

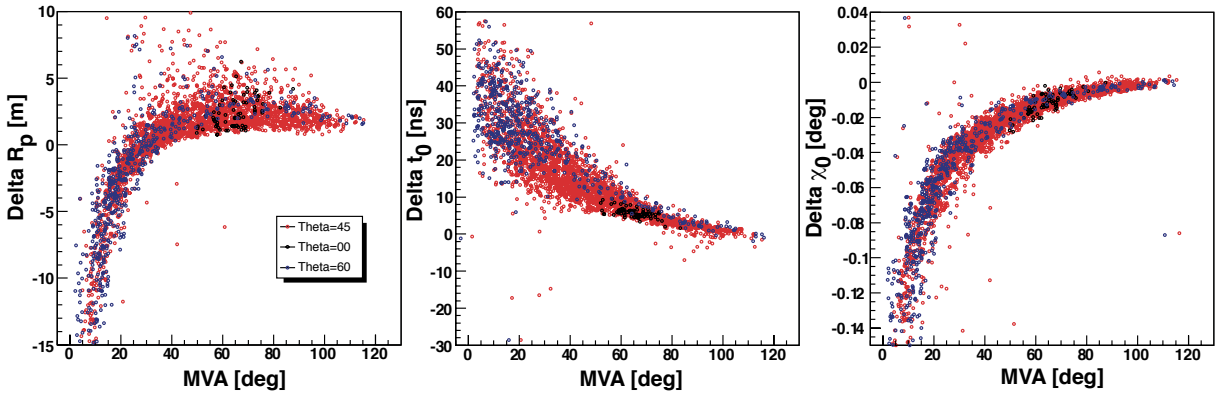

Figure 6.25: *Golden Hybrid Data*: Fit parameters as a function of minimum viewing angle. Note that "vac" indicates the speed of light in vacuum and "real" the reduced speed of light. "Delta" refers to $x_{\text{vac}} - x_{\text{real}}$. Different inclination angles ϑ are color coded (black $\rightarrow \vartheta = 0$ deg, red $\rightarrow \vartheta = 45$ deg and blue $\rightarrow \vartheta = 60$ deg).

	Event: 995272			**Event: 1196177**		
	Vacuum	*Real*	Δ(vac − real)	*Vacuum*	*Real*	Δ(vac − real)
R_p [m]	15595	15681	-86	7662	7654	8
χ_0 [deg]	53.33	53.64	-0.31	43.85	44.19	-0.34
t_0 [ns]	10202	9926	276	21020	20937	83
ϑ_{axis} [deg]	51.39	51.21	0.18	50.52	50.23	-0.01
φ_{axis} [deg]	89.94	90.26	-0.32	87.96	88.18	-0.22
E [EeV]	3.72	3.31	0.41	1.78	1.74	0.04
X_{max} [g/cm^2]	846	821	25	744	748	-4
MVA [deg]	33.67	33.98	-0.31	22.89	23.22	-0.33
CherFrac. [%]	12	17	-5	29	28	1
Core X [m]	12632	12652	-20	4352	4322	30
Core Y [m]	14704	14727	-23	10122	10049	73

Table 6.4: Reconstructed parameters for two individual events.

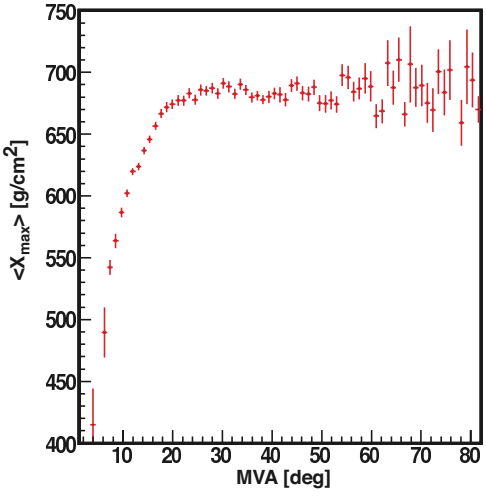

Figure 6.26: Mean X_{max} as a function of MVA. Hybrid data are used and geometry cuts are applied (see [105]).

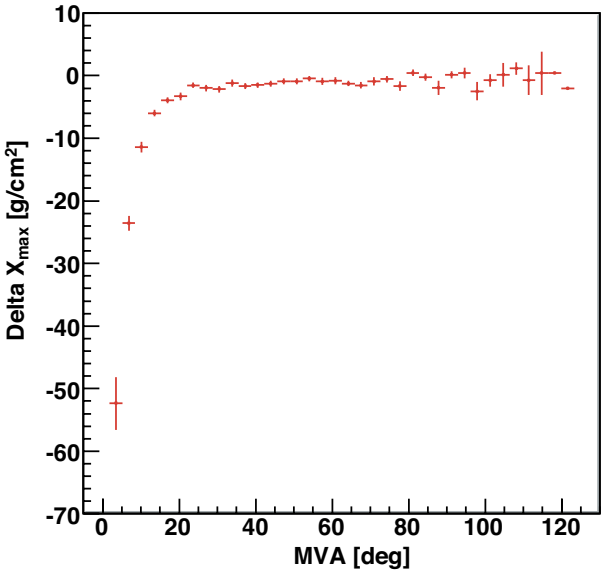

Figure 6.27: ΔX_{max} as a function of MVA. Note that "vac" indicates the speed of light in vacuum and in "real" de-excitation times, reduced speed of light and bending of light is included. "Delta" refers to X_{max}(vac) − X_{max}(real).

The differences between the reconstructed X_{max} values for the golden hybrid data set are shown in Fig. 6.27. For very small MVA, a systematic shift may be noted. In [105] it is already noted, that the average X_{max} of events with low MVA (large Čerenkov

contamination) are systematically shallower as shown in Fig. 6.26. The impact of a reduced speed of fluorescence light could be an explanation for that behavior (adjustment into the correct direction), but first tests on golden and brass hybrid events could not fully explain the observed large differences [90]. There may be some larger differences also due to a bended path for fluorescence light (cf. Sec. 6.6). Other explanations emanate from an incompleteness of the Čerenkov correction algorithm or a natural trigger effect. Since the effect is not completely understood events with low MVA have to be removed and cuts are applied.

6.6 Bending of light

In addition to the time delay, the light path also changes according to Fermat's principle resulting in an aberration of the viewing angle χ_i as discussed in Section 6.5.1. Consequently, the telescope "detects" the light higher in the atmosphere than it was actually produced. The situation is sketched in Fig. 6.28. An angular difference of $\Delta\chi_i = \chi_i^{\text{obs}} - \chi_i^{\text{real}} \sim 0.05$ deg implies a shifted observed emission point of about $h = 30$ m higher at a distance of $d = 30$ km. That could cause a delay of ∼100 ns for the expected impact time on ground [106]. This is particularly important for hybrid observations where the same EAS is detected by the ground array and a fluorescence detector as it is realized at the Pierre Auger Observatory. The resulting relative timing offset has to be taken into account for an accurate reconstruction (cf. Sec. 6.8).
The implementation into the OFFLINE software is not as straight forward as it was for the other effects, since there is also some impact on the SDP reconstruction. Assuming

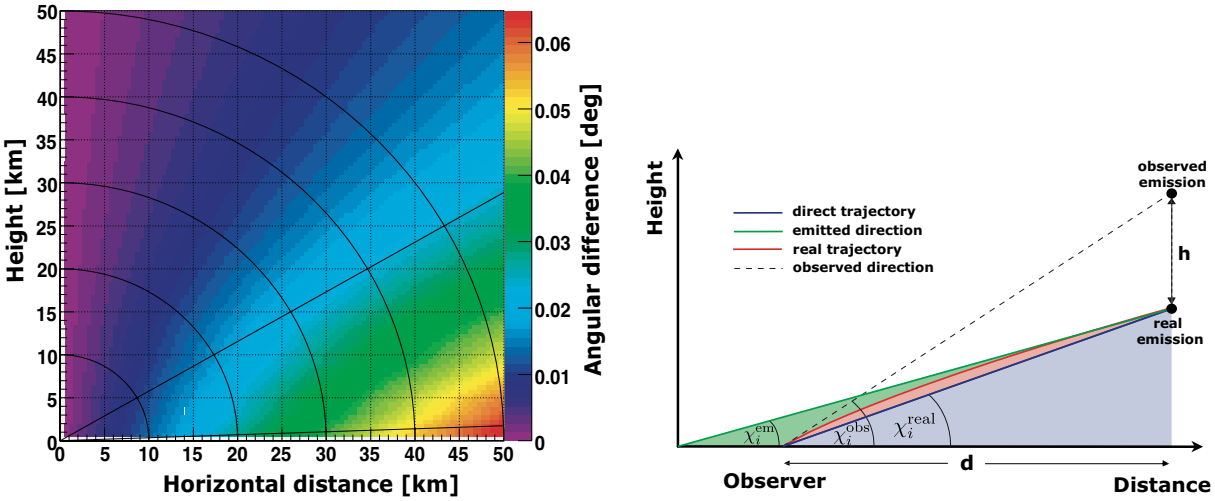

(a) Arrival angle difference between emitted and observed direction for a realistic atmosphere. The different colors indicate the difference $\chi_i^{\text{obs}} - \chi_i^{\text{em}}$ in deg.

(b) Illustration of the path deviation and the resulting impact on the observed emission point.

Figure 6.28: Illustration of the arrival angle difference and the underestimation in height.

a vertical SDP ($\vartheta_{\mathrm{SDP}} = 90$ deg) the observed and real emission point is located within the SDP. The angular difference between emitted and observed direction can easily be calculated with Eqn. 6.19 to be

$$\Delta\chi_i = \left(\frac{\pi}{2} - \chi_i^{\mathrm{obs}}\right) - \arcsin\left(\frac{n_{\mathrm{P}}}{n_0} \cdot \sin(\pi/2 - \chi_i^{\mathrm{obs}})\right) \ , \tag{6.28}$$

where n_P and n_0 denotes the index of refraction at emission and receiving point, respectively. Before the expected arrival time is calculated the real viewing angle χ_i^{real} has to be determined. As a first approximation one has $\chi_i^{\mathrm{real}} \approx \chi_i^{\mathrm{obs}} - \Delta\chi_i/2$. If ϑ_{SDP} is tilted (i.e. NOT around 90 deg) the situation changes and the calculated real emission point is not within the SDP. Typical values of $\Delta\chi_i$ are around 0.01 - 0.02 deg and compared to the uncertainties in the SDP (around 0.1 deg) this seems to be a minor effect, but one has to take into account that also $\Delta\chi_i$ is reduced for a tilted SDP. The final change in $\Delta\chi_i$ can therefore be written as

$$\chi_i^{\mathrm{real}} = \chi_i^{\mathrm{obs}} - \frac{\Delta\chi_i}{2} \cdot \sin\vartheta_{\mathrm{SDP}}. \tag{6.29}$$

6.7 Impact on real data including all discussed effects

To see the impact on real data, the golden hybrid data set from the previous sections is used with the same quality and profile cuts. According to the discussed effects of de-excitation times, reduced speed and bending of light, the final expected arrival time t_i^{exp} at the telescope can be written as

$$t_i^{\mathrm{exp}} = t_0 - \frac{R_p}{c}\left(\frac{1}{\tan(\chi_0 - \chi_i^{\mathrm{real}})}\right) + \frac{R_p}{c_i'}\left(\frac{1}{\sin(\chi_0 - \chi_i^{\mathrm{real}})}\right) + \tau(h) \tag{6.30}$$

where $\tau(h)$ denotes the de-excitation time, c_i' an effective speed of light and χ_i^{real} a bended viewing angle for a particular path i. The effect on the fit parameters as a function of $R_{X_{\mathrm{max}}}$ and MVA is shown in Fig. 6.29 and Fig. 6.30, respectively.

6.8 Time synchronization between SD and FD

As already discussed in Sec. 4.6 a precise determination of the SD/FD time offset is essential for an accurate hybrid reconstruction. The time offset is defined as the difference between SD and FD time measurements of the same event, taking into account different light travel distances. The performance requirements of the Pierre Auger Observatory specify that the SD/FD time offset should be known and stable within 125 ns and 95% certainty [107]. Several attempts have been made to determine the offset using different measurement techniques [108, 109]:

- **Using vertical laser shots:**
  In this technique vertical laser shots are fired from the CLF (cf. Sec. 4.3). The laser

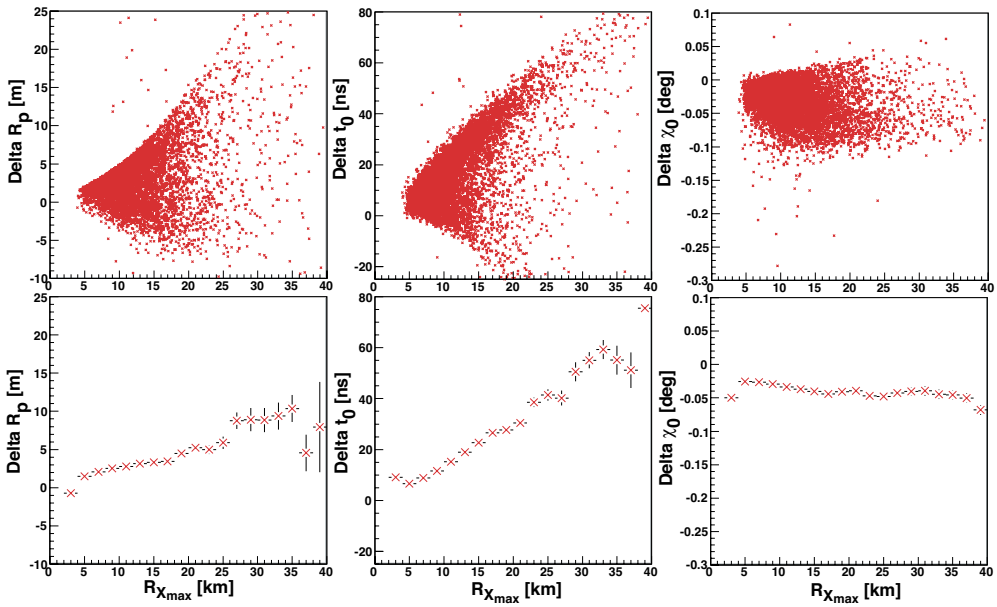

Figure 6.29: Effect on R_p, χ_0 and t_0 as a function of $R_{x_{\max}}$ for golden hybrid data as a profile plot (upper panel) and a scatter plot (lower panel). Note that "vac" indicates the speed of light in vacuum and in "real" de-excitation times, reduced speed of light and bending of light (cf. Eqn. 6.28) is included. "Delta" refers to $x_{\text{vac}} - x_{\text{real}}$.

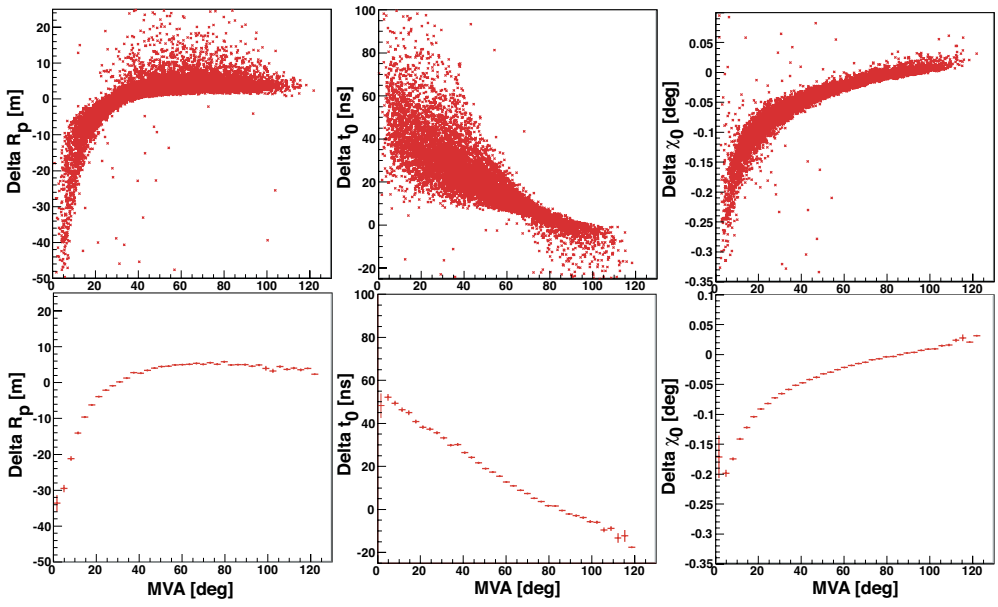

Figure 6.30: Effect on R_p, χ_0 and t_0 as a function of MVA for golden hybrid data as a profile plot (upper panel) and a scatter plot (lower panel). Note that "vac" indicates the speed of light in vacuum and in "real" de-excitation times, reduced speed of light and bending of light (cf. Eqn. 6.28) is included. "Delta" refers to $x_{\text{vac}} - x_{\text{real}}$.

light is split into two fractions where one is sent via an optical fiber to a near surface detector (Celeste, 20 m away), and the other one is fired vertically into the night sky. The scattered light is then detected by the fluorescence detector. In this way a hybrid event is simulated in a "real" way. In this study, the accuracy of the alignment of the laser beam has to be taken into account which is ~ 0.02 deg and the accuracy of the camera alignment can be estimated from star track measurements to be better than 0.05 deg. The time offset is calculated by comparing the estimated laser firing times by FD and SD measurements. The FD laser firing time is calculated by a one parameter fit to the $\chi_i - t_i$ curve keeping R_p and χ_0 fixed with varying t_0 (time at which the shower passes the closest distance to the telescope). The resulting SD/FD time offsets for different telescope stations are shown in Fig. 6.31.

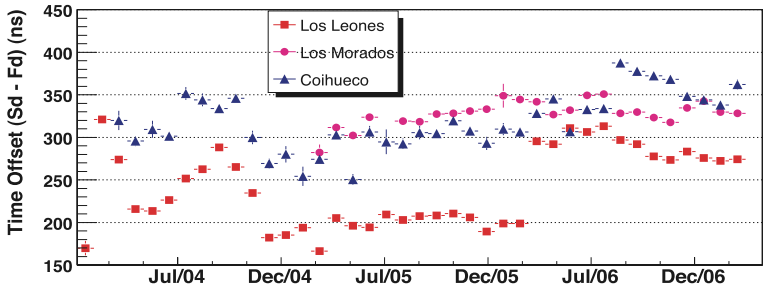

Figure 6.31: SD/FD time offset (SD - FD) for vertical laser shots of Los Leones (red), Los Morados (magenta) and Coihueco (blue) [90].

- **Using very inclined laser shots:**
  The advantage of inclined laser shots is, that they produce much narrower pulses resulting in more accurate synchronization measurements, because the pulse centroid is easier to determine. Another advantage for vertical shots arises from the fact that the small telescope alignment errors in azimuth do not affect the measurement of the time offset, since the SDP is the same for vertical and inclined laser shots. The approach to determine the timing offset differs slightly from the previous one and is described in [109]. The resulting SD/FD time offset for inclined shots is shown in Fig. 6.32.

- **Using golden hybrid events**
  The basic principle to determine the SD/FD offset with real events arises from differences in core positions for hybrid and stand-alone reconstructions. The accuracy of the SD reconstructed core is about 200 m and there should be no preferable direction. However, on closer inspection one can find for inclined showers an asymmetry in the tank-signal distribution on ground. Tanks that are underneath the shower axis will not only trigger the signal first, but will also have a stronger signal than tanks triggering the event late. This effect may bias the SD core position and hence the SD/FD offset measurements. For near vertical showers this effect is negligible and the SD core position has no preferred direction in contrast to the hybrid core.

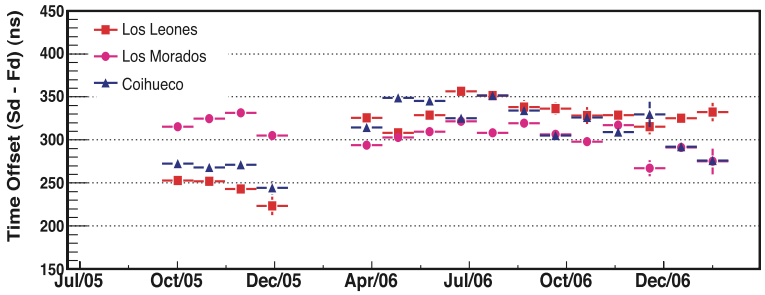

Figure 6.32: SD/FD time offset (SD - FD) for inclined (3 deg elevation) laser shots of Los Leones (red), Los Morados (megenta) and Coihueco (blue). Only pixels with an elevation < 5 deg were used to determine the offset [90].

This reconstructed core is sensitive to the SD/FD time offset which means, that the core may be systematically shifted away or closer to the fluorescence detector depending on the timing offset. To determine the offset, first the distance between SD and hybrid reconstructed core is computed. If there is no offset one can expect that differences in the core positions center around zero. In general, these distances do not center around zero as shown in Fig. 6.33. The corresponding time offset for

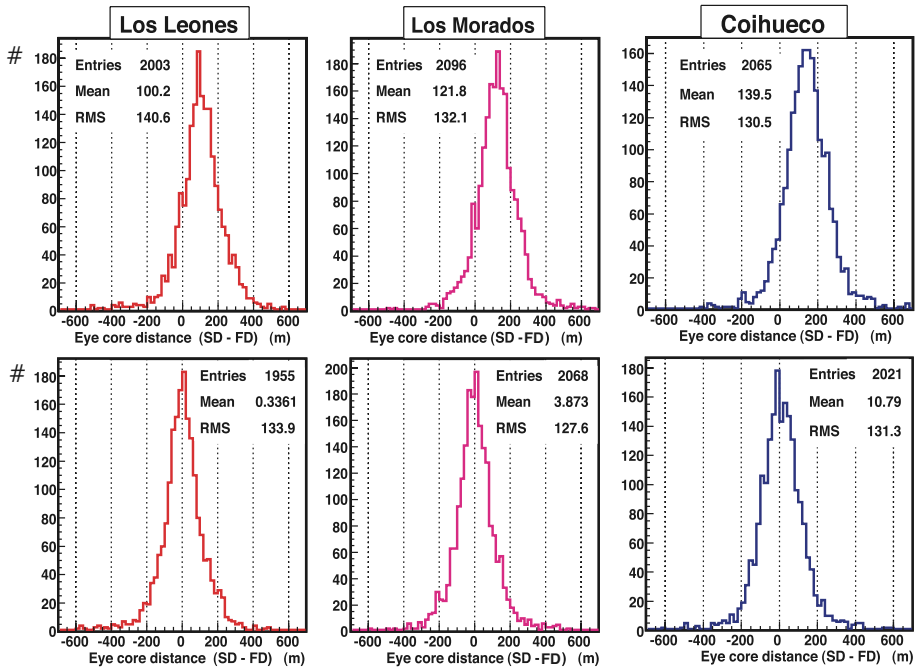

Figure 6.33: Histogram for eye-core distances for Golden Hybrid events [90]. **(Upper panel)**: The distributions at the top are assuming a perfect synchronization between SD and FD (time offset equal to zero). **(Lower panel)**: Distributions assuming an offset of 350 ns for Los Leones, 420 ns for Los Morados and 470 ns for Coihueco, respectively.

each eye is then computed by variation of the time offset until the core distances center around zero.

- **Using the reconstructed $X_{\max}$**
  As already explained, the determination of the timing offset with the SD and hybrid core position is only possible for near vertical showers. On the other hand fast showers (low duration) will produce a bigger impact on the reconstructed hybrid geometry. Using these showers one has to take into account the asymmetry in the tank-signal distribution. To avoid these difficulties one can try to measure the offset utilizing the calculated $X_{\max}$ of the shower. If $X_{\max}$ is sensitive to the reconstructed geometry, then it is also sensitive to the SD/FD time offset. To identify fast and incoming showers, the MVA (cf. App. B.1) seems to be an adequate parameter. As shown in Fig. 6.26 the mean MVA declines strongly for MVA < 20 deg. By changing the time offset one can change the slope to be more shallow as shown in Fig. 6.34. Events with larger MVA are not affected by the time offset, because their duration

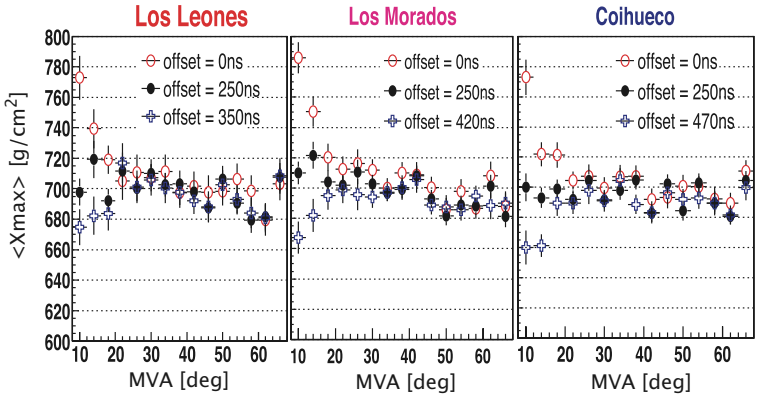

Figure 6.34: Mean $X_{\max}$ as a function of MVA assuming three different time offsets. A time offset of 250 ns produces a mean $X_{\max}$ independent of the MVA [90].

is of the order of a few μs which is large compared to an offset of 200 ns. Clearly this method assumes a correct Čerenkov correction algorithm. More studies on that issue are in preparation.

Recapitulatory one can say that all methods point out a relatively large timing offset of $\sim 250 - 350$ ns which are not yet understood. Any insights are very valuable.

6.8.1 Determine the expected time offset using a toy model

The aim of the toy model is, to simulate the impact of the aforementioned atmospheric effects (like de-excitation times, reduced speed of light and bended fluorescence light) to the SD/FD time offset. The program is written in C++ using the already provided code from the previous sections. Since one is only interested in timing differences between

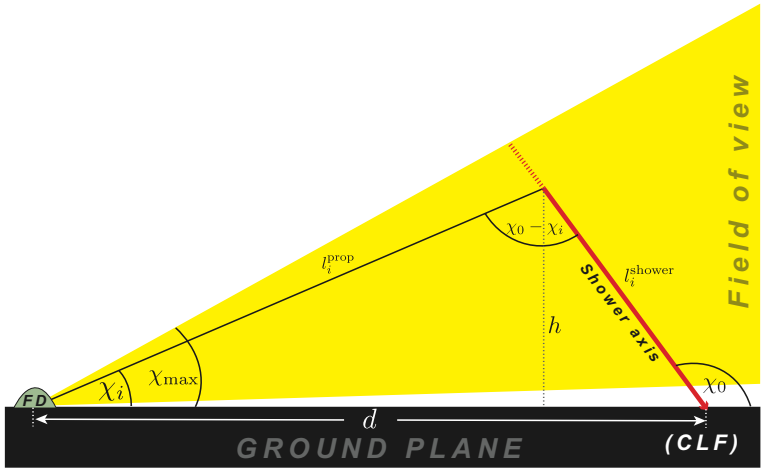

Figure 6.35: Illustration of the geometry of the toy model. The yellow area indicates the field of view of the telescope, here 1-30 deg. Only fluorescence light from this direction is taken into account. For this analysis a flat earth is assumed.

standard and modified reconstruction other (unchanged) effects like light attenuation, curved earth, Čerenkov contamination, camera misalignment a.s.o. are not involved in the code. Furthermore, the toy model reduces the simulation to a two dimensional problem which makes the determination of the SDP dispensable (always vertical to the ground). The approach for the geometry reconstruction within the SDP is similar to [109] and illustrated in Fig. 6.35.

6.8.2 CLF simulation

To simulate CLF events, a distance $d = 26$ km was assumed, corresponding roughly to the distance between Los Leones and the CLF. The height a.s.l. of the ground plane is assumed to be 1416 m taking the altitude of the Pierre Auger Observatory into account. This is particularly important for the implementation of an index of refraction $\neq 1$. The expected fluorescence light arrival time t_i^{exp} at the telescope can then be expressed as a function of the firing time t_{fire}. The arrival time can be written as (cf. Fig. 6.35)

$$\begin{aligned} t_i^{\text{exp}} &= t_{\text{fire}} + \frac{l_i^{\text{shower}}}{c} + \frac{l_i^{\text{prop}}}{c} \\ &= t_{\text{fire}} + \frac{d}{c}\frac{\sin\chi_i}{\sin(\chi_0 - \chi_i)} + \frac{d}{c}\frac{\sin\chi_0}{\sin(\chi_0 - \chi_i)} \\ &= t_{\text{fire}} + \frac{d}{c}\left(\frac{\sin\chi_0 + \sin\chi_i}{\sin(\chi_0 - \chi_i)}\right). \end{aligned} \tag{6.31}$$

Here c denotes the vacuum speed of light corresponding to the standard reconstruction software. The simulation program enables the possibility to switch on and off the discussed

atmospheric effects individually. In this way each effect can be investigated separately. The final timing offset is then obtained by a one parameter fit for Eqn. 6.31 where t_{fire} acts as a free parameter. All other values can be chosen freely within the simulation. Both, vacuum and realistic atmospheres are simulated. The simulation of the vacuum atmosphere acts also as a cross-check to give an expected firing time $t_{\text{fire}} = 0$.
A special feature of laser light is (in contrast to EAS propagation speed), that the propagation speed is also reduced by an index of refraction > 1 together with a bending of laser light. Additionally, the "fluorescence light" reaching the telescope is just scattered laser light and one has no excitation or de-excitation processes. All these circumstances are implemented within the simulation. The events are simulated in a range $70 \leq \chi_0\ [\text{deg}] \leq 178$ in steps of one degree. Table 6.5 summarizes several CLF simulations and Fig. 6.36 shows the calculated timing offset as a function of χ_0.

ID	SD	FD
1	with $n = 1.0003$	WITH $n(h)$ (fluorescence light) NO bended light (fluorescence light) NO $n(h)$ (laser light) NO bended light (laser light)
2	with $n = 1.0003$	NO $n(h)$ (fluorescence light) WITH bended light (fluorescence light, cf. Eqn. 6.28) NO $n(h)$ (laser light) NO bended light (laser light)
3	with $n = 1.0003$	WITH $n(h)$ (fluorescence light) WITH bended light (fluorescence light, cf. Eqn. 6.28) NO $n(h)$ (laser light) NO bended light (laser light)
4	with $n = 1.0003$	WITH $n(h)$ (fluorescence light) NO bended light (fluorescence light) WITH $n(h)$ (laser light) NO bended light (laser light)
5	with $n = 1.0003$	WITH $n(h)$ (fluorescence light) WITH bended light (fluorescence light, cf. Eqn. 6.28) WITH $n(h)$ (laser light) WITH bended light (laser light)
6	with $n = 1.0$	WITH $n(h)$ (fluorescence light) WITH bended light (fluorescence light, cf. Eqn. 6.28) WITH $n(h)$ (laser light) WITH bended light (laser light)

Table 6.5: Different CLF simulations. The ID is used as an identification number for Fig. 6.36. SD corresponds to the expected firing time using a vacuum atmosphere whereby FD denotes for the implemented corrections.

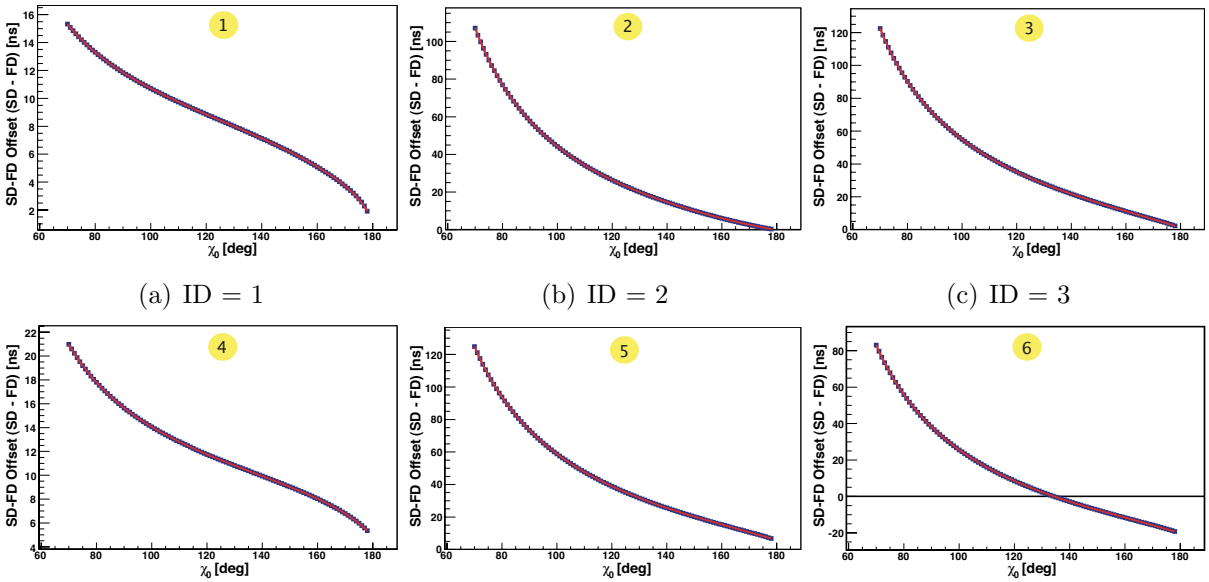

(a) ID = 1 (b) ID = 2 (c) ID = 3

(d) ID = 4 (e) ID = 5 (f) ID = 6

Figure 6.36: Time offset simulation as a function of χ_0 for CLF events using a toy model. The different ID's are explained in Table 6.5. The SD time corresponds to the expected firing time using a vacuum atmosphere whereby FD denotes for the implemented corrections.

In some simulations, a vacuum index of refraction of $n_{\text{vac}} = 1.0003$ was used to have a better comparison to [109]. One can see that in general the expected FD firing time is earlier than SD[3], such as the findings discussed in Sec. 6.8, with a stronger effect for low χ_0 angles (coming in showers). Furthermore, the offset seems to be larger with implemented bending of light. This is consistent with the incorrect estimation of the light emission point as shown in Fig. 6.28 (b). Note, that for low χ_0 no light attenuation is taken into account and that the effect of the reduced speed of light is stronger for those events.

6.8.3 Real event simulation

Real events were simulated in a slightly different way than CLF events. The starting position is always along the edge of the field of view of the telescope. For a better comparison to CLF events the impact point is always set to a distance of 26 km from the telescope. Since the event is starting at another position than before, one has to think about a new parameterization of the expected fluorescence arrival time t_i^{exp} at the telescope. With the law of sines, the expected impact time t_{imp} on ground can be calculated to be

$$t_{\text{imp}} = \frac{d}{c} \frac{\sin \chi_{\text{max}}}{\sin(\chi_0 - \chi_{\text{max}})} \ , \tag{6.32}$$

[3]The SD time corresponds to the expected firing time using a vacuum atmosphere whereby FD denotes the implemented corrections.

with the vacuum speed of light c and the maximum angle $\chi_{\max}$ for the field of view (in this case 30 deg). Once the expected impact time is calculated $t_i^{\exp}$ becomes

$$\begin{aligned} t_i^{\exp} &= t_{\text{imp}} - \frac{l_i^{\text{shower}}}{c} + \frac{l_i^{\text{prop}}}{c} \\ &= t_{\text{imp}} - \frac{d}{c}\frac{\sin\chi_i}{\sin(\chi_0-\chi_i)} + \frac{d}{c}\frac{\sin\chi_0}{\sin(\chi_0-\chi_i)} \\ &= t_{\text{imp}} + \frac{d}{c}\left(\frac{\sin\chi_0-\sin\chi_i}{\sin(\chi_0-\chi_i)}\right) \end{aligned} \tag{6.33}$$

Eqn. 6.33 is now used for a one parameter fit where t_{imp} acts as a free parameter. To see differences in the core location the expected impact time was fixed to the vacuum expectation and a one parameter fit for d was performed. Clearly, the propagation speed of the shower front is now assumed to be c with no bending and de-excitation times are taken into account. The events are simulated in a range $35 \leq \chi_0$ [deg] ≤ 178 in steps of one degree. Table 6.6 summarizes simulated real events with different characteristics and Fig. 6.37 shows the calculated timing offset and Fig. 6.38 differences in the expected impact point as a function of χ_0.

As one can see in Fig. 6.37 the expected impact time for FD measurements in general is delayed compared to SD measurements. The effect of de-excitation times is negligible for low altitude emission, but becomes more important in high altitudes (cf. Fig. 6.37 (A)). The most important effect arises from light bending as shown in Fig. 6.37 (C) which also gives the shape of the over-all effect (D). For very inclined going away showers time differences of more than 200 ns are possible. The little drop in (D) for low χ_0 is the result

ID	SD	FD
A	$n(h)=1$	WITH de-excitation times NO $n(h)>1$ NO bended fluorescence light
B	$n(h)=1$	NO de-excitation times WITH $n(h)>1$ NO bended fluorescence light
C	$n(h)=1$	NO de-excitation times NO $n(h)>1$ WITH bended fluorescence light (cf. Eqn. 6.28)
D	$n(h)=1$	WITH de-excitation times WITH $n(h)>1$ WITH bended fluorescence light (cf. Eqn. 6.28)

Table 6.6: Different real simulations. The ID is used as an identification number for Fig. 6.37 and Fig. 6.38. SD corresponds to the expected firing time using a vacuum atmosphere whereby FD denotes for the implemented corrections.

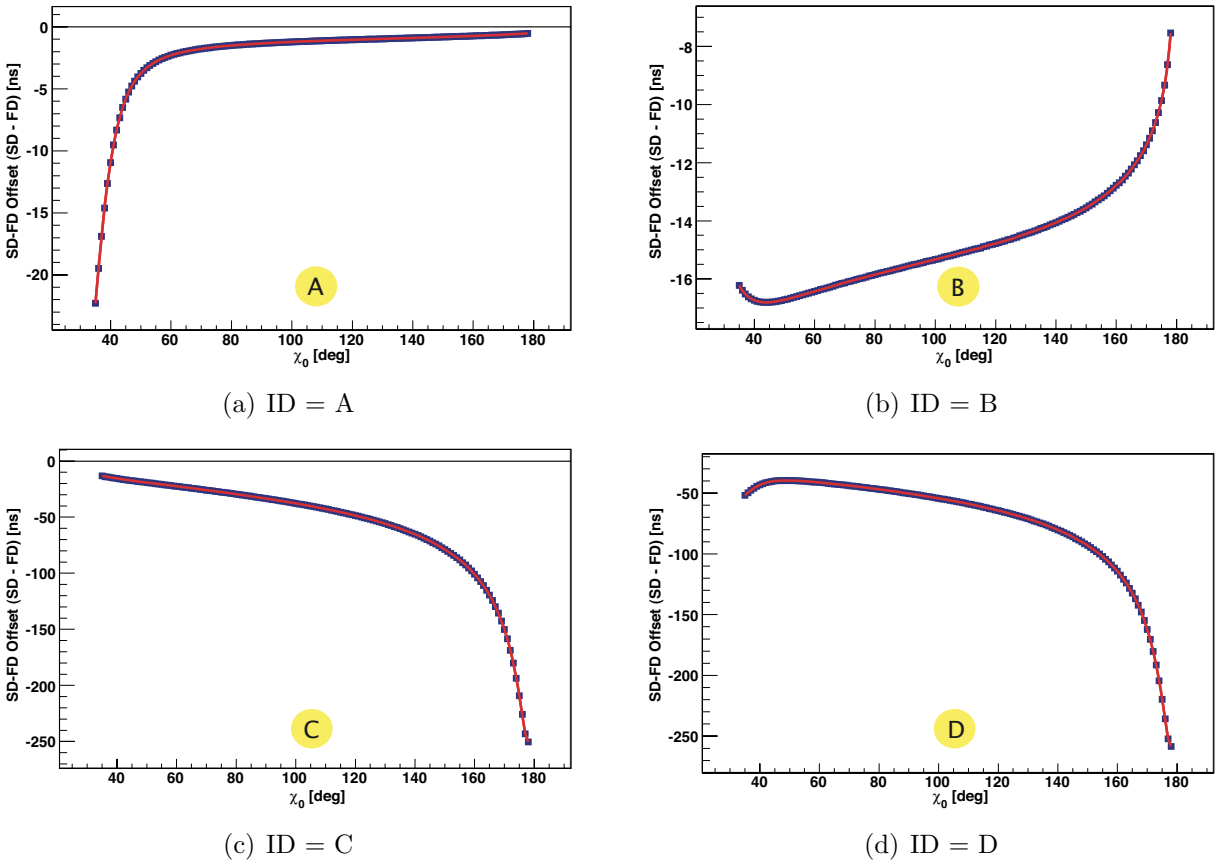

(a) ID = A

(b) ID = B

(c) ID = C

(d) ID = D

Figure 6.37: Time offset simulation as a function of χ_0 for real events using a toy model. The different ID's are explained in Table 6.6. The SD time corresponds to the expected impact time using a vacuum atmosphere whereby FD denotes the implemented corrections.

of de-excitation times high in the atmosphere.
The impact point differences are shown in Fig. 6.38. In general, the SD reconstructed core is closer to the telescope than FD. One can understand this by considering that the fluorescence light is expected to arrive later and therefore the shower is shifted away from the telescope. Additionally, the bending of light is strongest at low altitudes far away from the detector (cf. Fig. 6.28) resulting in a lifting of the expected shower axis in this area. That means inclined going away showers are reconstructed further away. Another attribute of the core positions is, that for $\chi_0 \rightarrow 180$ deg the SD and FD impact point seems to be almost equal again. This can be explained by considering that the arrival angle does not change for $\chi_0 \rightarrow 180$ deg because the index of refraction does not change causing a peak in the maximum impact point aberration.

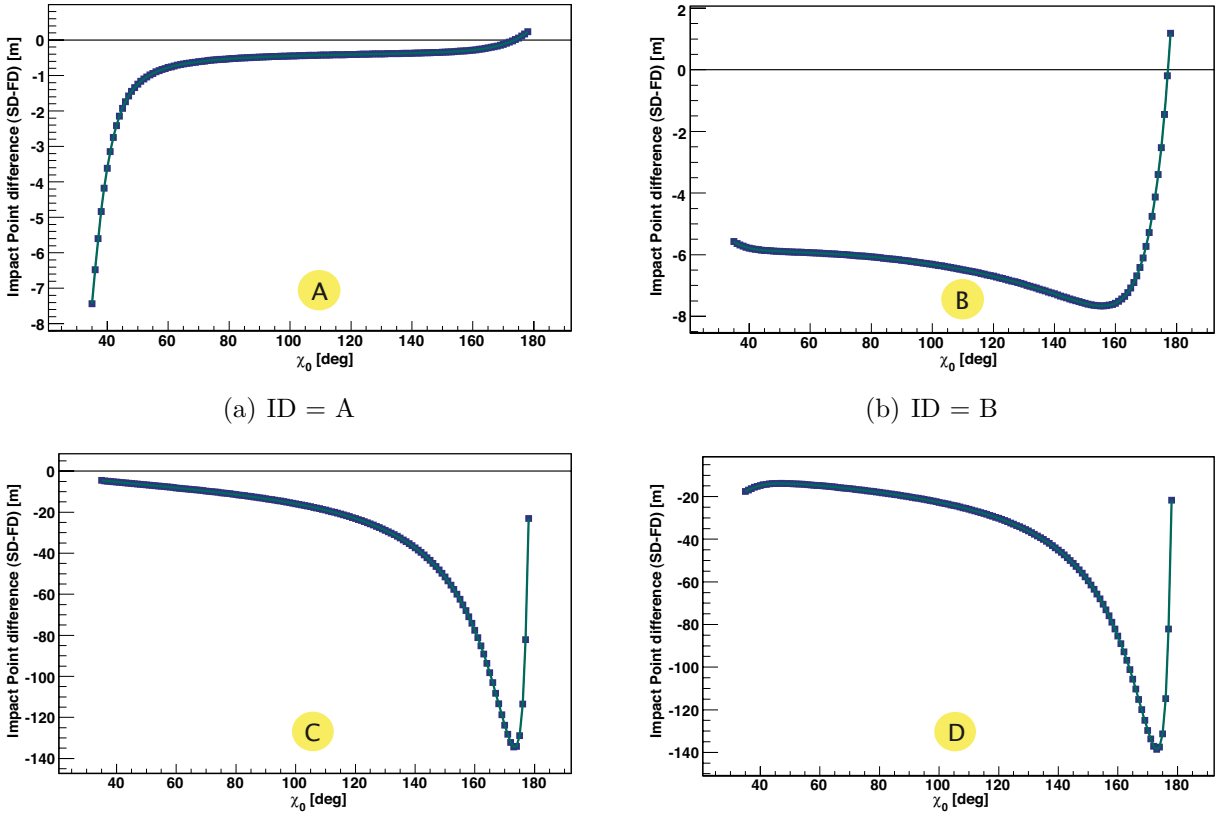

(a) ID = A

(b) ID = B

(c) ID = C

(d) ID = D

Figure 6.38: Core simulation as a function of χ_0 for real events using a toy model. The different ID's are explained in Table 6.6. The SD time corresponds to the expected impact point using a vacuum atmosphere whereby FD denotes the implemented corrections.

Chapter 7

Conclusion and Outlook

7.1 Pulse Centroid Uncertainty

Several approaches were made to parameterize the pulse centroid uncertainty in a more physical and stable way than it is done right now. It was demonstrated that it is possible to use just the charge and duration of the pulse. Ansatz 1 utilizes the following relation with 6 degrees of freedom

$$t_i^{\mathrm{err}} = f(\mathrm{charge}) \cdot g(\mathrm{duration}) \cdot w_i \tag{7.1}$$

$$= \left(\frac{f_1}{\mathrm{charge} - f_2} + f_3 \right) \cdot (g_1 \cdot \mathrm{duration} + g_2) \cdot w_i \ , \tag{7.2}$$

with $f_1 = 55000$, $f_2 = -10$, $f_3 = 9$, $g_1 = 6.85$, $g_2 = 23.97$ and $w_i = 1/37$. Ansatz 2 aimed for a parametrization of just one degree of freedom

$$t_i^{\mathrm{err}} = \frac{\mathrm{duration}}{\sqrt{\mathrm{charge}}} \cdot q_i \ , \tag{7.3}$$

with $q_i = 222$. It was shown, that the current parametrization of the pulse centroid uncertainty is underestimated for high energy far away and going away showers. It seems to be that the first approach is able to reduce the aforementioned shortcomings, but further studies may be desirable to find a completely satisfying estimate of the pulse centroid uncertainty.

7.2 Geometry Reconstruction Revisited

In the second part the geometry reconstruction of fluorescence light was revisited. It was shown, that the "classical" calculation, derived by just geometrical considerations, of the light arrival time [26]

$$t_i^{\mathrm{exp}} = t_0 + \frac{R_p}{c} \tan\left(\frac{\chi_0 - \chi_i}{2} \right) \tag{7.4}$$

has to be adjusted when accounting for atmospheric effects:

- **De-excitation times**:
  The expected arrival time $t_i^{\rm exp}$ is delayed by a time $\tau(h)$ due to de-excitation processes within the shower development induced by low energy electrons and positrons ($\sim$ 40 MeV). Almost all of the air fluorescence (in the wavelength range between 300 nm and 400 nm) originates from transitions of molecular nitrogen N_2 or molecular nitrogen ions N_2^+. De-excitation times can be of the order of 30-40 ns but are reduced by quenching effects especially at low altitudes where the air-density is larger. Below 20 km de-excitation times are smaller than 5 ns. The expected lifetime τ in ns as a function of height h in m can be parameterized in good approximation to be
  $$\tau(h) = \frac{\tau_{0_{\nu'}}}{\alpha \cdot e^{-h/H} + 1} \ , \tag{7.5}$$
  with $\tau_{0_{\nu'}} = 37.5$ ns, $H = 8005$ m and $\alpha = 95$.

- **Reduced speed of fluorescence light**:
  The propagation speed of fluorescence light $v = c/n$ is reduced by an index of refraction $n > 1$ which is a function of the traversed medium and wavelength λ. To estimate the impact of a realistic atmosphere differences of the light arrival times between the cases of vacuum and realistic speed of light were calculated from different parts of the atmosphere. Differences of more than 30 ns can occur especially for light propagating from far away and near the Earth's surface. Average arrival time differences are 10-25 ns.

- **Bending of fluorescence light**:
  In addition to the time delay, the light path also changes according to Fermat's principle resulting in an abberation of the viewing angle χ_i. Consequently, a simple back-extrapolation of the light arrival direction overestimates the height of the actual point of emission. An angular difference of $\chi_i^{\rm obs} - \chi_i^{\rm real} \sim 0.05$ deg implies a 30 m shift in height at 30 km distance which would cause a delay of $\sim$100 ns for the expected impact time on ground. Typical values for differences in χ_i amount to 0.01-0.02 deg. The real emission angle $\chi_i^{\rm real}$ can be approximated as (cf. Sec. 6.6)
  $$\chi_i^{\rm real} = \chi_i^{\rm obs} - \frac{\Delta\chi_i}{2} \cdot \sin\vartheta_{\rm SDP} \tag{7.6}$$
  with
  $$\Delta\chi_i = \left(\frac{\pi}{2} - \chi_i\right) - \arcsin\left(\frac{n_{\rm P}}{n_0} \cdot \sin(\pi/2 - \chi_i)\right) .$$

Implementing all these effects into Eqn. 7.4 the new expected arrival time can be written as

$$t_i^{\rm exp} = t_0 - \frac{R_p}{c}\left(\frac{1}{\tan(\chi_0 - \chi_i^{\rm real})}\right) + \frac{R_p}{c_i'}\left(\frac{1}{\sin(\chi_0 - \chi_i^{\rm real})}\right) + \tau(h) \ , \tag{7.7}$$

where $\tau(h)$ denotes the de-excitation time, c_i' an effective speed of light and χ_i^{real} a bended viewing angle for a particular path i. Taking all these effects into account the corrections amount up to $\simeq 0.2$ deg in arrival direction and a few percent in primary energy.

The impact on the SD/FD offset was calculated using a toy model. The main contribution to the offset arises from bended fluorescence light and has a dependence on χ_0. It could be shown that the SD recorded the events in general earlier (in real shower simulation) and that impact time differences of up to 200 ns can occur at very inclined shower geometries.

The implementation of the corrections into the OFFLINE reconstruction software is ongoing.

Appendix A

OFFLINE Example

As an example the application of the OFFLINE software is demonstrated for hybrid detector simulation and hybrid event reconstruction. This involves a combined treatment of SD and FD sequences.

A.1 Hybrid detector simulation

The first step is to create Monte Carlo generated air showers [43, 96]. Then a simulation of the response and triggering of the SD and FD is accomplished before finally, the event building and export to various data formats can be performed.
The module structure of the framework allows one to split the simulation process into a sequence of steps. An example for a hybrid detector simulation module sequence is shown in Fig. A.1. Intuitive names for the modules enhance the ability to follow the procedure sequence directly.

The simulation starts with an import of an appropriate Monte Carlo shower. In general one shower is used several times and placed at different positions on the array. The simulation of the surface detector begins typically with a module which places the shower impact point somewhere within the SD configuration followed by a module which determines the particles entering which tanks. In subsequent modules energy loss, Čerenkov light emission and detector response is simulated. Similarly, the FD response is separated into different modules. The fluorescence and Čerenkov light, emitted by the shower as it develops, is simulated as well as the propagation to the telescope. Finally, the response of the telescope, electronics and triggering is simulated before the event is built and exported.

A.2 Hybrid event reconstruction

Once the event is simulated it can be reconstructed within the hybrid event reconstruction chain. A part of the module sequence is shown in Fig. A.2.

In a first step, the calibration of the fluorescence and surface detectors is accomplished. The real or simulated raw data is transformed into physical quantities, before the pulse finding algorithm is started. This module locates the pulse related to the detection of fluorescence light from an air shower by maximization of a signal over noise (S/N) ratio. In order to reject accidental noise pixels triggered by background radiation a minimum requirement $S/N > 5$ ratio is used. After the determination of the pixels centroid, a series of geometrical reconstruction modules are employed. First, the plane containing the shower axis and the detecting eye[1] is determined by minimizing Eqn. 4.1. Within the HybridGeometryFinder module, the orientation of the shower axis within the SDP is determined by minimizing a combined χ^2-function[2] (Eqn. 4.8) using the expected light arrival time at the telescope together with the triggered PMTs. To estimate the total light received at the telescope the FdApertureLight module uses a S/N maximization algorithm to determine the optimal width ξ of the shower image on the camera. Via integration over all pixels inside the circle with radius ξ one can derive the number of photons at the telescope aperture as a function of time. The last step is the profile reconstruction, which converts the fluorescence light profile recorded by the telescope to a determination of the energy deposit at a given atmospheric depth along the shower axis (cf. Sec. 5.1).

[1] called shower-detector-plane (SDP).

[2] the χ^2-function consists of a SD and FD part. More details can be found in Section 4.6.

```
<!-- A sequence for a hybrid shower simulation -->
<sequenceFile>

    <!-- Loop over all Monte Carlo shower -->
    <loop numTimes="unbounded">

        <!-- Read in a Monte Carlo shower -->
        <module> EventFileReaderOG </module>

        <!-- Use each shower 10 times -->
        <loop numTimes="10">

            <!-- Position of the shower on array -->
            <module> EventGeneratorOG </module>

            <!-- SD simulation part -->
            <module> CachedShowerRegeneratorOG </module>
            <module> FastTankSimulatorOG </module>
            <module> SdPMTSimulatorOG </module>
            <module> SdFilterFADCSimulatorMTU </module>
            <module> SdBaselineSimulatorOG </module>
            <module> TankGPSSimulatorOG </module>
            <module> TankTriggerSimulatorOG </module>

            <!-- FD simulation part -->
            <module> ShowerLightSimulatorKG </module>
            <module> LightAtDiaphragmSimulatorKG </module>
            <module> TelescopeSimulatorKG </module>
            <module> FdBackgroundSimulatorOG </module>
            <module> FdElectronicsSimulatorOG </module>
            <module> FdTriggerSimulatorOG </module>

            <!-- Simulate trigger and build events -->
            <module> CentralTriggerSimulatorXb </module>
            <module> EventBuilderOG </module>

            <!-- Output and visualization -->
            <module> EventFileExporterOG </module>

        </loop>

    </loop>

</sequenceFile>
```

Figure A.1: Example of a module sequence for hybrid detector simulation in OFFLINE.

```
<!-- Part of the hybrid reconstruction chain -->

...

     <module> FdCalibratorOG </module>
     <module> SdFdPulseFinderOG </module>
     <module> CalibratorOG </module>
     <module> FdSDPFinderOG </module>
     <module> HybridGeometryFinderOG </module>
     <module> FdApertureLightOG </module>
     <module> FdProfileReconstructorKG </module>

...
```

Figure A.2: Part of the module sequence in hybrid reconstruction.

Appendix B

Parameters Used in this Thesis

B.1 Parameters

During this analysis parameters and abbreviations are used the meaning of which is not directly obvious. In the following some explanations are given:

- X_{max}: The slant depth at which the shower reaches the maximum number of particles (cf. Fig. B.1). The unit is usually g/cm^2. The parameter is very important for composition studies, because heavy primary particles develop faster in the atmosphere (smaller X_{max}) than lighter particles.
- $R_{X_{\mathrm{max}}}$: The distance from the telescope to the shower maximum, see Fig. B.1.

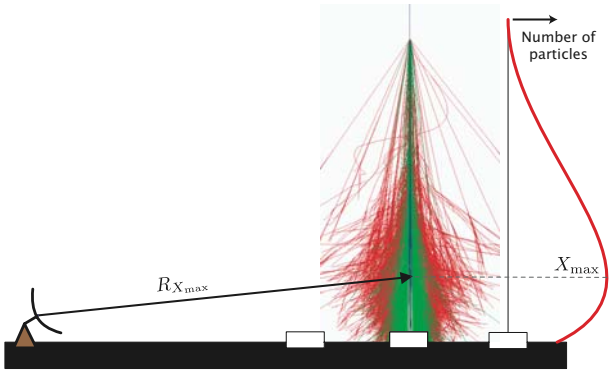

Figure B.1: Illustration of X_{max} and $R_{X_{\mathrm{max}}}$.

- *nPixels*: Number of triggered pixels per event.
- *sdpchisqr* and *tfitchisqr*: These are the SDP and timing fit χ^2.
- *maxDepth* and *minDepth*: Maximum and minimum shower depth in g/cm^2 observed by the telescope.

- *sd_fd_offset:*: This is the resultant SD/FD time offset after the minimization.
- *HybridFlag*: That flag indicates whether the event had a successful hybrid geometry reconstruction [110].

HybridFlag	= 1	when the value of 'sd_fd_offset' is less than 200 ns
HybridFlag	= 10	when 'tfitchisqr/(npixels-3)' is less than 5
HybridFlag	= 100	when 'Station_axis_distance' is less than 2000 m
HybridFlag	= 100	when none of the above conditions
HybridFlag	= 111	for a successful hybrid geometry reconstruction

- *Nstations*: Number of stations involved in the hybrid event. A station is considered involved in the hybrid event if its expected trigger time (assuming a flat shower front) is within 3000 ns from the actual station trigger time, and if the distance of the station (closest distance) to the SDP is less than 7000 m.
- *xmaxbk*: Equals 1 if $X_{\max}$ lies between maxDepth and minDepth, 0 otherwise.
- *axisthe* and *axisphi*: The angles ϑ_{axis} and φ_{axis} of the shower are defined using the core central system.
- *Minimum viewing angle (MVA)*: As shown in Fig. B.2 the viewing angle, under which an single event is seen by the detector, changes with shower development. The minimum viewing angle is defined as the smallest angle seen by the telescope. An MVA of 0 deg implies a shower pointing directly into the telescope. Usually only showers with MVA larger than 15-20 deg are taken into account to avoid a large Čerenkov contamination (cf. Sec. 6.5.5).

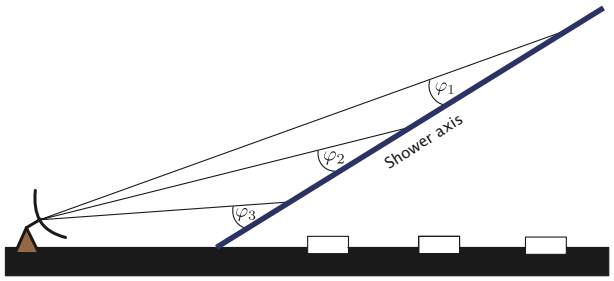

Figure B.2: Illustration of the minimum viewing angle, here φ_1.

B.2 Cuts

Table B.1 illustrates the basic quality and profile cuts that were used in this thesis.

xmaxbk	=	1
Minimum viewing angle (MVA)	>	20 [deg]
HybridFlag	>	110
maxDepth - minDepth	>	200 [g/cm^2]
R_p	>	0
χ_0	<	180 [deg]
N_{dof}(profile)	>	0

Table B.1: Quality cuts used for this analysis. For a more detailed explanation of the parameters see also App. B.1.

Bibliography

[1] V. F. Hess and W. Kolhoerster, "Über Beobachtungen der durchdringenden Strahlung bei sieben Freiballonfahrten," *Physikalische Zeitschrift* (1912).

[2] A. M. Hillas, *Cosmic rays*. The Commonwealth and International Library. Selected Readings in Physics, Oxford: Pergamon Press, 1972, 1972.

[3] G. V. Kulikov and G. B. Khristiansen *JETP 35* (1958), no. 635,.

[4] S. P. Knurenko, A. A. Ivanov, M. I. Pravdin, A. V. Sabourov, and I. Y. Sleptsov, "Recent results from Yakutsk experiment: development of EAS, energy spectrum and primary particle mass composition in the energy region of 10^{15}-10^{19} eV," *ArXiv Astrophysics e-prints* (Nov., 2006) `astro-ph/0611871`.

[5] M. Ave, J. Knapp, J. Lloyd-Evans, M. Marchesini, and A. A. Watson, "The energy spectrum of cosmic rays in the range 3×10^{17}-4×10^{18} eV as measured with the Haverah Park array," *Astroparticle Physics* **19** (Apr., 2003) 47–60, `astro-ph/0112253`.

[6] D. J. Bird *et al.*, "Evidence for correlated changes in the spectrum and composition of cosmic rays at extremely high energies," *Physical Review Letters* **71** (Nov., 1993) 3401–3404.

[7] S. Yoshida *et al.*, "The cosmic ray energy spectrum above 3×10^{18} eV measured by the Akeno Giant Air Shower Array," *Astroparticle Physics* **3** (Mar., 1995) 105–123.

[8] A. M. Hillas, "The origin of ultrahigh-energy cosmic rays," *Ann. Rev. Astron. Astrophys.* **22** (1984) 425–444.

[9] J. W. Cronin, S. P. Swordy, and T. K. Gaisser, "Cosmic rays at the energy frontier," *Sci. Am.* **276** (1997) 32–37.

[10] K.-H. Kampert, "Cosmic Rays from the Knee to the Ankle - Status and Prospects -," *ArXiv Astrophysics e-prints* (Nov., 2006) `astro-ph/0611884`.

[11] R. U. Abbasi *et al.*, "Measurement of the Flux of Ultrahigh Energy Cosmic Rays from Monocular Observations by the High Resolution Fly's Eye Experiment," *Physical Review Letters* **92** (Apr., 2004) 151101–+.

[12] M. Chikawa *et al.*, "Energy spectrum above 3×10^{18} eV observed with AGASA," in *International Cosmic Ray Conference*, pp. 333–+. 2001.

[13] R. C. Shellard, "First results from the Pierre Auger Observatory," *ArXiv Astrophysics e-prints* (Sept., 2006) `astro-ph/0609060`.

[14] T. Yamamoto and f. t. P. A. Collaboration, "The UHECR spectrum measured at the Pierre Auger Observatory and its astrophysical implications," `arXiv:0707.2638 [astro-ph]`.

[15] T. K. Gaisser and T. Stanev, "High-energy cosmic rays," *Nuclear Physics A* **777** (Oct., 2006) 98–110, `astro-ph/0510321`.

[16] T. K. Gaisser, *Cosmic rays and particle physics*. Cambridge and New York, Cambridge University Press, 1990, 292 p., 1990.

[17] K.-H. Kampert *et al.*, "Cosmic Ray Energy Spectra and Mass Composition at the Knee - Recent Results from KASCADE -," *Nuclear Physics B Proceedings Supplements* **136** (Nov., 2004) 273–281, `astro-ph/0410559`.

[18] J. R. Hörandel, "The composition of cosmic rays at the knee," *Nuovo Cimento B Serie* **120** (June, 2005) 825–+, `astro-ph/0407554`.

[19] V. Berezinsky, A. Gazizov, and S. Grigorieva, "Propagation and Signatures of Ultra High Energy Cosmic Rays," *Nuclear Physics B Proceedings Supplements* **136** (Nov., 2004) 147–158, `astro-ph/0410650`.

[20] **Pierre Auger** Collaboration, M. Aglietta *et al.*, "Anisotropy studies around the galactic centre at EeV energies with the Auger observatory," `astro-ph/0607382`.

[21] **AGASA** Collaboration, N. Hayashida *et al.*, "The anisotropy of cosmic ray arrival direction around 10^{18} eV," `astro-ph/9906056`.

[22] J. A. Bellido, R. W. Clay, B. R. Dawson, and M. Johnston-Hollitt, "Southern hemisphere observations of a 10^{18} eV cosmic ray source near the direction of the galactic centre," *Astropart. Phys.* **15** (2001) 167–175, `astro-ph/0009039`.

[23] W. F. Swann, "A Mechanism of Acquirement of Cosmic-Ray Energies by Electrons," *Physical Review* **43** (Feb., 1933) 217–220.

[24] E. Fermi, "On the Origin of the Cosmic Radiation," *Physical Review* **75** (Apr., 1949) 1169–1174.

[25] R. D. Blandford and J. P. Ostriker, "Particle Acceleration by Astrophysical Shocks," *Astrophys. J.* **221** (1978) L29–L32.

[26] P. Sokolsky, "Introduction to ultrahigh-energy Cosmic Ray physics,". Redwood City, USA: Addison-Wesley (1989) 208p.

[27] A. A. Penzias and R. W. Wilson, "A Measurement of excess antenna temperature at 4080-Mc/s," *Astrophys. J.* **142** (1965) 419–421.

[28] K. Greisen, "End to the cosmic ray spectrum?," *Phys. Rev. Lett.* **16** (1966) 748–750.

[29] G. T. Zatsepin and V. A. Kuzmin, "Upper limit of the spectrum of cosmic rays," *JETP Lett.* **4** (1966) 78–80.

[30] J. W. Cronin, "The highest-energy cosmic rays," *Nucl. Phys. Proc. Suppl.* **138** (2005) 465–491, `astro-ph/0402487`.

[31] G. R. Blumenthal, "Energy loss of high-energy cosmic rays in pair-producing collisions with ambient photons," *Phys. Rev.* **D1** (1970) 1596–1602.

[32] J. Linsley, "Evidence for a primary cosmic-ray particle with energy 10^{20}-eV," *Phys. Rev. Lett.* **10** (1963) 146–148.

[33] M. M. Winn, J. Ulrichs, L. S. Peak, C. B. A. Mccusker, and L. Horton, "The Cosmic Ray Energy Spectrum Above 10^{17} eV," *J. Phys.* **G12** (1986) 653–674.

[34] M. A. Lawrence, R. J. O. Reid, and A. A. Watson, "The Cosmic ray energy spectrum above $4{\cdot}10^{17}$ eV as measured by the Haverah Park array," *J. Phys.* **G17** (1991) 733–757.

[35] V. P. Egorova *et al.*, "The spectrum features of UHECRs below and surrounding GZK," *Nucl. Phys. Proc. Suppl.* **136** (2004) 3–11, `astro-ph/0408493`.

[36] M. Takeda *et al.*, "Energy determination in the Akeno Giant Air Shower Array experiment,". Prepared for 28th International Cosmic Ray Conferences (ICRC 2003), Tsukuba, Japan, 31 Jul - 7 Aug 2003.

[37] **HiRes** Collaboration, D. R. Bergman, "Observation of the GZK cutoff using the HiRes detector," `astro-ph/0609453`.

[38] P. Auger, P. Ehrenfest, R. Maze, J. Daudin, and A. F. Robley, "Extensive cosmic-ray showers," *Rev. Mod. Phys.* **11** (1939) 288–291.

[39] T. Bergmann *et al.*, "One-dimensional hybrid approach to extensive air shower simulation," *Astropart. Phys.* **26** (2007) 420–432, `astro-ph/0606564`.

[40] W. Heitler, *Quantum Theory of Radiation.* Oxford University Press, 1944.

[41] T. Gaisser and A. M. Hillas *Proc. 15th ICRC, Plovdiv, Bulgaria* **8** (1977) 353.

[42] P. W. Gorham, "On the possibility of radar echo detection of ultra-high energy cosmic ray and neutrino induced extensive air showers," *Astropart. Phys.* **15** (2001) 177–202, `hep-ex/0001041`.

[43] S. J. Sciutto, "Air shower simulations with the AIRES system," astro-ph/9905185.

[44] J. Linsley, "The structure function of EAS measured at Volcano Ranch. (Talk),". To appear in the proceedings of 13th International Cosmic Ray Conference (ICRC 1973), Denver, Colorado, 17-30 Aug 1973.

[45] M. T. Dova, M. E. Mancenido, A. G. Mariazzi, T. P. McCauley, and A. A. Watson, "A reinterpretation of Volcano Ranch lateral distribution measurements to infer the mass composition of cosmic rays," *Nucl. Phys. Proc. Suppl.* **122** (2003) 235–238, astro-ph/0210464.

[46] R. N. Coy, G. Cunningham, C. L. Pryke, and A. A. Watson, "The lateral distribution of extensive air showers produced by cosmic rays above 10^{19} eV as measured by water-Čerenkov detectors," *Astroparticle Physics* **6** (Mar., 1997) 263–270.

[47] A. N. Bunner *Sky and Telescope* **34** (1967) 204.

[48] R. M. Baltrusaitis *et al.*, "THE UTAH FLY'S EYE DETECTOR," *Nucl. Instrum. Meth.* **A240** (1985) 410–428.

[49] M. S. Longair, *High energy astrophysics. an informal introduction for students of physics and astronomy.* Cambridge: Cambridge University Press, 1981.

[50] D. J. Bird *et al.*, "Detection of a cosmic ray with measured energy well beyond the expected spectral cutoff due to cosmic microwave radiation," *Astrophys. J.* **441** (1995) 144–150.

[51] F. D. Kahn and I. Lerche, "Radiation from Cosmic Ray Air Showers," *Royal Society of London Proceedings Series A* **289** (Jan., 1966) 206–213.

[52] J. Jelley *et al.*, "Radio Pulses from Extensive Cosmic-Ray Air Showers," *Nature* **205** (1965) 327.

[53] H. Falcke and P. Gorham, "Detecting radio emission from cosmic ray air showers and neutrinos with a digital radio telescope," *Astropart. Phys.* **19** (2003) 477–494, astro-ph/0207226.

[54] T. Huege and H. Falcke, "Radio-emission from cosmic ray air-showers: A theoretical perspective for LOPES," astro-ph/0207647.

[55] **LOPES** Collaboration, T. Huege *et al.*, "Radio detection of cosmic ray air showers with LOPES," *Braz. J. Phys.* **36** (2006) 1157–1164, astro-ph/0609427.

[56] **Auger** Collaboration, "The pierre auger project design report,". FERMILAB-PUB-96-024.

[57] **Auger** Collaboration, "The Pierre Auger Observatory design report,". Second Edition, 1997, (http://www.auger.org/technical_info/design_report.html).

[58] J. Bluemer, "Das nördliche Pierre Auger-Observatorium." DPG Frühjahrstagung, Heidelberg, 2007.

[59] Z. Szadkowski, K. H. Becker, and K.-H. Kampert, "Development of a new first level trigger for the surface array in the Pierre Auger Observatory based on the Cyclone Altera FPGA," *Nucl. Instrum. Meth.* **A545** (2005) 793–802.

[60] **Pierre Auger** Collaboration, T. Suomijarvi, "The surface detectors of the Pierre Auger Observatory," *Nucl. Phys. Proc. Suppl.* **136** (2004) 393–398.

[61] **Pierre Auger** Collaboration, X. Bertou, "Performance of the Pierre Auger Observatory surface array," `astro-ph/0508466`.

[62] K.-H. Kampert, "The Pierre Auger observatory: Status and prospects," *Nucl. Phys. Proc. Suppl.* **151** (2006) 393–400, `astro-ph/0501074`.

[63] F. Kakimoto *et al.*, "A Measurement of the air fluorescence yield," *Nucl. Instrum. Meth.* **A372** (1996) 527–533.

[64] **Pierre Auger** Collaboration, R. Sato and C. O. Escobar, "The performance of the corrector lenses for the Auger fluorescence detector,". Presented at 29th International Cosmic Ray Conference (ICRC 2005), Pune, India, 3-11 Aug 2005.

[65] **Pierre Auger** Collaboration, J. A. Bellido, "Performance of the fluorescence detectors of the Pierre Auger Observatory," `astro-ph/0508389`.

[66] **Pierre Auger** Collaboration, P. Bauleo *et al.*, "Absolute calibration of the Auger fluorescence detectors," `astro-ph/0507347`.

[67] **Pierre Auger** Collaboration, C. Aramo *et al.*, "Optical relative calibration and stability monitoring for the Auger fluorescence detector," `astro-ph/0507577`.

[68] **Auger** Collaboration, M. A. Mostafa, "Atmospheric monitoring for the Pierre Auger fluorescence detector," `astro-ph/0308442`.

[69] **Pierre Auger** Collaboration, F. Arqueros *et al.*, "The central laser facility at the Pierre Auger observatory," *JINST* **1** (2006) P11003, `astro-ph/0507334`.

[70] **Pierre Auger** Collaboration, P. Allison *et al.*, "Timing calibration and synchronization of surface and fluorescence detectors of the Pierre Auger Observatory,". Presented at 29th International Cosmic Ray Conference (ICRC 2005), Pune, India, 3-11 Aug 2005.

[71] Internet:, "http://augersw1.physics.utah.edu/clf/, 06/27/07,".

[72] **Pierre Auger** Collaboration, S. Argiro *et al.*, "The offline software framework of the Pierre Auger Observatory,". Presented at 29th International Cosmic Ray Conference (ICRC 2005), Pune, India, 3-11 Aug 2005.

[73] M. Ambrosio *et al.*, "Application of Gnomonic Pro jections to the SDP reconstruction for FD events," *Internal Auger GAP-note,* GAP-2004-065.

[74] J. Bellido and V. Souza, "HybridGeometryFinder.cc," *2.2p4-mojo-svn_trunk, Line 204.*

[75] OFFLINE, "FdSDPFinder.cc," *2.2p4-mojo-svn_trunk, Line 848.*

[76] P. M. Younk and B. Fick, "On SDP Reconstruction Accuracy," *Internal Auger GAP-note,* GAP-2006-086.

[77] **Pierre Auger** Collaboration, J. Abraham *et al.*, "Properties and performance of the prototype instrument for the Pierre Auger Observatory," *Nucl. Instrum. Meth.* **A523** (2004) 50–95.

[78] **TA** Collaboration, K. Kasahara *et al.*, "The Current Status and Prospect of the Ta Experiment," astro-ph/0511177.

[79] **Pierre Auger** Collaboration, B. R. Dawson, "Hybrid Performance of the Pierre Auger Observatory," arXiv:0706.1105 [astro-ph].

[80] **Pierre Auger** Collaboration, M. D. Healy *et al.*, "Composition-sensitive parameters measured with the surface detector of the Pierre Auger Observatory," arXiv:0706.1569 [astro-ph].

[81] M. Mostafa, "Hybrid activities of the Pierre Auger Observatory," *Nucl. Phys. Proc. Suppl.* **165** (2007) 50–58, astro-ph/0608670.

[82] V. Souza *et al.*, "A hybrid reconstruction program and the hybrid resolution," *Internal Auger GAP-note,* GAP-2003-072.

[83] "Internet: Auger offline framework documentation, 2.2p4-mojo-svn_trunk, 07/13/07," *http://offline.p-ng.si/HybridGeometryFinder_8cc-source.html.*

[84] V. Holmes and B. Dawson, "Update on the Contributions of Cherenkov Light to the Width of the Shower Image," *Oral presentation Auger Collaboration Meeting, Malargue Argentina, March 2007.*

[85] M. Unger, "Shower Profile Reconstruction from Fluorescence and Cherenkov light," *Internal Auger GAP-note,* GAP-2006-010.

[86] M. Risse, D. Heck, and J. Knapp, "The CORSIKA Shower Library in Lyon after One Year of Production: Status and Experiences," *Internal Auger GAP-note,* GAP-2002-011.

[87] **Particle Data Group** Collaboration, K. Hagiwara *et al.*, "Review of particle physics," *Phys. Rev.* **D66** (2002) 010001.

[88] J. Bellido, B. Dawson, and D. Kuempel, "Parameterization of the Error for the Estimated Pulse Centroid," *Oral presentation at the Auger Analysis Meeting, Chicago United States, September 2006.*

[89] D. Kuempel, "Hybrid Reconstruction: Studies on different parametrizations for the pulse centroid error," *Oral presentation at the Auger Collaboration Meeting (given by K.-H. Kampert), Malargue Argentina, November 2006.*

[90] J. Bellido. Private communication.

[91] B. Dawson. Private communication.

[92] J. Bellido, "The Effect of the Camera Shadow on the Spot Shape and Pulse Centroid Time," *Oral presentation Auger Collaboration Meeting, Malargue Argentina, November 2006.*

[93] **High Resolution Fly's Eye** Collaboration, R. U. Abbasi *et al.*, "Measurement of the flux of ultrahigh energy cosmic rays from monocular observations by the High Resolution Fly's Eye experiment," *Phys. Rev. Lett.* **92** (2004) 151101, `astro-ph/0208243`.

[94] D. Kuempel *et al.*, "Delayed fluorescence light within Hybrid Reconstruction," *Internal Auger GAP-note,* `GAP-2007-059`.

[95] M. Risse and D. Heck, "Energy release in air showers," *Astropart. Phys.* **20** (2004) 661, `astro-ph/0308158`.

[96] D. Heck, G. Schatz, T. Thouw, J. Knapp, and J. N. Capdevielle, "CORSIKA: A Monte Carlo code to simulate extensive air showers,". FZKA-6019, Forschungszentrum Karlsruhe.

[97] B. Dawson, "Fluorescence Detector Techniques," *Internal Auger GAP-note,* `GAP-96-017`.

[98] T. Waldenmaier, "Spectral resolved measurement of the nitrogen fluorescence yield in air induced by electrons,". FZKA-7209, Forschungszentrum Karlsruhe.

[99] **Pierre Auger** Collaboration, B. Keilhauer *et al.*, "Atmospheric profiles at the southern Pierre Auger observatory and their relevance to air shower measurement," `astro-ph/0507275`.

[100] D. Kuempel *et al.*, "Effect of realistic speed of light on Hybrid Reconstruction," *Internal Auger GAP-note,* `GAP-2007-036`.

[101] L. Perrone and M. Risse, "Comparison of Cherenkov Light Emission in GEANT and CORSIKA," *Internal Auger GAP-note,* GAP-2002-060.

[102] D. Heck and T. Pierog, "Extensive Air Shower Simulation with CORSIKA: A User's Guide,".

[103] M. P. Kertzman and G. H. Sembroski, "Computer simulation methods for investigating the detection characteristics of tev air cherenkov telescopes," *Nucl. Instrum. Meth.* **A343** (1994) 629–643.

[104] R. C. Weast *et al.*, "CRC Handbook of Chemistry and Physics, 67th edition, 1986-1987,".

[105] J. Bellido, "Measuring the Mean Xmax as a Function of the Shower Energy Using the Hybrid Data," *Internal Auger GAP-note,* GAP-2007-019.

[106] D. Kuempel *et al.*, "Geometry Reconstruction of fluorescence detectors revisited,". Prepared for 30th International Cosmic Ray Conference, Merida Mexico, July 2007.

[107] **Pierre Auger** Collaboration, "http://www.auger.org/admin/specifications/node5.html," *Pierre Auger Project Performance Requirements and Technical Specifications* (Nov 24, 1998).

[108] J. Bellido, "Measurement of the time synchronization between the SD and the FD," *Internal Auger GAP-note,* GAP-2005-088.

[109] P. Younk, "Measurements of SD-FD Time Offset Using Inclined Laser Shots," *Internal Auger GAP-note,* GAP-2006-005.

[110] Internet:, "http://www.physics.adelaide.edu.au/j̃bellido/auger/hybridreconstruction.html, 08/07/07,".

Acknowledgement

I am indebted to many people who supported me during the completion of this thesis. First of all I want to thank the University of Adelaide Astrophysics Group for the great experience of studying abroad, the introduction to astroparticle physics and the very pleasant working atmosphere which was the starting point for this thesis. Very special thanks to Prof. Bruce Dawson for supervising me during that time, his initial ideas, his friendly nature, for remaining an important contact person and for his agreement to be one of the revisers of this thesis. I would also like to gratefully acknowledge the support of Dr. Jose Bellido throughout this work and assistance in small and big problems. Thanks to Vanessa Holmes and Jerrad Denman for giving me an insight of the Australian way of life and the off-campus activities. Finally I appreciate the financial support of the DAAD (German Academic Exchange Service) without which this work experience abroad would not have been possible.

I am deeply indebted to Prof. Karl-Heinz Kampert who gave me the opportunity to work on this interesting subject and for his continuous support and supervision in all issues even in very busy times. I appreciate the very welcoming and friendly atmosphere of the Astroparticle Group in Wuppertal when continuing my research in Germany. I want to express my gratitude to all members of this group for fruitful discussions and backing throughout of this work. Here I want to set Dr. Markus Risse especially apart. He never got tired in answering my questions and gave important initial ideas for this work. Thanks also for proofreading and comments. I am indebted to Gabriele Zeitler who never got tired in signing forms and encouraging me in my projects and Dr. Tobias Flick for helpful annotations. Special thanks to Anna Franckowiak for proofreading, being a reliable mate during my studies and a faithful friend beyond the university.

In the end I want to express my gratitude to my friends and family who always supported me during my studies with patience and encouragement.